LUND UNIVERSITY

Constitutive Modelling and Finite Element Analysis of Concrete Structures with Regard to Environmental Influence

Dahlblom, Ola

1987

Total number of authors:
1

OLA DAHLBLOM

**CONSTITUTIVE MODELLING AND FINITE ELEMENT
ANALYSIS OF CONCRETE STRUCTURES WITH
REGARD TO ENVIRONMENTAL INFLUENCE**

LUND INSTITUTE OF TECHNOLOGY
Division of Structural Mechanics
Report TVSM-1004

OLA DAHLBLOM

CONSTITUTIVE MODELLING AND FINITE ELEMENT ANALYSIS OF CONCRETE STRUCTURES WITH REGARD TO ENVIRONMENTAL INFLUENCE

ACKNOWLEDGEMENTS

Lund, June 1987

Ola Dahlblom

ABSTRACT

A constitutive model for concrete is formulated. Tensile fracture is described using a smeared crack approach where the fracture energy is considered and the shear stiffness in the cracked region is gradually reduced as cracking develops. Environmentally induced strain due to variation of moisture and temperature is taken into account and may be made dependent on the stress state. Creep is modelled by a rate type formulation.

In order to clarify whether the fracture description is accurate in reflecting the input value of fracture energy per unit area a concrete tension specimen is simulated, and good results are achieved.

The behaviour of a non-loaded drying concrete specimen is simulated by a theoretical analysis, in order to find to what extent the overall specimen behaviour is influenced by the non-uniform stress state caused by drying. According to the analysis the deformation after a long time differs only slightly from the material contraction due to drying.

According to several experimental observations the deformation of a loaded drying specimen is significantly larger than the sum of the deformation of a non-loaded drying specimen and the deformation of a loaded non-drying specimen. The excess deformation is often referred to as stress induced shrinkage or as drying induced creep. A theoretical simulation of a specimen results in the conclusion that the effect is largely a result of stress dependence of the moisture induced strain.

CONTENTS   PAGE

1. INTRODUCTION

1.1 General remarks

In many situations concrete structures are exposed to environmental influence. A variety of physical and chemical processes influence concrete and may cause destruction of the material. This may lead to severe structural damage which is difficult and expensive to repair. In Fig. 1.1 some examples of structures exposed to environmental influence are shown.

Bridge · Silo

Deep water platform · Hydroelectric power plant
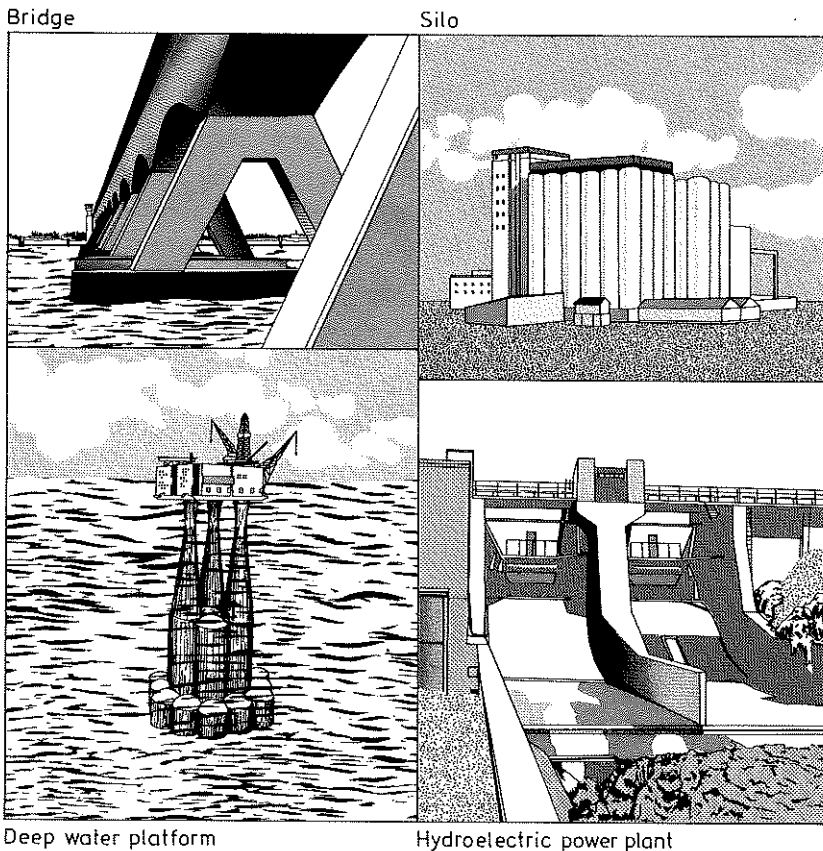
Fig. 1.1. Structures exposed to environmental influence.

In most applications concrete is exposed to changing moisture
content and temperature, causing contraction or expansion of the
material. Since drying of concrete is a very slow process the
moisture distribution in a drying structure will normally be
non-uniform. This non-uniform moisture distribution causes a
non-uniform distribution of drying induced strains. Since these
strains cannot, in general, develop without constraint a
non-uniform internal stress distribution is produced, which
typically results in cracking. Due to chemical reactions in
concrete at early ages, heat is generated. This leads to a
non-uniform temperature distribution which may result in
cracking. When a moist structure is exposed to temperatures below
the freezing point of water the expansion of the water at
freezing leads to tensile stresses which may exceed the strength
of the material and cause cracking. Some chemical substances like
acids and salts affect concrete by dissolving the material or by
reacting with substances in the concrete. The latter may cause
expansion also leading to crack development. Another type of
chemical influence on concrete is so called carbonization, i.e.
the reaction between carbon dioxide of the air and substances in
the concrete. This causes contraction of the material and
reduction of the pH value, which may lead to corrosion of
reinforcement bars.

The damage to concrete structures in practice is often the result
of several of the environmental effects mentioned above. The
different effects interact in a complicated way. The result of,
for example, exposure to chemical substances may be dependent on
whether the concrete contains cracks or not. This means that it
may be impossible to obtain a relevant prediction of some types
of environmental influence without having a reasonable
description of crack development due to variations of moisture
and temperature conditions.

To achieve an understanding of the effects of environmental influence, experiments are often performed by exposing specimens to different loading and environmental conditions. However, the observed behaviour is the response of specimens in which, especially for environmental loading, stress distributions are non-uniform. Therefore the results cannot always be directly interpreted as material properties. When trying to interpret the test results in terms of material properties there has been a long standing discussion of whether the non-uniform stress state has a significant influence on the observed specimen behaviour or not, cf. Fig. 1.2.
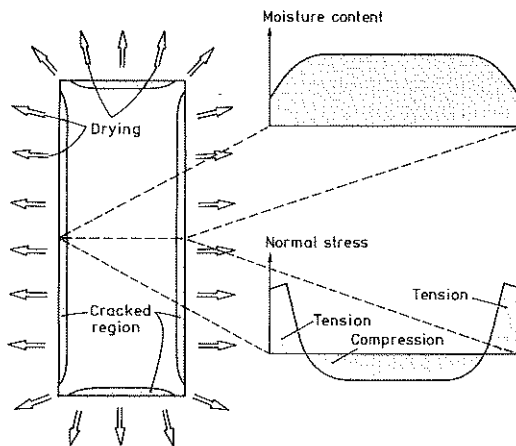
Fig. 1.2. Illustration of moisture and stress distribution in a drying specimen.

As an example of these interpretation problems it has been experimentally observed that the deformation of a loaded drying specimen is significantly larger than the sum of the deformation of a loaded specimen under constant environmental conditions and the deformation of a non-loaded drying specimen, cf. Fig. 1.3. This behaviour is called the Pickett effect or often sorption creep or drying creep. Various explanations have been suggested

for this effect. Some researchers have proposed that the Pickett effect to a major extent or even totally is due to non-uniform stress distribution and cracking in drying specimens. Others have suggested that the Pickett effect is a property of the material and not due to the influence of the non-uniform stress distribution.
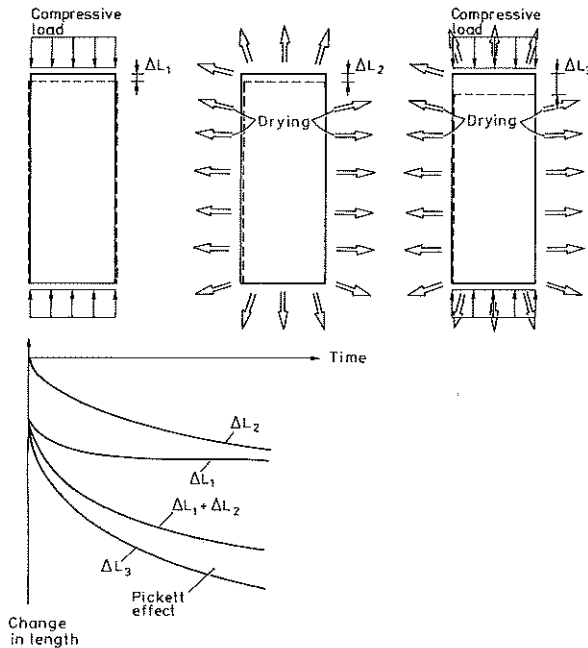
Fig. 1.3. Illustration of the Pickett effect.

1.2 Aim of the present investigation

To accurately predict the mechanical behaviour of concrete structures exposed to environmental influence, non-linear effects have to be considered. Therefore, to achieve realistic analyses, material modelling becomes a crucial point. The present work aims to provide a constitutive model which is suitable for describing the strains caused by changes of moisture and temperature and also gives a proper description of crack development.

Due to the complexity of non-linear problems, numerical methods have to be applied. The finite element method has proven to be an efficient tool in structural analysis and is therefore used in the present study. Thus, the constitutive model is implemented in a finite element program. By use of the program the behaviour of specimens subjected to different loadings is simulated. As a convincing description of the Pickett effect is of fundamental importance, when trying to estimate the response of concrete structures exposed to general environmental influence, emphasis is given to investigations of this effect. Interest is thus focused on drying experiments both on non-loaded and loaded specimens. One aim of the simulations is to find out to what extent the specimen length change is affected by the non-uniform stress state. This knowledge is the key to the question about to what extent the Pickett effect is caused by non-uniform stress distributions in drying specimens.

1.3   Summary of the contents

In Chapter 2, experimentally observed phenomena on concrete specimens subjected to mechanical loading and environmental influence are briefly described. A review of previous work regarding theoretical description of the behaviour is also given.

In Chapter 3, a material model for concrete is proposed. In this model, tensile fracture is described by a smeared crack approach where the energy dissipated during crack development is taken into consideration in an objective manner and where the shear stiffness is gradually reduced during crack development. Conventionally, moisture induced and thermal strains are assumed to depend only on the change of moisture content and temperature, respectively. In the present model, dependence on the stress may also be assumed. To model time dependent deformation under sustained load, a rate type creep formulation is used.

The finite element formulation, the numerical solution procedure and the computer program applied are described in Chapter 4.

In Chapter 5, the fracture of a concrete tension specimen, in constant environmental conditions, is simulated by use of the finite element method. The purpose of the simulation is to demonstrate the objectivity of the predicted fracture energy with respect to the finite element mesh.

Finite element simulations of concrete specimens subjected to different loading and moisture conditions are performed in Chapter 6. The results are qualitatively compared with experimentally observed behaviour and conclusions regarding the Pickett effect are put forward.

In Chapter 7, some concluding remarks and some suggestions for further research are given.

1.4   Notations

Equations are, in general, written in component form and, unless otherwise indicated, the summation convention is applied, see e.g. Malvern [35]. For computer programming, matrix notations are in general most convenient. Thus, the equations which are to be implemented as computer code are rewritten in matrix form.

A component of a vector or a tensor is indicated by using indices, e.g. f_i or σ_{ij}. To make a distinction between a tensor or a vector itself and its components, tensors and vectors are denoted by boldface letters, e.g. $\mathbf{f}$ or σ. The time derivative is denoted by a dot over the variable considered, e.g. $\dot{f}_i$.

Throughout this work small strains, displacements and rotations are assumed. Tensile stresses and elongations are considered as positive quantities. Dynamic effects are neglected.

The notations are explained in the text where they first appear. They are listed in Appendix A.

References to literature are quoted in the text by numbers in square brackets, [ ]. The references are given in alphabetical order in Appendix C.

2.   PHENOMENOLOGICAL DESCRIPTION AND PREVIOUS WORK

2.1   Introduction

The purpose of this chapter is to give a brief description of the
experimentally observed behaviour of concrete, important to the
present work, and to give a review of previous work regarding the
theoretical description of the observed behaviour. The
description is concentrated upon the non-linear behaviour due to
tensile stresses and the behaviour related to drying. The
influence of concrete composition is not included in the
description. In Sec. 2.2 some general features of the mechanical
behaviour of concrete are given. The specific material behaviour
under variable environmental conditions is described in Sec. 2.3.
A review of previous work concerning concrete behaviour under
variable environmental conditions and concrete fracture is given
in Sec. 2.4.

2.2   Behaviour under constant environmental conditions

For a concrete specimen loaded uniaxially in compression the
force-deformation curve has typically the form shown in Fig. 2.1.
Up to 30-50% of the ultimate load, the curve is approximately
linear. An increase in the compressive deformation when the
ultimate load has been reached leads to a decrease in compressive
force.

The tensile strength of concrete is typically 7-10% of the
compressive strength. When a specimen is loaded in tension a
localized crack develops. Because of the localized nature of the
fracture it is inappropriate to describe the behaviour using a
relation between stress and strain. Such a relation will be
dependent on the gauge length over which the deformation is
measured. Petersson [48] has performed displacement controlled
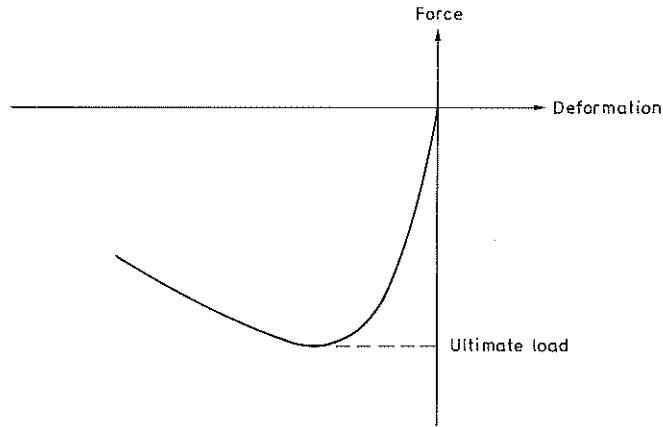
Fig. 2.1.   Force–deformation curve for concrete uniaxially loaded
in compression.

tensile tests on concrete using a necked specimen as shown in
Fig. 2.2. The force–deformation curve is approximately linear up
to 80–90% of the ultimate load. An increase in the displacement
after the ultimate load has been reached results in a decrease in
the force until the specimen has totally disintegrated. The area
under the force–displacement diagram is a measure of the energy
dissipated when the crack is produced. A typical response for a
tension specimen, as obtained by Petersson [48], is shown in Fig.
2.3.

The stiffness and the ultimate load are to some degree affected
by the moisture content.

The elastic modulus is somewhat higher in wet concrete than in
dry while the opposite holds for the compressive strength,see
e.g. Ref. [11].
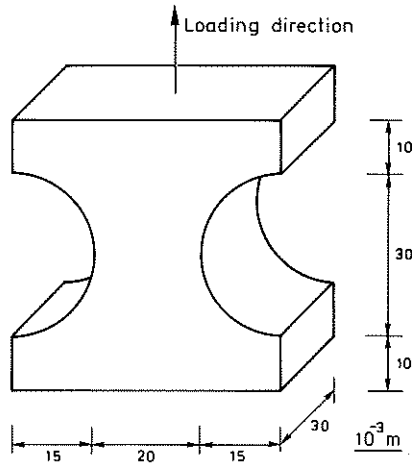
Fig. 2.2. Concrete tension specimen.

As regards the strength and stiffness of specimens which have been drying, it should be noted that the behaviour may be affected by the history of non-uniform stress in a specimen due to drying.

It has been experimentally shown that the modulus of elasticity and the compressive strength decrease as the temperature is raised. As an example Saemann and Washa [53] have found the compressive strength to be about 15 % less at $100^{o}C$ than at $20^{o}C$ and the elastic modulus to be about 10-20 % less at $100^{o}C$ than at $20^{o}C$.

As the concrete ages, the elastic modulus, the tensile strength and the compressive strength increase. The properties change at a decreasing rate as the concrete ages, see e.g. Byfors [12]. After 28 days the concrete is often assumed to be fully hardened.
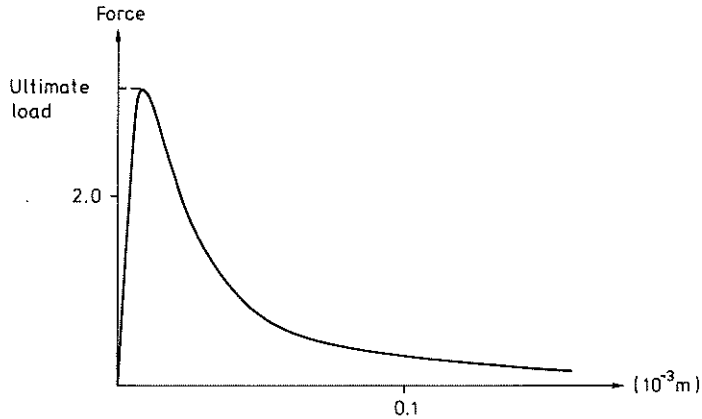
Fig. 2.3. Force–deformation   curve   for   concrete   loaded   in tension. Gauge length = $40 \cdot 10^{-3}$ m.

When a load is applied to a concrete specimen, instantaneous deformation occurs. If the load is retained creep occurs. As an example, the deformation history according to experiments performed by Gamble and Parrott [26], is shown in Fig. 2.4. The applied load was approximately equal to 20% of the ultimate load at the age of 7 days when the concrete was loaded. The specimen was unloaded 98 days after loading. The temperature and the relative humidity were held constant at $19^{\circ}C$ and 100% respectively.

It has been observed that the creep rate is directly proportional to the stress up to about 50% of the ultimate stress, see e.g. Mamillan [36]. Above this limit the creep rate increases at an increasing rate as the stress is raised. For stresses higher than about 80% of the ultimate stress, creep rupture may result, see Neville [38].
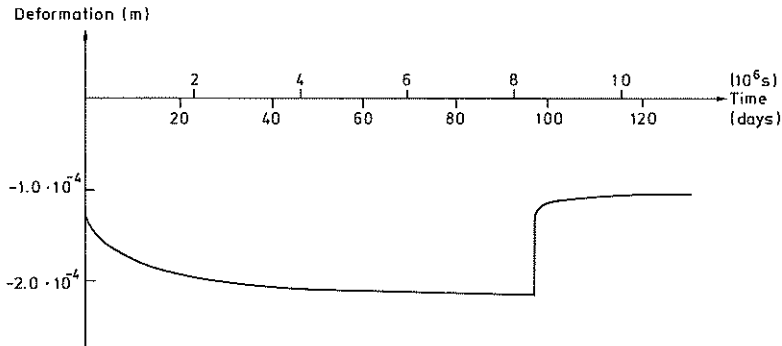
Fig. 2.4. Observed deformation of concrete specimen (0.5×0.1×0.1 m) with a compressive load, $\sigma = -7.9\cdot 10^6$ Pa, and constant environmental conditions.

The creep is influenced by the moisture content of the concrete. The creep of wet concrete is larger than the creep of dry concrete, see e.g. Bazant et al. [5].

At a high temperature the creep is larger than at room temperature, see e.g. England and Ross [24].

At early ages the creep is considerably larger than at late ages, see e.g. Byfors [12].

2.3   Behaviour under variable environmental conditions

The deformation observed in a non-loaded specimen subjected to variable moisture conditions is referred to as drying shrinkage or as swelling, depending on whether the moisture content decreases or increases. The shrinkage is approximately proportional to the change of moisture conteand depends on the age of the concrete. The shrinkage is influenced only slightly by

moist curing periods less than about a month before commencement
of drying. However, longer moist curing periods before
commencement of drying, lead to smaller values of shrinkage, see
e.g. Byfors [12]. When the specimen is re-wetted, most of the
shrinkage is recovered by swelling.

In a drying specimen, the moisture content close to the surface
decreases faster than in the core. This gives rise to a non-
uniform distribution of moisture. Since the shrinkage is
dependent on the moisture content the non-uniform moisture
distribution produces a non-uniform stress state, which may
result in crack development. The observed deformation of a drying
specimen is therefore the combined result of deformation caused
by moisture change and deformation caused by the non-uniform
stress state. A typical shrinkage curve observed in experiments
by Gamble and Parrott [26] is shown in Fig. 2.5. An initially
damp specimen of size 0.5x0.1x0.1 m was drying in an environment
with 65% relative humidity. The temperature was held constant at
19°C.

If a specimen under sustained compressive load is allowed to dry
the observed deformation is significantly larger than the sum of
the deformation of a loaded specimen in constant environmental
conditions and the deformation of a non-loaded drying specimen.
The excess deformation is often referred to as stress induced
shrinkage or as drying induced creep. The phenomenon was first
documented by Pickett [49] and is called the Pickett effect.

This effect is illustrated in Fig. 2.6, which shows experimental
results according to Gamble and Parrott [26]. Curve I in the
figure shows the deformation of a loaded drying specimen. The
relative humidity was initially 100%. The specimen was subjected
to 65% relative humidity and a compressive load corresponding to
a mean stress $\sigma = -7.9 \cdot 10^{6}$ Pa. The temperature was held constant
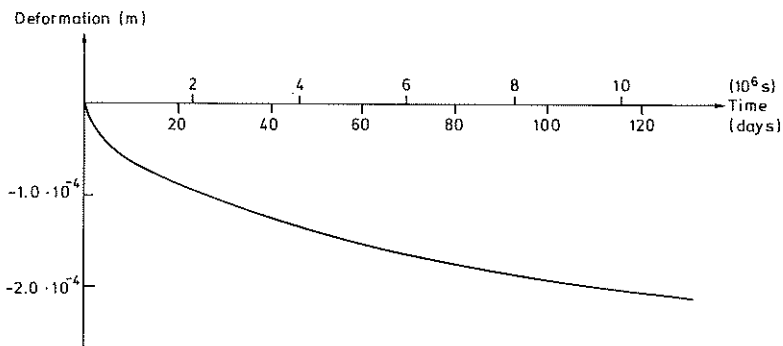
Deformation (m)

Fig. 2.5. Observed deformation of an initially damp concrete
specimen (0.5×0.1×0.1 m) subjected to 65% relative
humidity. No external load is applied.

at 19°C. The concrete was loaded at the age of 7 days and the
specimen was unloaded after 98 days. After this time the relative
humidity was also 65%.

As a comparison, curve II in the figure shows the sum of the
deformation of a loaded non-drying specimen according to Fig. 2.4
and the deformation of a non-loaded drying specimen according to
Fig. 2.5. The difference between curves I and II is the Pickett
effect, which appears to be quite significant.

It has been observed that the stress induced shrinkage is
proportional to the drying shrinkage and to the stress, see for
instance Gamble and Parrott [26] and Day et al. [22]. The Pickett
effect has also been observed for loading in tension and in
shear, see for instance Domone [23] and Ishai and Glucklich [33].

A variation of temperature causes thermal strain, which is
approximately proportional to the temperature change. If a loaded
specimen is subjected to an increase of temperature, the
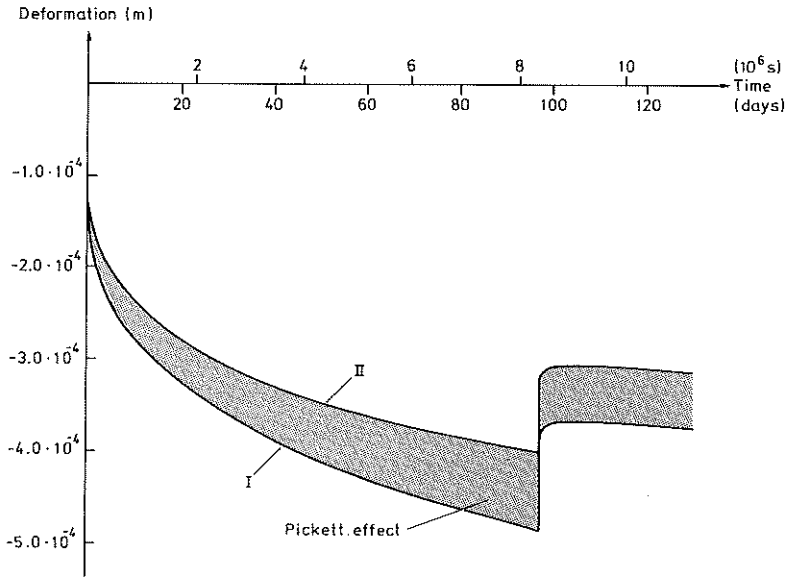
Fig. 2.6. Observed deformation of an initially damp concrete specimen subjected to 65% relative humidity and a compressive load (curve I). The sum of the deformation of a loaded non-drying specimen and the deformation of a non-loaded drying specimen (curve II). The difference between curves I and II is the Pickett effect.

deformation will be significantly larger than the sum of the deformation of a loaded specimen at constant temperature and the deformation of a non-loaded specimen subjected to an increasing temperature, see e.g. Hansen and Eriksson [28], Illston and Sanders [31] and Parrott [45]. The behaviour is similar to the Pickett effect observed in drying specimens. The excess deformation is often referred to as transitional creep. In analogy to the concept of stress induced shrinkage it may also be regarded as stress induced thermal strain.

2.4   Review of previous work

Ever since the Pickett effect was first documented, efforts have been made to describe it theoretically. Attempts have been made to handle the Pickett effect by assuming that creep is dependent on the rate of moisture change, in addition to the commonly assumed stress dependence. In early works a clear distinction between material properties and the behaviour of specimens is not often made. During drying, a non-uniform stress state with tensile stresses close to the surface is developed. If a compressive load is applied during drying the tensile stresses are compensated for, and crack development is prevented. Wittmann and Roelfstra [59] suggest that the Pickett effect is, to a major extent or even completely, due to prevention of crack formation and modification of the stress state caused by an applied compressive load. Bazant and Raftshol [9] analysed the significance of cracking caused by the non-uniform stress state due to drying. Their conclusion is that the specimens must be very thin (about 1 mm) and the environmental humidity must be lowered sufficiently slowly in order to avoid development of cracks. It has been suggested by Thelandersson [58] that the drying induced strain rate depends on the current stress state in addition to the commonly assumed dependence on moisture content changes. This approach has also been used by Bazant and Chern [7]. One conclusion of their work is that the Pickett effect can be seen partly as a true material property and partly as an apparent mechanism.

On the basis of experimental investigations Day et al. [22], conclude that the effect is a property of the material and not due to spurious influence caused by internal moisture gradients. However, it has not been clearly shown until now to what extent the different causes contribute to the observed behaviour. Such a clarification is a major purpose of the present work. Assuming

material properties, the behaviour of specimens is simulated by finite element analyses, which give information as to what amount the overall behaviour is influenced by the stress states in drying specimens.

It appears from the above discussion that the description of crack development is a crucial point in the analysis of drying concrete. Modelling of cracks can be accomplished by two different approaches, a discrete approach and a smeared approach. In the discrete approach cracks are assumed to follow element boundaries. When this approach is used, the finite element mesh is chosen in such a way that expected crack planes coincide with element boundaries. In situations where the crack pattern is not known a priori, such an approach is obviously not very attractive. Alternatively the finite element mesh can be redefined during the analysis, either by hand or automatically, see Ingreffea and Saouma [32]. In either case, however, such procedures significantly complicate the approach. In the smeared approach, the discontinuities introduced by cracking are ignored and attention is paid only to the changing ability to transfer stresses. This is achieved by changing the material properties in the elements where cracks develop. This leads to a very convenient numerical scheme. However, as demonstrated by Bazant and Cedolin [6], the original smeared concept proposed by Rashid [50], is not objective with respect to the finite element mesh. When the elements tend to be infinitely small, the energy dissipated by the cracks approaches zero. Modelling of cracks is significantly improved by the fictitious crack model according to Hillerborg et al. [30], in which the energy dissipated by crack development is used as a material parameter. The fictitious crack model was originally applied as a discrete approach, but to facilitate its use in numerical analyses Nilsson and Oldenburg

[40] have proposed a smeared version of the model. However, the results obtained by Oldenburg [41] with this approach are, not completely satisfactory since the results do not correctly reflect the assumed value of the fracture energy per unit area.

Another smeared approach is the crack band model by Bazant and Oh [8], in which the width of the process zone is claimed to be a material property. In the present work a smeared version of the fictitious crack model is proposed. To obtain this a so called equivalent length is introduced. This equivalent length, in contrast to the width of the process zone of the crack band model, is a purely geometrical quantity determined by the element size and form. Moreover the present approach includes a method of considering the reduction of the shear stiffness due to fracture development which is objective with respect to element size. The approach gives considerably improved results compared. with previous smeared approaches.

3. CONSTITUTIVE EQUATIONS

3.1 Introduction

Theoretical analyses of the phenomena described in Secs. 2.2 and
2.3 require a proper material description. The material model
which will be described below aims to be general enough to
reflect qualitatively the phenomena of interest without being
more complicated than necessary. This means that as few
parameters as possible are used to describe the material.

The material model now proposed considers tensile softening by a
smeared crack approach based on the fictitious crack model
accordning to Hillerborg et al. [30], where the fracture energy
of localized cracks is taken into account. The present approach
differs from previous concepts, e.g. Nilsson and Oldenburg [40]
and Bazant and Oh, [8] in the manner of relating the crack width
to element strain, the expression for reduction of shear
stiffness and the manner of dealing with closing cracks.

Environmentally induced strains due to changes of moisture
content and temperature, are often assumed to depend only on the
changes of moisture content and temperature respectively. In the
present material model dependence on the stress state, as
suggested by Thelandersson [58], may also be optionally chosen.

Time dependent deformation under sustained stress, i.e. creep, is
modelled by a rate type formulation where the total stress
history need not be available.

Since the ultimate stress is much lower in tension than in
compression, a common situation in real concrete structures under
service loadings is that the ultimate tensile stress is exceeded,
while the maximum compressive stress is well below the
proportional limit. This situation is assumed to be valid in the

present study. For convenience the behaviour in compression is therefore modelled simply by linear elasticity, i.e. compression failure is not included in the model. This assumption is well within the scope of the present study. However, a variety of theories exist for description of the nonlinear behaviour of concrete in compression, see e.g. Chen and Saleeb [15], Chen [14], Nilsson [39] and Ref. [25].

The strain rate tensor $\dot{\epsilon}$ is assumed to consist of the sum of the elastic, fracturing, moisture induced, thermal and creep strain rate tensors, respectively denoted by $\dot{\epsilon}^e$, $\dot{\epsilon}^f$, $\dot{\epsilon}^w$, $\dot{\epsilon}^T$ and $\dot{\epsilon}^c$, i.e.

$$\dot{\epsilon}_{ij} = \dot{\epsilon}^e_{ij} + \dot{\epsilon}^f_{ij} + \dot{\epsilon}^w_{ij} + \dot{\epsilon}^T_{ij} + \dot{\epsilon}^c_{ij} \tag{3.1}$$

In the following sections expressions for the tensors appearing on the right-hand side of Eq. (3.1) are derived. In the present work the tensors $\dot{\epsilon}^e$, $\dot{\epsilon}^w$, $\dot{\epsilon}^T$ and $\dot{\epsilon}^c$ are assumed to be related to the stress or rate of stress by isotropic fourth-order tensors, which for the sake of clarity are expressed in two material parameters in the same way. The chapter is concluded by the establishment of a relation between total strain rate and stress rate.

3.2   Elastic strain

Assuming isotropy, the elastic strain tensor ϵ^e is related to the stress tensor σ by the generalized Hooke's law

$$\epsilon^e_{ij} = C^e_{ijkm}\sigma_{km} \tag{3.2}$$

where C^e is the isotropic compliance tensor, given by

$$C^e_{ijkm} = \rho_e \delta_{ij}\delta_{km} + \kappa_e(\delta_{ik}\delta_{jm} + \delta_{im}\delta_{jk}) \tag{3.3}$$

Here δ_{ij} is Kronecker's delta and ρ_e and κ_e are elastic parameters related to the elastic modulus E and Poisson's ratio v by

$$\rho_e = -\frac{v}{E} \tag{3.4}$$

$$\kappa_e = \frac{1+v}{2E} \tag{3.5}$$

The elastic parameters E and v may depend on aging, i.e. time t, moisture content w and temperature T, i.e.

$$E = E(t, w(t), T(t)) \tag{3.6}$$

$$v = v(t, w(t), T(t)) \tag{3.7}$$

The elastic strain rate is given by the time derivative of Eq. (3.2), i.e.

$$\dot{e}^e_{ij} = C^e_{ijkm}\dot{\sigma}_{km} + \dot{e}^t_{ij} \tag{3.8}$$

where

$$\dot{e}^t_{ij} = \dot{C}^e_{ijkm}\sigma_{km} \tag{3.9}$$

and where, according to Eq. (3.3)

$$\dot{C}^e_{ijkm} = \dot{\rho}_e\delta_{ij}\delta_{km} + \dot{\kappa}_e(\delta_{ik}\delta_{jm} + \delta_{im}\delta_{jk}) \tag{3.10}$$

The parameters $\dot{\rho}_e$ and $\dot{\kappa}_e$ can, according to Eqs. (3.4) and (3.5) be written

$$\dot{\rho}_e = \frac{\upsilon}{E^2} \dot{E} - \frac{1}{E} \dot{\upsilon} \qquad (3.11)$$

$$\dot{\kappa}_e = -\frac{1+\upsilon}{2E^2} \dot{E} + \frac{1}{2E} \dot{\upsilon} \qquad (3.12)$$

3.3   Fracturing strain

Crack development is assumed to start when the maximum principal
stress reaches the unaxial tensile strength. The crack plane of
the first crack is assumed to be normal to the direction of the
maximum principal stress. A possible second crack is assumed to
develop perpendicular to the first crack, if the normal stress in
that direction also reaches the tensile strength. Likewise a
third crack may develop perpendicular to the existing two cracks.

For convenience, a local coordinate system is introduced, where
the $\bar{x}_1$-axis is normal to the plane of the first crack. If a
second crack has occurred the $\bar{x}_2$-axis is normal to the plane of
that crack. The unit vectors $\bar{i}_i$ in the local coordinate system
are related to the unit vectors i_k in the global coordinate
system by the relation

$$\bar{i}_i = a_{ik} i_k \qquad (3.13)$$

where

$$a_{ik} = \cos(\bar{x}_i, x_k) \qquad (3.14)$$

in which $\bar{x}_i$ and x_k denote local and global coordinates
respectively. It may be noted that, in the present description of
fracture, barred variables relate to the local coordinate system.

The fictitious crack model according to Hillerborg et al. [29], [30], [37] is based on the fact that when a specimen is loaded in tension, fracture is localized to a thin zone. The deformation caused by fracture in this zone is modelled by a fictitious crack whose width $\overline{w}_\alpha$ represents the total fracturing deformation in the zone. The material outside the fracture zone is assumed to be unaffected by cracking. The stress $\overline{\sigma}_{\alpha\alpha}$ normal to the plane of crack No α is assumed to decrease when the crack width $\overline{w}_\alpha$ increases. It should be noted that when α or β is used as tensor index in this description a specific component is assumed and that the summation convention is not applied for a repeated index α or β.

The energy G_F necessary to produce one unit area of crack is given by the integral

$$G_F = \int_0^{w_c} \overline{\sigma}_{\alpha\alpha} d\overline{w}_\alpha \tag{3.15}$$

where w_c is the crack width when the normal stress has dropped to zero. The stress $\overline{\sigma}_{\alpha\alpha}$ can be made to depend on $\overline{w}_\alpha$ in a variety of ways. In the present work $\overline{\sigma}_{\alpha\alpha}$ is for the sake of simplicity assumed to be a linear function of $\overline{w}_\alpha$, i.e.

$$\overline{\sigma}_{\alpha\alpha} = f_t + N\overline{w}_\alpha \tag{3.16}$$

where f_t is the unaxial tensile strength which is assumed to be constant, and N is a proportionality constant ($N < 0$). The relation of $\overline{\sigma}_{\alpha\alpha}$ and $\overline{w}_\alpha$ is illustrated in Fig. 3.1.
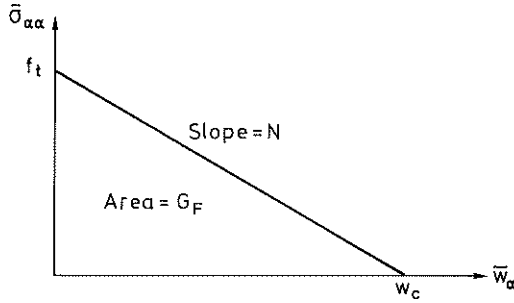
Fig. 3.1. Relation of stress $\bar{\sigma}_{\alpha\alpha}$ and crack width $\bar{w}_{\alpha}$.

The concept of using a constitutive relation between stress and crack width rather than strain was originally based on experimental observations, but it can also be based on purely thermodynamical arguments, see Ottosen [43].

Eq. (3.16) and the fact that the normal stress is zero when the crack width is w_c yield

$$w_c = -\frac{f_t}{N} \tag{3.17}$$

Substitution of Eq. (3.16) into Eq. (3.15), evaluation of the integral and use of Eq. (3.17) results in

$$N = -\frac{f_t^2}{2G_F} \tag{3.18}$$

A fracturing strain tensor ϵ^f is introduced which represents the mean fracturing strain in some region which includes the discrete crack. The fracturing strain $\bar{\epsilon}^f_{\alpha\alpha}$ normal to the plane of crack No α is defined by

$$\bar{\epsilon}^f_{\alpha\alpha} = \frac{\bar{w}_\alpha}{L_\alpha} \tag{3.19}$$

where L_α is an equivalent length associated with crack No α which will be further discussed in Chapter 4.

Substitution of Eq. (3.19) into Eq. (3.16) and differentiation with respect to time yields

$$\dot{\bar{\epsilon}}^f_{\alpha\alpha} = J_\alpha \dot{\bar{\sigma}}_{\alpha\alpha} \tag{3.20}$$

where

$$J_\alpha = \frac{1}{NL_\alpha} \tag{3.21}$$

Eq. (3.21) is valid on condition that

$$\dot{\bar{w}}_\alpha > 0, \quad \bar{w}_\alpha = \bar{w}_{\alpha,\max} \tag{3.22}$$

where $\bar{w}_{\alpha,\max}$ is the maximum previously obtained value of $\bar{w}_\alpha$. If this condition is not satisfied, i.e. if crack closing takes place, a fraction of the developed crack width is assumed to be recoverable, depending on the material parameter γ_f which has a value in the range $0 \leq \gamma_f \leq 1$, where the lower bound represents total recoverability and the upper bound represents total irrecoverability. For tensile stresses, i.e. $\bar{\sigma}_{\alpha\alpha} \geq 0$, a linear relation between crack width and stress is also assumed during unloading, i.e.

$$\bar{w}_\alpha = \left[\gamma_f + (1-\gamma_f)\frac{\bar{\sigma}_{\alpha\alpha}}{f_\alpha}\right]\bar{w}_{\alpha,\max} \tag{3.23}$$

where

$$f_\alpha = f_t + N\bar{w}_{\alpha,max} \qquad (3.24)$$

It may be noted that for $\bar{\sigma}_{\alpha\alpha} = f_\alpha$ Eq. (3.23) yields $\bar{w}_\alpha = \bar{w}_{\alpha,max}$ and for $\bar{\sigma}_{\alpha\alpha} = 0$ we have $\bar{w}_\alpha = \gamma_f \bar{w}_{\alpha,max}$. The parameter γ_f is illustrated in Fig. 3.2.
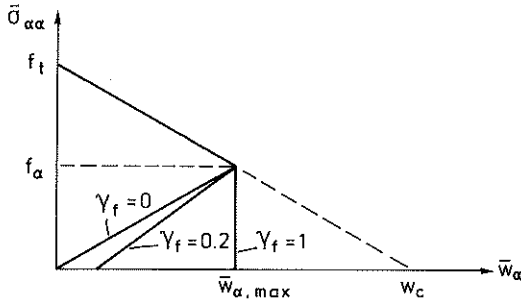
Fig. 3.2. Illustration of parameter γ_f.

Substitution of Eq. (3.23) into Eq. (3.19) and differentiation with respect to time yields, once again, Eq. (3.20), but now the coefficient J_α is given by

$$J_\alpha = (1-\gamma_f) \frac{\bar{w}_{\alpha,max}}{L_\alpha f_\alpha} \qquad (3.25)$$

For compressive stresses, $\bar{\sigma}_{\alpha\alpha} < 0$, the crack width is assumed to be constant and thus the fracturing strain rate is assumed to be zero, i.e. Eq. (3.20) is still valid but now with J_α given by

$$J_\alpha = 0 \qquad (3.26)$$

In previous work it has often been assumed that the developed

fracture is totally irrecoverable, see e.g. Oldenburg [41] or Leibengood et al. [34], corresponding to $\gamma_f = 1$, or totally recoverable, see e.g. Rots et al. [52] or Glemberg [27], corresponding to $\gamma_f = 0$. Experimental results obtained by Reinhardt [51] indicate that neither of these assumptions is realistic. The approach now proposed with partly recoverable fracture agrees fairly well with the experimental behaviour, as illustrated in Fig. 3.3.
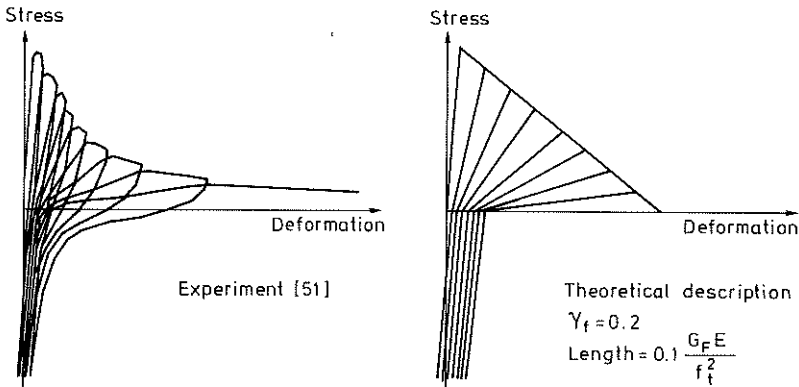
Fig. 3.3. Comparison of experiment and theoretical description.

Development of a crack will reduce the ability to transfer shear stresses across the crack plane. In analysis of fracture it is important, in addition to modelling the behaviour normal to a crack plane, to obtain a reasonable expression for the shear behaviour. A common way of handling the reduction of shear stiffness is simply to multiply the elastic shear modulus by a so called shear retention factor which has a constant value in the from 0 to 1, see e.g. Leibengood et al. [34] or Rots et al. [52]. It is, however, not satisfactory to assume that the reduction of the shear stiffness is independent of the crack width. It is reasonable to assume that the shear stiffness is reduced gradually as the crack width increases. Since the fracture is

localized to a thin zone the reduction of shear stiffness is related to this zone and the shear stiffness in the region outside the zone is unaffected by cracking. When a smeared crack approach is used an effective shear modulus, representative of some region which includes the crack, is applied. The effective shear modulus depends on the shear stiffness of the fracture zone and also on the shear stiffness of the unaffected region outside the zone, and is therefore dependent on the size of the region considered. It is thus not acceptable to use a shear retention factor which is not related to the size of the region of which it is assumed to be representative. In experiments by Paulay and Loeber [46] relationships between shear stress and shear displacement at constant crack widths have been obtained. According to their results the shear displacement is more or less proportional to the shear stress and to the crack width. Based on this observations the shear displacement $\bar{w}^s_{\alpha\beta}$ in crack No α in the direction $\bar{x}_\beta$ is, as proposed by Ottosen and Dahlblom [44], assumed to be given by

$$\bar{w}^s_{\alpha\beta} = \frac{\bar{w}_\alpha}{G_s} \bar{\sigma}_{\alpha\beta} \qquad (\alpha \neq \beta) \qquad (3.27)$$

where $\bar{w}_\alpha$ is the crack width, G_s is a material parameter which in this investigation is referred to as the slip modulus, and $\bar{\sigma}_{\alpha\beta}$ is the shear stress in the crack plane.

In Fig. 3.4, Eq. (3.27) with $G_s = 3.8 \cdot 10^6$ Pa is compared with the experimental results according to Paulay and Loeber [46], and agreement seem to be reasonable. If Eq. (3.27) where replaced by a more complicated relation better agreement could of course be achieved, but since we are primarily interested in a simple model which qualitatively reflects the material behaviour Eq. (3.27) is accepted. The limited number of experimental results is another

reason for using a simple expression. Since Eq. (3.27) has the property that the shear displacement is zero for zero crack width it is reasonable to apply it for all crack widths, although the experimental results at present available only relate to fully open cracks.
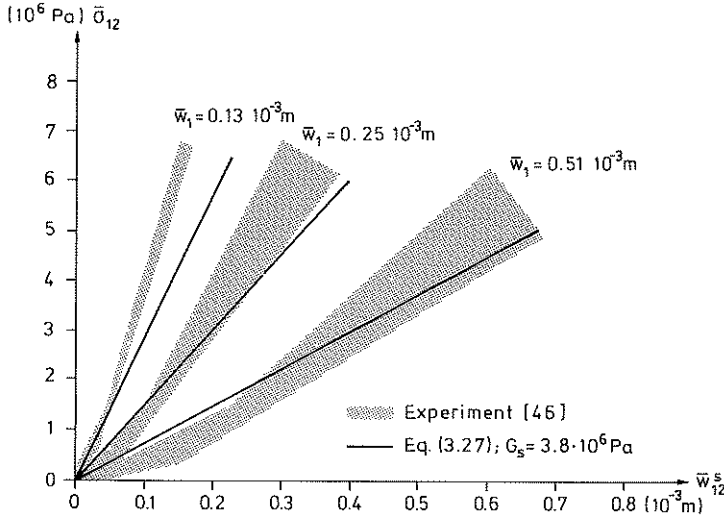
Fig. 3.4. Comparison of Eq. (3.27) and experimental results.

As in the case of fracture normal to the crack plane a fracturing strain component is defined for shear displacement. The fracturing shear strain $\bar{\epsilon}^f_{\alpha\beta}$ is defined by

$$\bar{\epsilon}^f_{\alpha\beta} = \frac{1}{2}(\frac{\bar{w}^s_{\alpha\beta}}{L_\alpha} + \frac{\bar{w}^s_{\beta\alpha}}{L_\beta}) \qquad (\alpha \neq \beta) \qquad (3.28)$$

where L_α is the equivalent length corresponding to crack No α as introduced above in Eq. (3.19). Substituting Eqs. (3.19) and (3.27) into Eq. (3.28) and considering that $\bar{\sigma}_{\alpha\beta} = \bar{\sigma}_{\beta\alpha}$, we have

$$\bar{\epsilon}^f_{\alpha\beta} = \frac{1}{2}(\bar{\epsilon}^f_{\alpha\alpha} + \bar{\epsilon}^f_{\beta\beta}) \frac{\bar{\sigma}_{\alpha\beta}}{G_s} \qquad (\alpha \neq \beta) \qquad (3.29)$$

Assuming all material parameters to be constant, differentiation of Eq. (3.28) with respect to time and substitution of Eq. (3.20) yields

$$\dot{\bar{\epsilon}}^f_{\alpha\beta} = A_{\alpha\beta}\dot{\bar{\sigma}}_{\alpha\beta} + B_{\alpha\beta}\dot{\bar{\sigma}}_{\alpha\alpha} + B_{\beta\alpha}\dot{\bar{\sigma}}_{\beta\beta} \qquad (\alpha \neq \beta) \qquad (3.30)$$

where

$$A_{\alpha\beta} = \frac{\bar{\epsilon}^f_{\alpha\alpha} + \bar{\epsilon}^f_{\beta\beta}}{2G_s} \qquad (\alpha \neq \beta) \qquad (3.31)$$

$$B_{\alpha\beta} = \frac{J_\alpha \bar{\sigma}_{\alpha\beta}}{2G_s} \qquad (\alpha \neq \beta) \qquad (3.32)$$

Using Eqs. (3.20) and (3.30) a complete relation between fracturing strain rate and stress rate can be obtained

$$\dot{\bar{\epsilon}}^f_{pq} = \bar{C}^f_{pqrs}\dot{\bar{\sigma}}_{rs} \qquad (3.33)$$

where

$$\bar{C}^f_{1111} = J_1 \qquad (3.34a)$$

$$\bar{C}^f_{2222} = J_2 \qquad (3.34b)$$

$$\bar{C}^f_{3333} = J_3 \qquad (3.34c)$$

$$\bar{C}^f_{1212} = \bar{C}^f_{1221} = \bar{C}^f_{2112} = \bar{C}^f_{2121} = \frac{A_{12}}{2} \qquad (3.34d)$$

$$\bar{C}^f_{2323} = \bar{C}^f_{2332} = \bar{C}^f_{3223} = \bar{C}^f_{3232} = \frac{A_{23}}{2} \qquad (3.34e)$$

$$\bar{C}^f_{3131} = \bar{C}^f_{3113} = \bar{C}^f_{1331} = \bar{C}^f_{1313} = \frac{A_{31}}{2} \qquad (3.34f)$$

$$\bar{C}^f_{1211} = \bar{C}^f_{2111} = B_{12} \qquad (3.34g)$$

$$\bar{C}^f_{1222} = \bar{C}^f_{2122} = B_{21} \qquad (3.34h)$$

$$\bar{C}^f_{2322} = \bar{C}^f_{3222} = B_{23} \qquad (3.34i)$$

$$\bar{C}^f_{2333} = \bar{C}^f_{3233} = B_{32} \qquad (3.34j)$$

$$\bar{C}^f_{3133} = \bar{C}^f_{1333} = B_{31} \qquad (3.34k)$$

$$\bar{C}^f_{3111} = \bar{C}^f_{1311} = B_{13} \qquad (3.34l)$$

All other components $\bar{C}^f_{pqrs}$ are zero.

The stress and fracturing strain rate tensors expressed in the local coordinate system can be transformed to the global coordinate system by the usual relations

$$\dot{\bar{\sigma}}_{rs} = a_{rk} a_{sm} \dot{\sigma}_{km} \qquad (3.35)$$

$$\dot{\epsilon}^f_{ij} = a_{pi} a_{qj} \dot{\bar{\epsilon}}^f_{pq} \qquad (3.36)$$

where a_{ik} is given by Eq. (3.14). Eqs. (3.33), (3.35) and (3.36) can be combined to form a relation between fracturing strain rate and stress rate in the global coordinate system

$$\dot{\epsilon}^f_{ij} = a_{pi}a_{qj}\bar{\dot{C}}^f_{pqrs}a_{rk}a_{sm}\dot{\sigma}_{km} \tag{3.37}$$

3.4 Environmentally induced strain

The moisture induced and thermal strain rates are often assumed to be dependent only on the rate of change of moisture content and temperature, respectively. They can also, as suggested by Thelandersson [58] and later by Bazant and Chern [7] and by Thelandersson [57], be assumed to be dependent on the current stress state. The concept of stress dependence suggested by Thelandersson [57] is adopted here.

The thermal strain rate tensor $\dot{\epsilon}$ is therefore given by the sum of the conventional thermal strain rate tensor and a term which is proportional to the stress tensor σ, i.e.

$$\dot{\epsilon}^T_{ij} = \alpha_T\dot{T}(\delta_{ij} + \beta_T C^T_{ijkm}\sigma_{km}) \tag{3.38}$$

where α_T is the coefficient of thermal expansion, $\dot{T}$ is the rate of temperature change, C^T is the thermal strain compliance tensor and β_T is a parameter which can assume either the value 1 or 0 depending on whether or not stress dependence of thermal strain is assumed. If $\beta_T = 0$ we have the expression for conventional thermal strain theory. The thermal strain compliance tensor C^T which is a fourth-order tensor is for the sake of simplicity assumed to be an isotropic tensor and is thus dependent on only two material parameters. For the sake of clarity the tensor C^T is expressed in a way similar to the elastic compliance tensor C^e in Eq. (3.3), i.e.

$$C^T_{ijkm} = \rho_T\delta_{ij}\delta_{km} + \kappa_T(\delta_{ik}\delta_{jm} + \delta_{im}\delta_{jk}) \tag{3.39}$$

where ρ_T and κ_T are material parameters. The moisture induced strain rate tensor $\dot{\epsilon}^W$, analogously with Eq. (3.38), is given by

$$\dot{\epsilon}^W_{ij} = \alpha_w \dot{w}(\delta_{ij} + \beta_w C^W_{ijkm}\sigma_{km}) \qquad (3.40)$$

where

$$C^W_{ijkm} = \rho_w \delta_{ij}\delta_{km} + \kappa_w(\delta_{ik}\delta_{jm} + \delta_{im}\delta_{jk}) \qquad (3.41)$$

and α_w is the coefficient of drying shrinkage and $\dot{w}$ the rate of change of moisture content. The parameter β_w determines whether or not stress dependence is assumed. Just as for the parameter β_T of Eq. (3.38) the value of β_w can be either 1 or 0. If $\beta_w = 0$ we have the expression for the conventional moisture strain theory. The stress dependence of the moisture induced strain is described by the material parameters ρ_w and κ_w.

Experimental results according to Illston and Sanders [31] and Parrott [45] indicate that the stress dependence of thermal strain is pronounced on first heating, but for cooling or heating to a level previously attained the effect is not present or present to a small extent. In the absence of more detailed experimental information, the parameter β_T may be made $\beta_T = 1$ for $\dot{T} > 0$ and $T = T_{max}$, and $\beta_T = 0$ otherwise. Here T_{max} is the maximum previously attained temperature.

For moisture induced strain, experimental results according to Gamble and Parrott [26] and Day et al. [22] indicate, in the same way as in the above observations that the stress dependence is pronounced for the first drying. For the first wetting the effect is significantly smaller and for later moisture cycles the effect is smaller still. Due to the lack of more detailed experimental

results the parameter β_w may be made $\beta_w = 1$ for $\dot{w} < 0$ and $w = w_{min}$ and $\beta_w = 0$ otherwise. Here w_{min} is the minimum previously attained moisture content.

In analogy with Eqs. (3.4) and (3.5) the parameters ρ_T, κ_T, ρ_w and κ_w can be expressed as

$$\rho_T = -\upsilon_T F_T \tag{3.42}$$

$$\kappa_T = \frac{1+\upsilon_T}{2} F_T \tag{3.43}$$

$$\rho_w = -\upsilon_w F_w \tag{3.44}$$

$$\kappa_w = \frac{1+\upsilon_w}{2} F_w \tag{3.45}$$

where the parameters F_T and F_w describe the stress dependence of the environmentally induced strain for uniaxial stress and υ_T and υ_w are quantities analogous to Poisson's ratio υ. In the absence of detailed experimental results one may assume that $\upsilon_T = \upsilon$ and $\upsilon_w = \upsilon$.

3.5   Creep strain

The time dependent strain, i.e. creep, is approximately proportional to the stress. The uniaxial creep strain $\epsilon_c(t)$ for a constant uniaxial stress σ can then be written

$$\epsilon_c(t) = C(t,t')\sigma \tag{3.46}$$

where $C(t,t')$ is the creep compliance, representing the creep strain at time t due to a unit stress applied at time t'. Adopting the principle of superposition, which means that the creep strain due to a stress history $\sigma(t)$ is equal to the sum of

the creep strains due to stress increments applied at different times t', see e.g. Bazant [3], Eq. (3.46) may be written

$$\epsilon_c(t) = \int_0^t C(t,t') \frac{d\sigma}{dt'} dt' \tag{3.47}$$

The creep compliance $C(t,t')$ may be described by a Dirichlet series

$$C(t,t') = \sum_{n=1}^{N} F_n(t')(1 - e^{-\frac{t-t'}{\tau_n}}) \tag{3.48}$$

where the parameters τ_n are so called retardation times and the quantities $F_n(t')$ are creep compliance parameters. The contribution of each term is small for time values $t < 0.1 \tau_n + t'$ and almost equal to $F_n(t')$ for time values $t > 10 \tau_n + t'$, i.e. the values of τ_n determine in which time range the different terms exert an influence on the change of the sum. By making $\tau_n = 10 \tau_{n-1}$ the series may with good accuracy be used to represent an experimental creep curve.

Assuming isotropy, the following generalization of Eqs. (3.47) and (3.48), see e.g. Bazant [3], can be used.

$$\epsilon_{ij}^c = \sum_{n=1}^{N} \int_0^t C_{ijkm}^{c,n}(t')(1 - e^{-\frac{t-t'}{\tau_n}}) \frac{d\sigma_{km}}{dt'} dt' \tag{3.49}$$

where the creep compliance tensor $C^{c,n}$ can be expressed in a way similar to the elastic compliance tensor in Eq. (3.3), i.e.

$$C_{ijkm}^{c,n}(t') = \rho_c^n(t')\delta_{ij}\delta_{km} + \kappa_c^n(t')(\delta_{ik}\delta_{jm} + \delta_{im}\delta_{jk}) \tag{3.50}$$

in which $\rho_c^n(t')$ and $\kappa_c^n(t')$ are creep compliance parameters which, analogously to Eqs. (3.4) and (3.5), can be expressed as

$$\rho_c^n(t') = -v_n(t')F_n(t') \tag{3.51}$$

$$\kappa_c^n(t') = \frac{1+v_n(t')}{2}\, F_n(t') \tag{3.52}$$

where $F_n(t')$ are the uniaxial creep compliance parameters of Eq. (3.48) and $v_n(t')$ are quantities analogous to Poisson's ratio v. In the absence of detailed experimental results one may assume that $v_n(t') = v$, as e.g. Anderson [1].

Eq. (3.49) is known as a convolution. Using standard notation this equation can be written

$$\epsilon_{ij}^c = \sum_{n=1}^N C_{ijkm}^{c,n}(t)\, \frac{d\sigma_{km}}{dt} * (1 - e^{-\frac{t}{\tau_n}}) \tag{3.53}$$

Since differentiation of a convolution $f(t) * g(t)$ with respect to time yields $\frac{d}{dt}(f(t) * g(t)) = \frac{df(t)}{dt} * g(t) = f(t) * \frac{dg(t)}{dt}$ Eq. (3.53) yields

$$\dot{\epsilon}_{ij}^c = \sum_{n=1}^N C_{ijkm}^{c,n}(t)\, \frac{d\sigma_{km}}{dt} * \frac{1}{\tau_n}\, e^{-\frac{t}{\tau_n}} \tag{3.54}$$

Eq. (3.54) can then be rewritten as

$$\dot{\epsilon}_{ij}^c = \sum_{n=1}^N \frac{1}{\tau_n}\, e^{-\frac{t}{\tau_n}}\, \gamma_{ij}^n(t) \tag{3.55}$$

where the quantities γ_{ij}^n represent the history of the material and are given by

$$\gamma_{ij}^{n}(t) = \int_{0}^{t} C_{ijkm}^{c,n}(t') \; e^{\frac{t'}{\tau_n}} \frac{d\sigma_{km}}{dt'} \; dt' \qquad (3.56)$$

When the creep strain rate at time $t + \Delta t$ is to be computed by use of Eq. (3.55) the integral of Eq. (3.56) has to be evaluated only from time t to time $t + \Delta t$, if the value of the integral at time t is known. This means that the stress history before time t need not be available when the creep strain rate at time $t + \Delta t$ is to be computed.

3.6 Stress-strain relation

In the previous sections, expressions have been obtained for the quantities on the right hand side of Eq. (3.1). In order to obtain a relation between the stress rate $\dot{\sigma}$ and the total strain rate $\dot{\epsilon}$ the previous expressions will be combined. Substitution of Eqs. (3.8) and (3.37) into Eq. (3.1) yields

$$\dot{\epsilon}_{ij} = (C_{ijkm}^{e} + a_{pi} a_{qj} \bar{C}_{pqrs}^{f} a_{rk} a_{sm}) \dot{\sigma}_{km} + \dot{\epsilon}_{ij}^{0} \qquad (3.57)$$

where

$$\dot{\epsilon}_{ij}^{0} = \dot{\epsilon}_{ij}^{T} + \dot{\epsilon}_{ij}^{w} + \dot{\epsilon}_{ij}^{c} + \dot{\epsilon}_{ij}^{t} \qquad (3.58)$$

Since the tensor C^{e} is isotropic, i.e. its components do not change under rotation of the coordinate axes, Eq. (3.57) can be written as

$$\dot{\epsilon}_{ij} = a_{pi} a_{qj} \bar{C}_{pqrs} a_{rk} a_{sm} \dot{\sigma}_{km} + \dot{\epsilon}_{ij}^{0} \qquad (3.59)$$

where

$$\bar{C}_{pqrs} = C^{e}_{pqrs} + \bar{C}^{f}_{pqrs} \tag{3.60}$$

Eq. (3.59) can be used to determine the strain rate when the stress rate is given. In order to obtain a finite element formulation, we are however, interested in the inverse relation. Therefore we introduce the stiffness tensor $\bar{D}$ which is the inverse of the compliance tensor $\bar{C}$, given by

$$\bar{D}_{tupq}\bar{C}_{pqrs} = \frac{1}{2}(\delta_{tr}\delta_{us} + \delta_{ts}\delta_{ur}) \tag{3.61}$$

Since it is complicated to obtain the components of $\bar{D}$ analytically an explicit expression will not be given here. Multiplication of Eq. (3.59) by $a_{vn}a_{wo}\bar{D}_{vwtu}a_{ti}a_{uj}$, use of the relations $a_{ik}a_{jk} = \delta_{ij}$, $a_{ik}a_{im} = \delta_{km}$, $\dot{\sigma}_{km} = \dot{\sigma}_{mk}$ and Eq. (3.61), rearrangement and change of the summation indices yields the following relation between stress rate $\dot{\sigma}$ and strain rate $\dot{\epsilon}$

$$\dot{\sigma}_{km} = D_{kmij}\dot{\epsilon}_{ij} - \dot{\sigma}^{0}_{km} \tag{3.62}$$

where the material stiffness tensor $\mathbf{D}$ and the pseudo stress rate tensor $\dot{\sigma}^{0}$ are given by

$$D_{kmij} = a_{rk}a_{sm}\bar{D}_{rspq}a_{pi}a_{qj} \tag{3.63}$$

$$\dot{\sigma}^{0}_{km} = D_{kmij}\dot{\epsilon}^{0}_{ij} \tag{3.64}$$

The constitutive equations described in this chapter can be used to compute the material stiffness and the pseudo stress rate in order to establish a finite element formulation for concrete structures. If the strain distribution is known the equations can also be used to compute the obtained stress. In the finite

element formulation in the next chapter and in the following applications the present material model will be used.

3.7   Matrix formulation of the constitutive equations

For computer programming matrix formulation is in general most convenient. Using matrix notation the proposed constitutive equations will be summarized below.

Since the tensors $\dot{\sigma}$, $\dot{\epsilon}$ and $\dot{\epsilon}^0$ are symmetric the previous equations can be expressed by using 6-element column matrices for these quantities, i.e.

$$\dot{\sigma} = [\dot{\sigma}_{11} \quad \dot{\sigma}_{22} \quad \dot{\sigma}_{33} \quad \dot{\sigma}_{12} \quad \dot{\sigma}_{23} \quad \dot{\sigma}_{31}]^T \tag{3.65}$$

$$\dot{\epsilon} = [\dot{\epsilon}_{11} \quad \dot{\epsilon}_{22} \quad \dot{\epsilon}_{33} \quad 2\dot{\epsilon}_{12} \quad 2\dot{\epsilon}_{23} \quad 2\dot{\epsilon}_{31}]^T \tag{3.66}$$

$$\dot{\epsilon}_0 = [\dot{\epsilon}^0_{11} \quad \dot{\epsilon}^0_{22} \quad \dot{\epsilon}^0_{33} \quad 2\dot{\epsilon}^0_{12} \quad 2\dot{\epsilon}^0_{23} \quad 2\dot{\epsilon}^0_{31}]^T \tag{3.67}$$

where it should be noted that the shear strain quantities have been multiplied by 2. Noting that $\bar{C}_{pqrs} = \bar{C}_{qprs}$ and $\bar{C}_{pqrs} = \bar{C}_{pqsr}$ it can be verified that Eq. (3.59), using matrix notation, can be written

$$\dot{\epsilon} = \bar{G} \, \bar{C} \, \bar{G}^T \, \dot{\sigma} + \dot{\epsilon}_0 \tag{3.68}$$

where

$$\bar{G} = \begin{bmatrix} a_{11}a_{11} & a_{21}a_{21} & a_{31}a_{31} & a_{11}a_{21} & a_{21}a_{31} & a_{31}a_{11} \\ a_{12}a_{12} & a_{22}a_{22} & a_{32}a_{32} & a_{12}a_{22} & a_{22}a_{32} & a_{32}a_{12} \\ a_{13}a_{13} & a_{23}a_{23} & a_{33}a_{33} & a_{13}a_{23} & a_{23}a_{33} & a_{33}a_{13} \\ 2a_{11}a_{12} & 2a_{21}a_{22} & 2a_{31}a_{32} & a_{11}a_{22}{+}a_{21}a_{12} & a_{21}a_{32}{+}a_{31}a_{22} & a_{31}a_{12}{+}a_{11}a_{32} \\ 2a_{12}a_{13} & 2a_{22}a_{23} & 2a_{32}a_{33} & a_{12}a_{23}{+}a_{22}a_{13} & a_{22}a_{33}{+}a_{32}a_{23} & a_{32}a_{13}{+}a_{12}a_{33} \\ 2a_{13}a_{11} & 2a_{23}a_{21} & 2a_{33}a_{31} & a_{13}a_{21}{+}a_{23}a_{11} & a_{23}a_{31}{+}a_{33}a_{21} & a_{33}a_{11}{+}a_{13}a_{31} \end{bmatrix}$$

$$(3.69)$$

$$\bar{C} = \begin{bmatrix} \bar{C}_{1111} & \bar{C}_{1122} & \bar{C}_{1133} & 2\bar{C}_{1112} & 2\bar{C}_{1123} & 2\bar{C}_{1131} \\ \bar{C}_{2211} & \bar{C}_{2222} & \bar{C}_{2233} & 2\bar{C}_{2212} & 2\bar{C}_{2223} & 2\bar{C}_{2231} \\ \bar{C}_{3311} & \bar{C}_{3322} & \bar{C}_{3333} & 2\bar{C}_{3312} & 2\bar{C}_{3323} & 2\bar{C}_{3331} \\ 2\bar{C}_{1211} & 2\bar{C}_{1222} & 2\bar{C}_{1233} & 4\bar{C}_{1212} & 4\bar{C}_{1223} & 4\bar{C}_{1231} \\ 2\bar{C}_{2311} & 2\bar{C}_{2322} & 2\bar{C}_{2333} & 4\bar{C}_{2312} & 4\bar{C}_{2323} & 4\bar{C}_{2331} \\ 2\bar{C}_{3111} & 2\bar{C}_{3122} & 2\bar{C}_{3133} & 4\bar{C}_{3112} & 4\bar{C}_{3123} & 4\bar{C}_{3131} \end{bmatrix}$$

$$(3.70)$$

Defining G and $\bar{D}$, where

$$G=\bar{G}^{-1}=\begin{bmatrix} a_{11}a_{11} & a_{12}a_{12} & a_{13}a_{13} & a_{11}a_{12} & a_{12}a_{13} & a_{13}a_{11} \\ a_{21}a_{21} & a_{22}a_{22} & a_{23}a_{23} & a_{21}a_{22} & a_{22}a_{23} & a_{23}a_{21} \\ a_{31}a_{31} & a_{32}a_{32} & a_{33}a_{33} & a_{31}a_{32} & a_{32}a_{33} & a_{33}a_{31} \\ 2a_{11}a_{21} & 2a_{12}a_{22} & 2a_{13}a_{23} & a_{11}a_{22}{+}a_{12}a_{21} & a_{12}a_{23}{+}a_{13}a_{22} & a_{13}a_{21}{+}a_{11}a_{23} \\ 2a_{21}a_{31} & 2a_{22}a_{32} & 2a_{23}a_{33} & a_{21}a_{32}{+}a_{22}a_{31} & a_{22}a_{33}{+}a_{23}a_{32} & a_{23}a_{31}{+}a_{21}a_{33} \\ 2a_{31}a_{11} & 2a_{32}a_{12} & 2a_{33}a_{13} & a_{31}a_{12}{+}a_{32}a_{11} & a_{32}a_{13}{+}a_{33}a_{12} & a_{33}a_{11}{+}a_{31}a_{13} \end{bmatrix}$$

$$(3.71)$$

$$\bar{D} = \bar{C}^{-1} \tag{3.72}$$

and premultiplying Eq. (3.68) by $G^T DG$ we obtain

$$\dot{\sigma} = D\dot{\epsilon}' - \dot{\sigma}_0 \tag{3.73}$$

where the tangential material stiffness matrix D and the pseudo stress rate matrix $\dot{\sigma}_0$ are given by

$$D = G^T \bar{D} G \tag{3.74}$$

$$\dot{\sigma}_0 = D\dot{\epsilon}_0 \tag{3.75}$$

Using Eq. (3.61) it may be verified that the components of the matrix $\bar{D}$ are given by

$$\bar{D} = \begin{bmatrix} \bar{D}_{1111} & \bar{D}_{1122} & \bar{D}_{1133} & \bar{D}_{1112} & \bar{D}_{1123} & \bar{D}_{1131} \\ \bar{D}_{2211} & \bar{D}_{2222} & \bar{D}_{2233} & \bar{D}_{2212} & \bar{D}_{2223} & \bar{D}_{2231} \\ \bar{D}_{3311} & \bar{D}_{3322} & \bar{D}_{3333} & \bar{D}_{3312} & \bar{D}_{3323} & \bar{D}_{3331} \\ \bar{D}_{1211} & \bar{D}_{1222} & \bar{D}_{1233} & \bar{D}_{1212} & \bar{D}_{1223} & \bar{D}_{1231} \\ \bar{D}_{2311} & \bar{D}_{2322} & \bar{D}_{2333} & \bar{D}_{2312} & \bar{D}_{2323} & \bar{D}_{2331} \\ \bar{D}_{3111} & \bar{D}_{3122} & \bar{D}_{3133} & \bar{D}_{3112} & \bar{D}_{3123} & \bar{D}_{3131} \end{bmatrix}$$

$$\tag{3.76}$$

According to Eqs. (3.60), (3.3) and (3.34) Eq. (3.70) can be written

$$\bar{C} = \begin{bmatrix} c_1 & c_4 & c_4 & 0 & 0 & 0 \\ c_4 & c_2 & c_4 & 0 & 0 & 0 \\ c_4 & c_4 & c_3 & 0 & 0 & 0 \\ c_8 & c_9 & 0 & c_5 & 0 & 0 \\ 0 & c_{10} & c_{11} & 0 & c_6 & 0 \\ c_{13} & 0 & c_{12} & 0 & 0 & c_7 \end{bmatrix} \tag{3.77}$$

where

$$c_1 = \rho_e + 2\kappa_e + J_1 \tag{3.78a}$$

$$c_2 = \rho_e + 2\kappa_e + J_2 \tag{3.78b}$$

$$c_3 = \rho_e + 2\kappa_e + J_3 \tag{3.78c}$$

$$c_4 = \rho_e \tag{3.78d}$$

$$c_5 = 4\kappa_e + 2A_{12} \tag{3.78e}$$

$$c_6 = 4\kappa_e + 2A_{23} \tag{3.78f}$$

$$c_7 = 4\kappa_e + 2A_{31} \tag{3.78g}$$

$$c_8 = 2B_{12} \tag{3.78h}$$

$$c_9 = 2B_{21} \tag{3.78i}$$

$$c_{10} = 2B_{23} \tag{3.78j}$$

$$c_{11} = 2B_{32} \tag{3.78k}$$

$$c_{12} = 2B_{31} \tag{3.78l}$$

$$c_{13} = 2B_{13} \tag{3.78m}$$

It may be noted that the matrix $\bar{\bar{C}}$ is nonsymmetric due to the modelling of shear fracturing. The reason for the nonsymmetry is that the fracturing shear strain is related to the fracturing normal strain, as described in Sec. 3.3. Since $\bar{C}$ is nonsymmetric its inverse, i.e. the matrix $\bar{D}$, and the matrix D will also be nonsymmetric. Computation of the matrix $\bar{D}$ by inverting the matrix $\bar{C}$ analytically is complicated and will not be carried out here. The inversion can, however, be performed numerically.

The matrix $\dot{\epsilon}_0$ defined by Eq. (3.67) can, according to Eq. (3.58) be expressed as a sum of thermal strain rate, moisture induced strain rate, creep strain rate, and strain rate representing the effect of change of elastic properties, i.e.

$$\dot{\epsilon}_0 = \dot{\epsilon}_T + \dot{\epsilon}_w + \dot{\epsilon}_c + \dot{\epsilon}_t \tag{3.79}$$

The matrices $\dot{\epsilon}_T$ and $\dot{\epsilon}_w$, representing thermal strain rate and moisture induced strain rate respectively can according to Eqs. (3.38)-(3.41) be expressed as

$$\dot{\epsilon}_T = \alpha_T \dot{T}(I_0 + \beta_T C_T \sigma) \tag{3.80}$$

$$\dot{\epsilon}_w = \alpha_w \dot{w}(I_0 + \beta_w C_w \sigma) \tag{3.81}$$

with

$$I_0 = [1 \quad 1 \quad 1 \quad 0 \quad 0 \quad 0]^T \tag{3.82}$$

$$
C_T = \begin{bmatrix}
\rho_T + 2\kappa_T & \rho_T & \rho_T & 0 & 0 & 0 \\
\rho_T & \rho_T + 2\kappa_T & \rho_T & 0 & 0 & 0 \\
\rho_T & \rho_T & \rho_T + 2\kappa_T & 0 & 0 & 0 \\
0 & 0 & 0 & 4\kappa_T & 0 & 0 \\
0 & 0 & 0 & 0 & 4\kappa_T & 0 \\
0 & 0 & 0 & 0 & 0 & 4\kappa_T
\end{bmatrix}
\tag{3.83}
$$

$$
C_W = \begin{bmatrix}
\rho_W + 2\kappa_W & \rho_W & \rho_W & 0 & 0 & 0 \\
\rho_W & \rho_W + 2\kappa_W & \rho_W & 0 & 0 & 0 \\
\rho_W & \rho_W & \rho_W + 2\kappa_W & 0 & 0 & 0 \\
0 & 0 & 0 & 4\kappa_W & 0 & 0 \\
0 & 0 & 0 & 0 & 4\kappa_W & 0 \\
0 & 0 & 0 & 0 & 0 & 4\kappa_W
\end{bmatrix}
\tag{3.84}
$$

According to Eqs. (3.55), (3.56) and (3.50) the creep strain rate $\dot{e}_c$ can be written

$$
\dot{e}_c = \sum_{n=1}^{N} \frac{1}{\tau_n} e^{-\frac{t}{\tau_n}} \gamma_c^n(t)
\tag{3.85}
$$

in which

$$
\gamma_c^n(t) = \int_0^t e^{\frac{t'}{\tau_n}} C_c^n \frac{d\sigma}{dt'} \, dt'
\tag{3.86}
$$

$$
C_c^n = \begin{bmatrix}
\rho_c^n + 2\kappa_c^n & \rho_c^n & \rho_c^n & 0 & 0 & 0 \\
\rho_c^n & \rho_c^n + 2\kappa_c^n & \rho_c^n & 0 & 0 & 0 \\
\rho_c^n & \rho_c^n & \rho_c^n + 2\kappa_c^n & 0 & 0 & 0 \\
0 & 0 & 0 & 4\kappa_c^n & 0 & 0 \\
0 & 0 & 0 & 0 & 4\kappa_c^n & 0 \\
0 & 0 & 0 & 0 & 0 & 4\kappa_c^n
\end{bmatrix}
\tag{3.87}
$$

The strain rate representing the effect of change of elastic properties $\dot{e}_t$ can, according to Eqs. (3.9) and (3.10), be expressed as

$$\dot{e}_t = \dot{C}_e \sigma \tag{3.88}$$

in which

$$\dot{C}_e = \begin{bmatrix} \dot{\rho}_e + 2\dot{\kappa}_e & \dot{\rho}_e & \dot{\rho}_e & 0 & 0 & 0 \\ \dot{\rho}_e & \dot{\rho}_e + 2\dot{\kappa}_e & \dot{\rho}_e & 0 & 0 & 0 \\ \dot{\rho}_e & \dot{\rho}_e & \dot{\rho}_e + 2\dot{\kappa}_e & 0 & 0 & 0 \\ 0 & 0 & 0 & 4\dot{\kappa}_e & 0 & 0 \\ 0 & 0 & 0 & 0 & 4\dot{\kappa}_e & 0 \\ 0 & 0 & 0 & 0 & 0 & 4\dot{\kappa}_e \end{bmatrix} \tag{3.89}$$

Eqs. (3.65)-(3.67) and (3.71)-(3.89) give the proposed constitutive equations using matrix notation. As may be noted the matrices C_T, C_w, C_c^n and $\dot{C}_e$ are all given in a form analogous to the elastic part of matrix $\bar{C}$.

4. FINITE ELEMENT FORMULATION AND SOLUTION PROCEDURE

4.1 Introduction

In the previous chapter constitutive equations for concrete have been proposed. These equations will in the present chapter be used in the establishment of a finite element formulation which will be given in rate form. In order to perform the time integration of the finite element equations an incremental numerical solution procedure will be used. In the formulation of tensile fracture in Sec. 3.3 an equivalent length was introduced. This length is related to the size and shape of the finite element where the fracture occurs and will also be described. The chapter is concluded by a description of the computer program used in the applications.

4.2 Basic equations

In order to arrive at an appropriate finite element formulation the basic equations of nonlinear structural analysis will be briefly described.

The equations of equilibrium are

$$\frac{\partial \sigma_{ji}}{\partial x_j} + f_i = 0 \tag{4.1}$$

where σ is the stress tensor, f is the vector representing body force per unit volume and x_j denotes a Cartesian coordinate system. Eq. (4.1) is multiplied by a set of weighting functions v_{im} and an integration over the studied body volume V is performed

$$\int_V v_{im} \frac{\partial \sigma_{ji}}{\partial x_j} \, dV + \int_V v_{im} f_i dV = 0 \tag{4.2}$$

It should be noted that the index m may normally assume values exceeding 3. Use of the divergence theorem gives the relation

$$\int_V \frac{\partial v_{im}}{\partial x_j} \sigma_{ji} dV = \int_S v_{im} t_i dS + \int_V v_{im} f_i dV \tag{4.3}$$

where **t** is the traction vector defined by

$$t_i = \sigma_{ji} n_j \tag{4.4}$$

where **n** is the outward unit vector normal to the surface S of the studied body. As Eq. (4.1) also applies in rate form and v_{im} is assumed to be constant with respect to time it follows directly from Eq. (4.3) that

$$\int_V \frac{\partial v_{im}}{\partial x_j} \dot{\sigma}_{ji} dV = \int_S v_{im} \dot{t}_i dS + \int_V v_{im} \dot{f}_i dV \tag{4.5}$$

The stress rate is related to the strain rate through the constitutive equations, as described in Chapter 3. The relation to be used may in general be expressed as (cf. Eq. (3.62))

$$\dot{\sigma}_{ij} = D_{ijpq} \dot{\epsilon}_{pq} - \dot{\sigma}_{ij}^0 \tag{4.6}$$

where **D** is the tangential material stiffness tensor, $\dot{\epsilon}$ is the strain rate tensor and $\dot{\sigma}^0$ is the rate of pseudo stress tensor. The strain rate $\dot{\epsilon}$ is assumed to be given by the linear kinematic relation

$$\dot{\epsilon}_{pq} = \frac{1}{2} \left(\frac{\partial \dot{u}_p}{\partial x_q} + \frac{\partial \dot{u}_q}{\partial x_p} \right) \tag{4.7}$$

where **u** is the displacement vector.

Eqs. (4.5), (4.6) and (4.7) are combined to form

$$\int_V \frac{\partial v_{im}}{\partial x_j} D_{jipq} \frac{1}{2}(\frac{\partial \dot{u}_p}{\partial x_q} + \frac{\partial \dot{u}_q}{\partial x_p})dV = \int_S v_{im}\dot{t}_i dS +$$

$$+ \int_V v_{im}\dot{f}_i dV + \int_V \frac{\partial v_{im}}{\partial x_j} \dot{\sigma}_{ji}^0 dV \qquad (4.8)$$

Since the stress and strain rate tensors $\dot{\sigma}$ and $\dot{\epsilon}$ are symmetric the material stiffness tensor D has the symmetry properties

$$D_{ijpq} = D_{jipq} \qquad (4.9)$$

$$D_{ijpq} = D_{ijqp} \qquad (4.10)$$

Due to these symmetry properties Eq. (4.8) can be written as

$$\int_V \frac{\partial v_{im}}{\partial x_j} D_{ijpq} \frac{\partial \dot{u}_p}{\partial x_q} dV = \int_S v_{im}\dot{t}_i dS + \int_V v_{im}\dot{f}_i dV +$$

$$+ \int_V \frac{\partial v_{im}}{\partial x_j} \dot{\sigma}_{ij}^0 dV \qquad (4.11)$$

This is a weak formulation which will be used to obtain the finite element equations in the next section.

4.3   Finite element equations in matrix form

In order to obtain finite element equations the displacements u are expressed in an approximate way as a function of so called nodal displacements $\bar{u}_n$ as

$$u_p = N_{pn}\bar{u}_n \qquad (4.12)$$

where N_{pn} are interpolation functions which are assumed to be constant with respect to time. The summation index n in Eq. (4.12) may normally exceed 3. Differentiation of Eq. (4.12) with respect to time yields

$$\dot{u}_p = N_{pn}\dot{\bar{u}}_n \qquad (4.13)$$

According to the Galerkin method the interpolation functions are chosen as weighting functions, i.e.

$$v_{im} = N_{im} \qquad (4.14)$$

Substitution of Eqs. (4.13) and (4.14) into Eq. (4.11) yields

$$K_{mn}\dot{\bar{u}}_n = \dot{P}_m + \dot{P}_m^O \qquad (4.15)$$

where K_{mn}, $\dot{P}_m$ and $\dot{P}_m^O$ are tangential stiffness, rate of load and rate of pseudo load given by

$$K_{mn} = \int_V \frac{\partial N_{im}}{\partial x_j} D_{ijpq} \frac{\partial N_{pn}}{\partial x_q} dV \qquad (4.16)$$

$$\dot{P}_m = \int_S N_{im}\dot{t}_i dS + \int_V N_{im}\dot{f}_i dV \qquad (4.17)$$

$$\dot{P}_m^O = \int_V \frac{\partial N_{im}}{\partial x_j} \dot{\sigma}_{ij}^O dV \qquad (4.18)$$

For computer programming matrix notations are in general most convenient. In order to rewrite Eqs. (4.16)-(4.18) using matrix notations and to reduce the number of terms in the summations we define the matrices N_n, $\tilde{v}$, B_n, $\dot{t}$ and $\dot{f}$ as

$$N_n = \begin{bmatrix} N_{1n} & N_{2n} & N_{3n} \end{bmatrix}^T \tag{4.19}$$

$$\tilde{\nabla} = \begin{bmatrix} \dfrac{\partial}{\partial x_1} & 0 & 0 & \dfrac{\partial}{\partial x_2} & 0 & \dfrac{\partial}{\partial x_3} \\[3mm] 0 & \dfrac{\partial}{\partial x_2} & 0 & \dfrac{\partial}{\partial x_1} & \dfrac{\partial}{\partial x_3} & 0 \\[3mm] 0 & 0 & \dfrac{\partial}{\partial x_3} & 0 & \dfrac{\partial}{\partial x_2} & \dfrac{\partial}{\partial x_1} \end{bmatrix}^T \tag{4.20}$$

$$B_n = \tilde{\nabla} N_n = \begin{bmatrix} \dfrac{\partial N_{1n}}{\partial x_1} & \dfrac{\partial N_{2n}}{\partial x_2} & \dfrac{\partial N_{3n}}{\partial x_3} & \dfrac{\partial N_{1n}}{\partial x_2} + \dfrac{\partial N_{2n}}{\partial x_1} & \dfrac{\partial N_{2n}}{\partial x_3} + \dfrac{\partial N_{3n}}{\partial x_2} & \dfrac{\partial N_{1n}}{\partial x_3} + \dfrac{\partial N_{3n}}{\partial x_1} \end{bmatrix}^T \tag{4.21}$$

$$\dot{t} = \begin{bmatrix} \dot{t}_1 & \dot{t}_2 & \dot{t}_3 \end{bmatrix}^T \tag{4.22}$$

$$\dot{f} = \begin{bmatrix} \dot{f}_1 & \dot{f}_2 & \dot{f}_3 \end{bmatrix}^T \tag{4.23}$$

Noting the symmetry properties given by Eqs. (4.9) and (4.10) Eqs. (4.16)–(4.18) can be expressed as

$$K_{mn} = \int_V B_m^T D B_n \, dV \tag{4.24}$$

$$\dot{P}_m = \int_S N_m^T \dot{t} \, dS + \int_V N_m^T \dot{f} \, dV \tag{4.25}$$

$$\dot{P}_m^0 = \int_V B_m^T \dot{\sigma}_0 \, dV \tag{4.26}$$

where the matrices D and $\dot{\sigma}_0$ are defined by Eqs. (3.74) and (3.75).

Finite element formulation and solution procedure

Eq. (4.7) can, using matrix notation, be written as

$$\dot{\epsilon} = \tilde{\nabla} \dot{u} \qquad (4.27)$$

where $\dot{\epsilon}$ is defined by Eq. (3.66) and

$$\dot{u} = [\dot{u}_1 \quad \dot{u}_2 \quad \dot{u}_3]^T \qquad (4.28)$$

By using Eqs. (4.19) and (4.28) Eq. (4.13) can be expressed as

$$\dot{u} = N_n \dot{\bar{u}}_n \qquad (4.29)$$

where n is a summation index which may normally exceed 3. Substitution of Eq. (4.29) into Eq. (4.27) and use of Eq. (4.21) yields the expression

$$\dot{\epsilon} = B_n \dot{\bar{u}}_n \qquad (4.30)$$

which can be used to obtain an approximation of the strains $\dot{\epsilon}$ when the rate of nodal displacements $\dot{\bar{u}}_n$ is known. Knowing the strain rates $\dot{\epsilon}$, we can then determine the stress rates $\dot{\sigma}$ from Eq. (3.73).

By choosing the interpolation functions in such a way that each function is non-zero in a limited subdomain of the studied body and zero elsewhere, the integrations over the volume V and surface S in Eqs. (4.24)-(4.26) can be split up into integrations over subdomains called finite elements. In this way one system of equations is obtained for each finite element. The systems of equations for all elements of the studied body are assembled into a common system of equations representing the whole body.

In the present work three element types are used: three–node triangular element, four–node isoparametric element and eight–node isoparametric element. The choice of nodal displacements and shape functions for these elements may be found in e.g. Zienkiewicz [60] or Bathe [2]. For the isoparametric elements the integrals are evaluated numerically by Gauss quadrature.

4.4   Numerical solution procedure

In the previous section finite element equations have been established in a rate form, cf. Eq. (4.15). In order to determine the nodal displacements $\bar{u}$ at time t this equation is integrated with respect to time using a numerical procedure. For a review of different techniques of solution, see e.g. Stricklin et al. [55] or Bergan and Søreide [10]. Although more sophisticated methods are available, a self–correcting incremental method, which will be briefly described below, is applied for the sake of simplicity.

The numerical solution procedure includes approximations which may result in that the equations of equilibrium are not satisfied exactly. A measure of the deviation is provided by the out–of–balance forces P^*, which are defined as the difference between the right and left hand sides of Eq. (4.3), i.e.

$$P^*_m = \int_S v_{im} t_i dS + \int_V v_{im} f_i dV - \int_V \frac{\partial v_{im}}{\partial x_j} \sigma_{ji} dV \qquad (4.31)$$

Using Eqs. (4.14), (4.19), (4.20) and (4.21) and defining the matrices σ, t and f as

$$\sigma = \begin{bmatrix} \sigma_{11} & \sigma_{22} & \sigma_{33} & \sigma_{12} & \sigma_{23} & \sigma_{31} \end{bmatrix}^T \qquad (4.32)$$

$$t = \begin{bmatrix} t_1 & t_2 & t_3 \end{bmatrix}^T \qquad (4.33)$$

$$f = \begin{bmatrix} f_1 & f_2 & f_3 \end{bmatrix}^T \qquad (4.34)$$

we have

$$P_m^* = P_m - \int_V B_m^T \sigma \, dV \qquad (4.35)$$

where P_m is the sum of the applied external loads given by

$$P_m = \int_S N_m^T t \, dS + \int_V N_m^T f \, dV \qquad (4.36)$$

The last term of Eq. (4.35) represents the internal forces corresponding to the obtained stress σ, which has been computed according to the constitutive equations. The rate of change of the out-of-balance forces P_m^* is given by the time derivative of Eq. (4.35), i.e.

$$\dot{P}_m^* = \dot{P}_m - \int_V B_m^T \dot{\sigma} \, dV \qquad (4.37)$$

where $\dot{P}_m$ and $\dot{\sigma}$ are given by Eqs. (4.25) and (3.65) respectively. Use of Eqs. (3.73) and (4.30) and rearrangement yields

$$K_{mn} \dot{\bar{u}}_n = \dot{P}_m + \dot{P}_m^0 - \dot{P}_m^* \qquad (4.38)$$

where K_{mn} and $\dot{P}_m^0$ are the tangential stiffness and rate of pseudo load given by Eqs. (4.24) and (4.26), respectively. Evaluation of Eq. (4.38) can be performed by an Euler forward expression, assuming a linear relation from time t to time $t+\Delta t$, i.e.

$$K_{mn}(t)\Delta\bar{u}_n = \Delta P_m + \Delta t\dot{P}_m^0(t) - \Delta t\dot{P}_m^* \tag{4.39}$$

where $K_{mn}(t)$ is the tangential stiffness at time t, $\Delta\bar{u}_n$ the change of nodal displacements from time t to time $t+\Delta t$, $\dot{P}_m^0(t)$ the rate of pseudo load at time t and ΔP_m the incremental load, which is given by

$$\Delta P_m = \int_t^{t+\Delta t} \dot{P}_m dt \tag{4.40}$$

In order to guide the solution towards the true solution, we want the out-of-balance forces $P_m^*(t)$ at time t to reduce to zero during the time increment. Therefore the rate of change of the out-of-balance forces is assumed to be

$$\dot{P}_m^* = -\frac{1}{\Delta t} P_m^*(t) \tag{4.41}$$

Substitution of Eq. (4.41) into Eq. (4.39) yields

$$K_{mn}(t)\Delta\bar{u}_n = \Delta P_m + \Delta t\dot{P}^0(t) + P_m^*(t) \tag{4.42}$$

This procedure is described by Stricklin et al. [55] and is called a self-correcting solution form, since the solution is guided towards the true solution.

By making $\dot{P}_m^* = 0$ in Eq. (4.39) we obtain a purely incremental stiffness method which yields solutions with a tendency to drift away from the true solutions because of the increasing out-of-balance forces. As pointed out by Stricklin et al. [55] considerably better results are obtained by the self-correcting form than by the purely incremental form.

4.5   Definition of equivalent length

Now, when the finite element formulation as well as the numerical solution procedure have been established, we shall return to the equivalent length which was introduced in the formulation of fracturing strain in Sec. 3.3.

In Eqs. (3.19) and (3.28) the fracturing strain was defined as the mean strain caused by fracture in a region which includes the crack. In the present section we will discuss the way in which the equivalent length can be related to the size and shape of the finite element where the fracture occurs. Considering a two-node bar element, which due to the shape functions has a uniform strain distribution, the total elongation $\bar{w}_1$, caused by fracture is given by the integral of the mean fracture strain $\bar{\epsilon}_{11}^f$ over the element length L, i.e.

$$\bar{w}_1 = \int_0^L \bar{\epsilon}_{11}^f d\bar{x} = L\bar{\epsilon}_{11}^f \tag{4.45}$$

In Eq. (3.19) the fracturing strain was related to the crack width by the equivalent length L_1. Substitution of Eq. (3.19) into Eq. (4.45) yields

$$L_1 = L \tag{4.46}$$

i.e. the equivalent length L_1 is equal to the length of the bar element. By the same type of reasoning and a rectangular element with a crack plane parallel to one of the edges, the equivalent lengths of Eq. (3.28), relating fracturing shear strain and shear crack displacement, can be shown to be the length of the element in the $\bar{x}$- and $\bar{y}$-directions. These observations lead to a general definition of equivalent length. The equivalent length

corresponding to a crack is the maximum length in the direction normal to the crack plane of the element region of interest. This definition was introduced by Ottosen and Dahlblom [44] and is illustrated in Fig. 4.1 for a three-node triangular element and four-node and eight-node isoparametric elements.
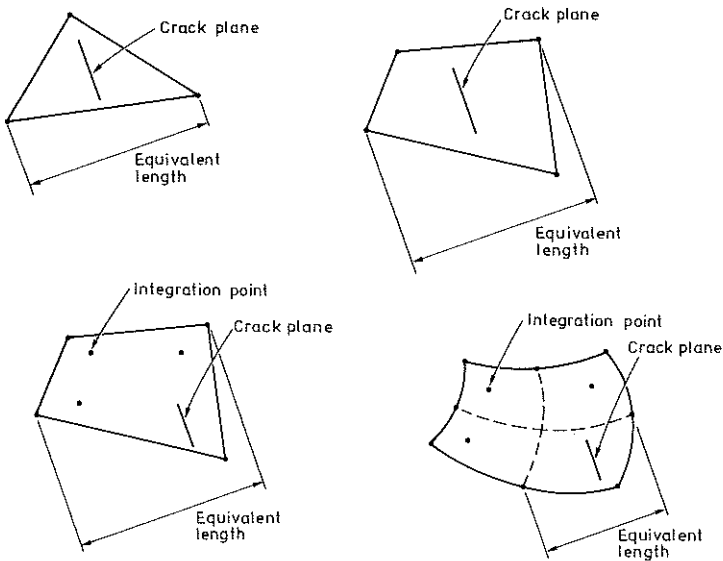
Fig. 4.1. Illustration of equivalent length.

It should be noted that the whole four-node element is considered both when one integration point is used and when four integration points are used. When fracture has been initiated at one integration point in a four-node element with four integration points and the element is subjected to an increasing elongation, fracture will, due to the shape functions, in general occur also at the other integration points. Since the strain distribution in a four-node element is almost constant, an element where fracture has been initiated at all the integration points should be given stiffness properties corresponding to one crack plane inside the element. When the crack width is determined according to Eq.

(3.19) the fracturing strain is consequently related to the whole element length. On the other hand, for an eight-node element the region bounded by the nodal points closest to the integration point in question and the element mid-point are considered. This is because this element type, in contrast to the four-node element, is suitable for description of the variation of strain inside the element, corresponding e.g. to fracture development in one integration point and elastic unloading in another.

The proposed definition of equivalent length is applied in the computations in the present study. In Chapter 5 a simulation of a concrete tension specimen is performed, which aims to reflect the input value of fracture energy. The results show considerable improvement compared with those obtained by Oldenburg [41] where another concept which corresponds to making the equivalent length for a two-dimensional element equal to the square root of the element area, is used for relating the crack width to the element strain. This approach does not, however, consider the influence of the element shape in a proper way.

In the present work the proposed concept has been applied only to two-dimensional problems. Three-dimensional analysis can, however, be performed using the same concept.

4.6   Computer program

In order to perform numerical studies in material and structural mechanics using an established theory, a computer has normally to be used. When new formulations are to be applied, computer code development is often necessary. Since programming is time consuming it is desirable to minimize the code development and use existing computer code to a large extent in order that results may be obtained rapidly. The aim of the computer program CAMFEM (Computer Aided Modelling based on the Finite Element Method) Dahlblom and Peterson [18] is to provide a problem

independent program structure which can easily be supplemented with problem dependent program modules. To facilitate complete user control over the computational procedure the program is based on a command language, i.e. the computational procedure is defined by commands given by the user. The problem independent program structure includes commands for facilities needed in most computations. By supplementing the problem independent program structure with problem dependent program modules a special purpose program can be rapidly obtained. CAMFEM has been successfully used in different classes of problems, see e.g. Refs. [16], [42], [47], [54], [56].

During the course of the present study CAMFEM has been revised, Dahlblom and Peterson [19]. The new program version includes facilities of the program CALFEM, Dahlblom et al. [20], [21], which is an interactive computer program designed as a tool for teaching the finite element method. The facilities common to the two programs are accessed by identical commands.

In previous work, see Dahlblom [17], a library of material models for finite element analysis has been developed. The constitutive model proposed in the present work may be regarded as a supplement to this library. In the present work the problem independent program structure of CAMFEM has been supplemented by commands for the constitutive equations described in Chapter 3 and commands for the three different types of finite elements applied according to the guidelines proposed by Dahlblom [16]. For operations like input and output of data, matrix handling and solution of systems of equations, the facilities in the problem independent program structure are used. The program CAMFEM is briefly described in Appendix B.

5. SIMULATION OF CONCRETE TENSION SPECIMEN

5.1 Introduction

In this chapter the behaviour of a concrete tension specimen is simulated, in order to document that the smeared crack approach now proposed, reflects the assumed value of fracture energy per unit area.

The concrete tension specimen shown in Fig. 5.1 is analysed. The geometry of the specimen is the same as that of the specimens used in tests by Petersson [48]. Owing to symmetry only one quarter of the specimen is considered.
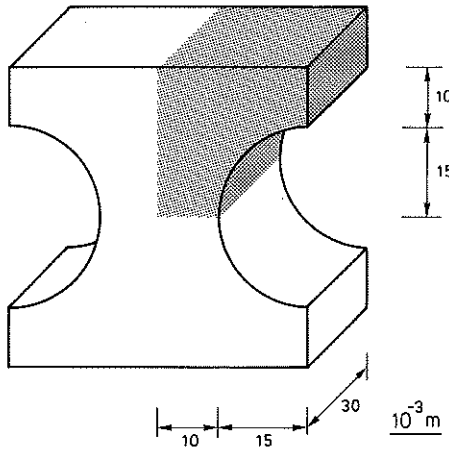

Fig. 5.1. Analysed concrete specimen

In the analysis the material is assumed to be characterized by the parameters $E = 2.1 \cdot 10^{10}$ Pa, $\nu = 0.2$, $f_t = 3.3 \cdot 10^6$ Pa, $G_F = 130.0$ N/m, $G_s = 3.8 \cdot 10^6$ Pa and $\gamma_f = 1.0$. Plane stress conditions are assumed.

The specimen is analysed using a three-node triangular element, a four-node isoparametric element and an eight-node isoparametric element. For each element type the specimen is analysed using a set of different element meshes. The analysis simulates a tensile test where the specimen is subjected to an increasing displacement δ. The boundary conditions used in the analysis are illustrated in Fig. 5.2.
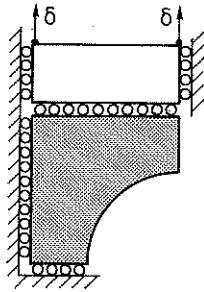
Fig. 5.2. Boundary conditions.

During the analysis the total vertical force P on the specimen varies with the prescribed displacement δ. The integral of P from zero displacement up to the displacement for which the specimen is fully cracked is the dissipated energy. By dividing the dissipated energy by the cross sectional area at the crack plane an estimate of the fracture energy is obtained. For decreasing element sizes the estimated value of the fracture energy should converge towards the input value of the fracture energy. For some of the computational results the value of the force does not reach zero but stabilizes at a positive value. In order to get a finite value of the dissipated energy for these computations the "tail" of the force-displacement curve is replaced by a straight line tangential to the curve at the point where the slope starts to decrease.

In the figures with crack patterns the symbols denote crack directions. Thick crack symbols denote developing or fully developed cracks.

5.2   Analysis with regular meshes

For the three-node triangular element the meshes shown in Fig. 5.3 are used. In the figure the crack patterns at the termination of computation are also shown.

Mesh A1   Mesh A2   Mesh A3   Mesh A4
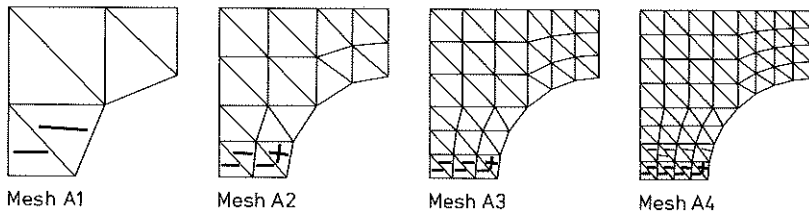
Fig. 5.3.   Finite element meshes and crack patterns for the three-node triangular element.

The force-displacement curves for the meshes of Fig. 5.3 are shown in Fig. 5.4 and the estimated values of the fracture energy are given in Table 5.1.

	Estimate of G_F (N/m)	Deviation from input value
A1	159.4	22.6 %
A2	140.1	7.8 %
A3	135.5	4.2 %
A4	133.5	2.7 %

Table 5.1. Estimated values of fracture energy for computations according to Fig. 5.3.

Force
(10^3 N)

1.00

A1
A2
A3
A4

.50

Displacement
(10^{-6} m)

50.

100.
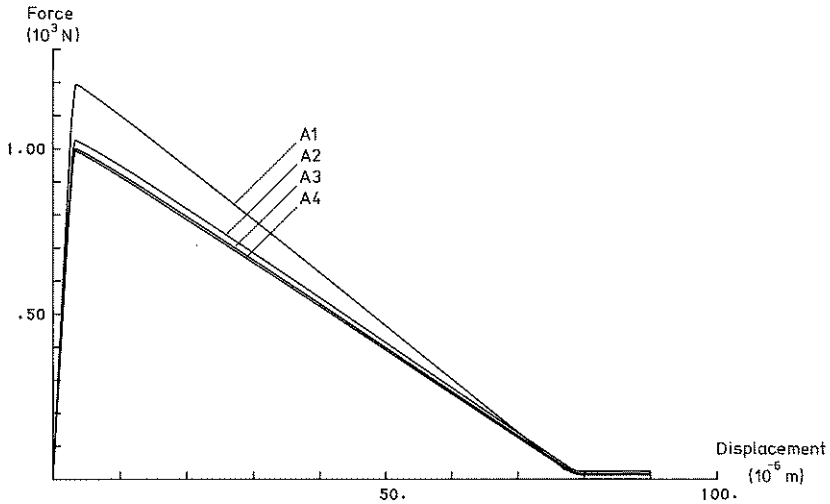
Fig. 5.4.   Force–displacement curves for computation according to
          Fig. 5.3.

For the four–node isoparametric element computations have been
performed with one–point integration as well as with four–point
integration. For one–point integration the element meshes and
the corresponding crack patterns are shown in Fig. 5.5.

The force–displacement curves for the computations corresponding
to Fig. 5.5 are shown in Fig. 5.6 and the estimated fracture
energies are given in Table 5.2.

	Estimate of G_F (N/m)	Deviation from input value
B1	138.9	6.8 %
B2	130.5	0.4 %
B3	128.0	−1.5 %
B4	127.6	−1.8 %

Table 5.2. Estimated values of fracture energy for computations
          according to Fig. 5.5.

Mesh B1   Mesh B2   Mesh B3   Mesh B4

<u>Fig. 5.5.</u> Finite element meshes and crack patterns for the
four-node isoparametric element with one-point
integration.

<u>Fig. 5.6.</u> Force-displacement curves for computations according
to Fig. 5.5.

For four-point integration of the four-node isoparametric element
the element meshes and the corresponding crack patterns are shown
in Fig. 5.7.

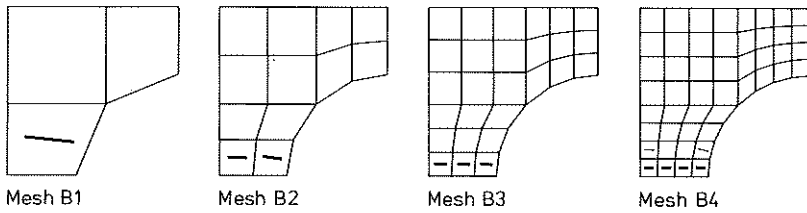Mesh C1   Mesh C2   Mesh C3   Mesh C4

Fig. 5.7. Finite element meshes and crack patterns for the four-node isoparametric element with four-point integration.

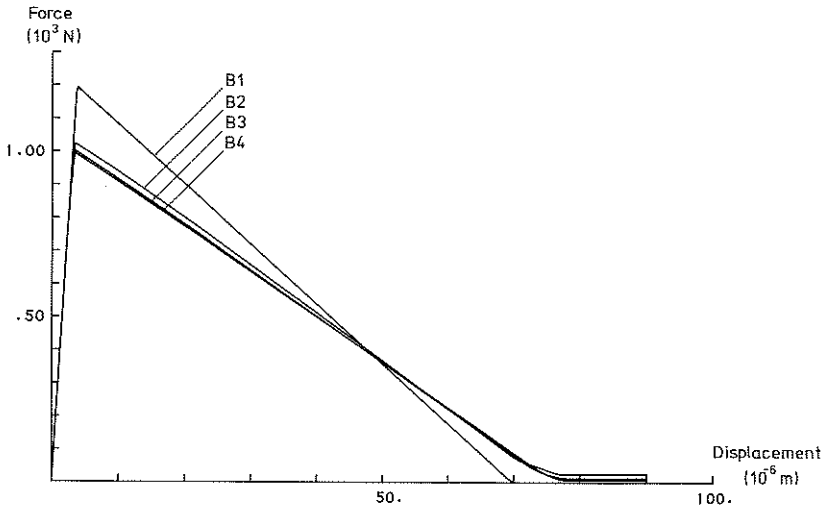The force-displacement curves for the computations corresponding to Fig. 5.7 are shown in Fig. 5.8 and the estimated fracture energies are given in Table 5.3.

Fig. 5.8. Force-displacement curves for computations according to Fig. 5.7.

	Estimate of G_F (N/m)	Deviation from input value
C1	156.4	20.3 %
C2	137.7	5.9 %
C3	132.2	1.7 %
C4	130.3	0.2 %

Table 5.3. Estimated values of fracture energy for computations according to Fig. 5.7.

For the eight-node isoparametric element the meshes shown in Fig. 5.9 are used. In the figure the corresponding crack patterns are shown.

Mesh D1   Mesh D2   Mesh D3
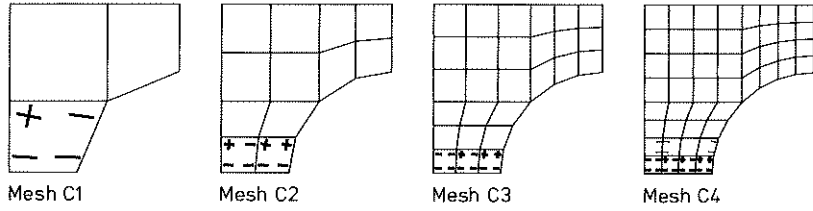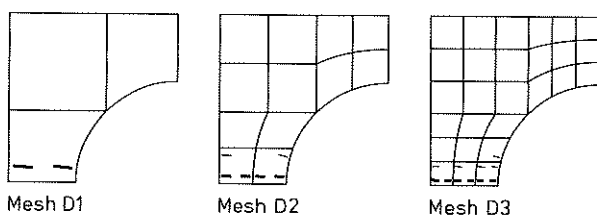
Fig. 5.9. Finite element meshes and crack patterns for the eight-node isoparametric element.

The force-displacement curves for the computations corresponding to Fig. 5.9 are shown in Fig. 5.10 and the estimated values of the fracture energy are given in Table 5.4.
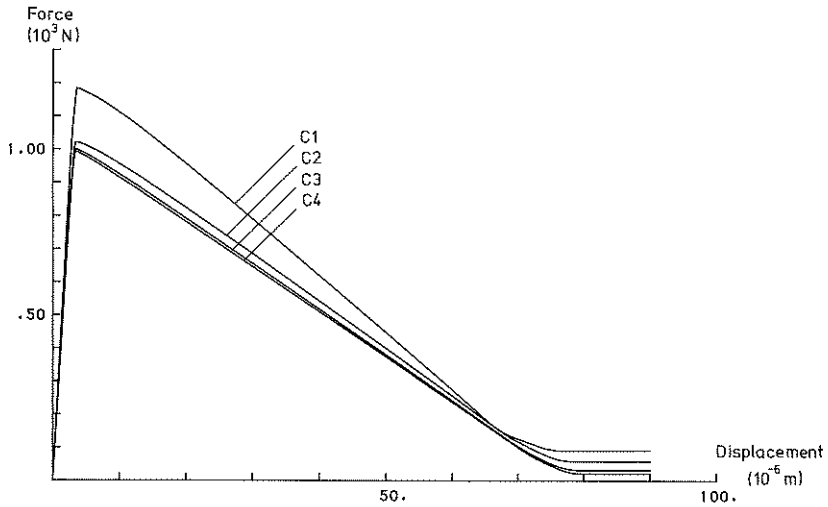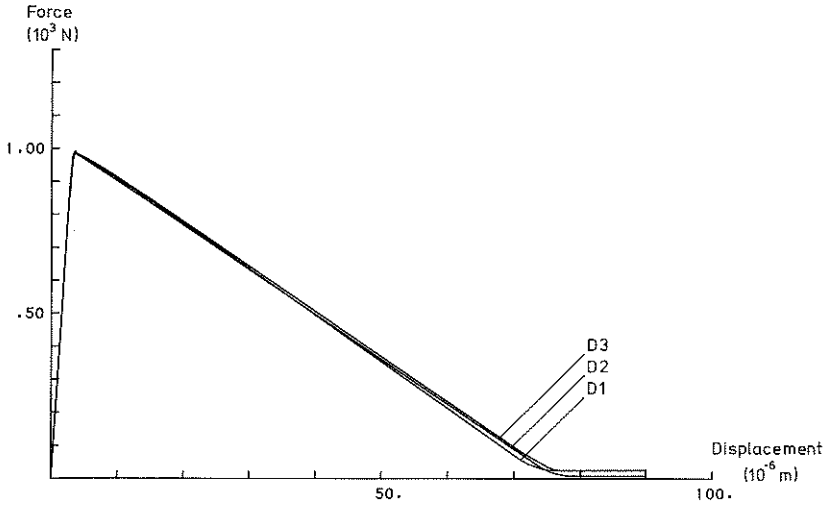
Fig. 5.10. Force-displacement curves for the meshes shown in Fig. 5.9.

	Estimate of G_F (N/m)	Deviation from input value
D1	126.0	-3.1 %
D2	126.8	-2.5 %
D3	129.1	-0.7 %

Table 5.4. Estimated values of fracture energy for computations according to Fig. 5.9.

The estimated values of fracture energy given in Tables 5.1–5.4 are plotted in Fig. 5.11 as a function of the inverted value of the number of equations n_{eq}^{-1}, i.e. for an infinite number of degrees of freedom $n_{eq}^{-1} \rightarrow 0$.

As can be seen in Fig. 5.11 the results for all the element types used show good convergence for mesh refinement.
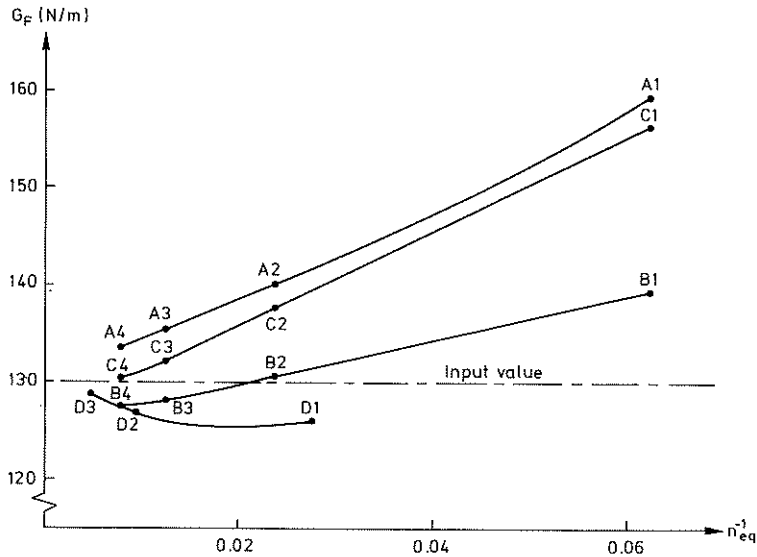
Fig. 5.11. Estimated values of fracture energy as a function of the number of equations.

In the previous computations of the tensile specimen, owing to symmetry, only one quarter of the specimen has been considered. To demonstrate that the same estimate of the fracture energy is obtained if the symmetry is not considered one half of the specimen, corresponding to the right half of Fig. 5.1, is analysed. If the upper and the lower quarter were given exactly the same properties the behaviour of the specimen would be exactly symmetric. It is, however, important that the tensile strength in two integration points is not reached in the same computational step when the total force is about to reach its maximum value. In order to avoid this the structure is given an initial nonsymmetry by a very small change of the coordinates of one nodal point. The finite element mesh used in the analysis corresponds to mesh C3 of Fig. 5.7. The mesh and the corresponding crack pattern is shown in Fig. 5.12. The force-displacement curve for the computation is shown in Fig.
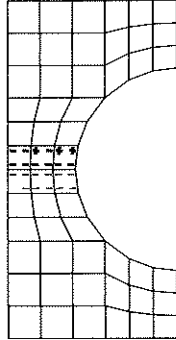
Fig. 5.12. Finite element mesh and corresponding crack pattern for analysis of one half of the tensile concrete specimen.
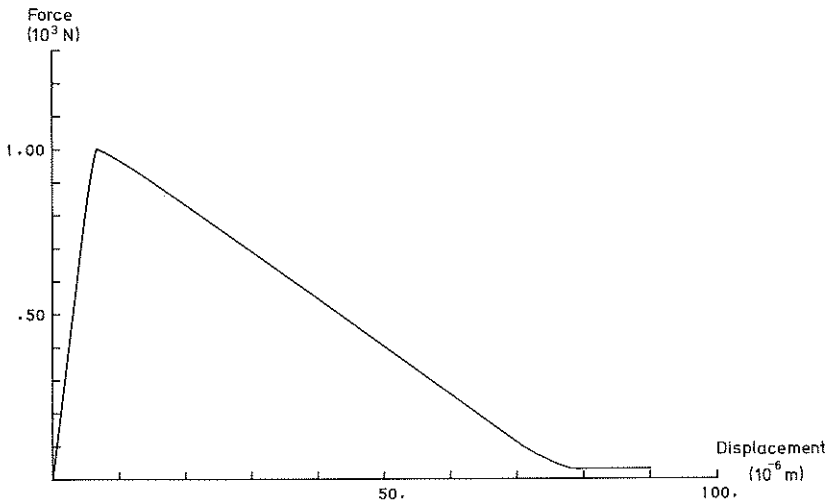
Fig. 5.13. Force-displacement curve for the computation according to Fig. 5.12.

5.13. The estimated value of the fracture energy is $G_{F,est}$ = 133.2 N/m, i.e. practically the same as that obtained for mesh C3 shown in Table 5.3. This demonstrates that the estimated value of the fracture energy is independent of whether or not symmetry is considered.

5.3   Analysis with distorted meshes

In the previous computations regular meshes have been used. In these meshes the cracks develop mainly parallel to element boundaries. To investigate the behaviour in a more general situation distorted meshes have been analysed.

For the three-node triangular element the meshes shown in Fig. 5.14 are used. In the figure the crack patterns at termination of computation are also shown.

Mesh E1   Mesh E2   Mesh E3   Mesh E4
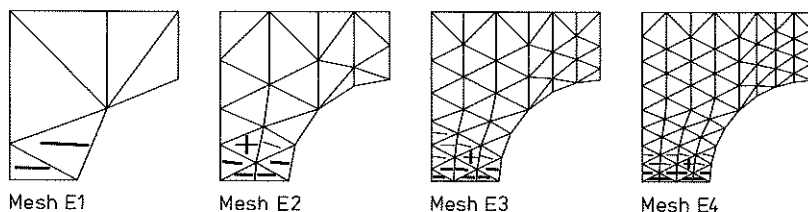
Fig. 5.14. Distorted finite element meshes and crack patterns for the three-node triangular element.

The force-displacement curves for the meshes of Fig. 5.14 are shown in Fig. 5.15 and the estimated values of the fracture energy are given in Table 5.5. It may be noted that rather significant and unrealistic "tails" of the force-displacement curves are predicted, cf. Fig. 5.15.

For the four-node isoparametric element with one-point integration the meshes and the corresponding crack patterns are shown in Fig. 5.16.
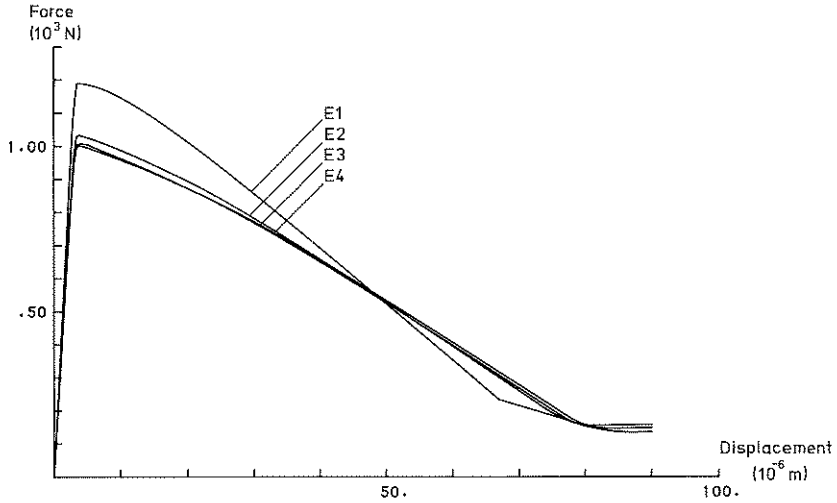
<u>Fig. 5.15</u>. Force-displacement curves for computations according to Fig. 5.14.

	Estimate of G_F (N/m)	Deviation from input value
E1	200.4	54.2 %
E2	166.2	27.8 %
E3	164.7	26.7 %
E4	166.3	27.9 %

<u>Table 5.5</u>. Estimated values of fracture energy for computations according to Fig. 5.14.

The force-displacement curves for the computations corresponding to Fig. 5.16 are shown in Fig. 5.17 and the estimated fracture energies are given in Table 5.6. It may be noted that the "tails" of the force-displacement curves are not as significant as for the three-node element.

Fig. 5.16. Distorted finite element meshes and corresponding
crack patterns for the four-node isoparametric element
with one-point integration.

Fig. 5.17. Force-displacement curves for the computations
according to Fig. 5.16.

For the four-node isoparametric element with four-point
integration the meshes and the corresponding crack patterns are
shown in Fig. 5.18.

	Estimate of G_F (N/m)	Deviation from input value
F1	93.2	–28.3 %
F2	112.8	–13.2 %
F3	108.2	–16.8 %
F4	108.6	–16.5 %

<u>Table 5.6</u>. Estimated values of fracture energy for computations according to Fig. 5.16.

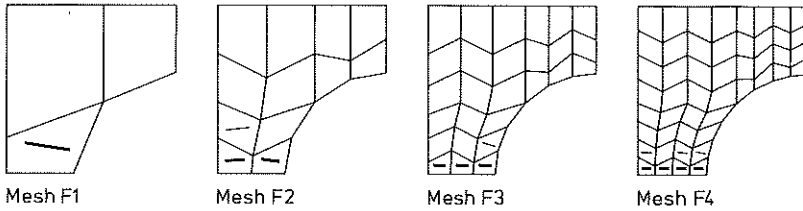Mesh G1   Mesh G2   Mesh G3   Mesh G4
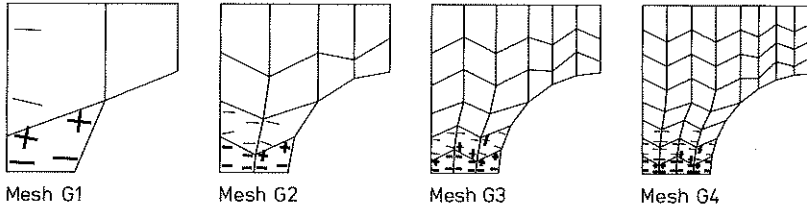
<u>Fig. 5.18</u>. Distorted finite element meshes and corresponding crack patterns for the four–node isoparametric element with four–point integration.

The force–displacement curves for the computations corresponding to Fig. 5.18 are shown in Fig. 5.19 and the estimated fracture energies are given in Table 5.7. Again we observe the prediction of unwanted "tails" of the force–displacement curves.
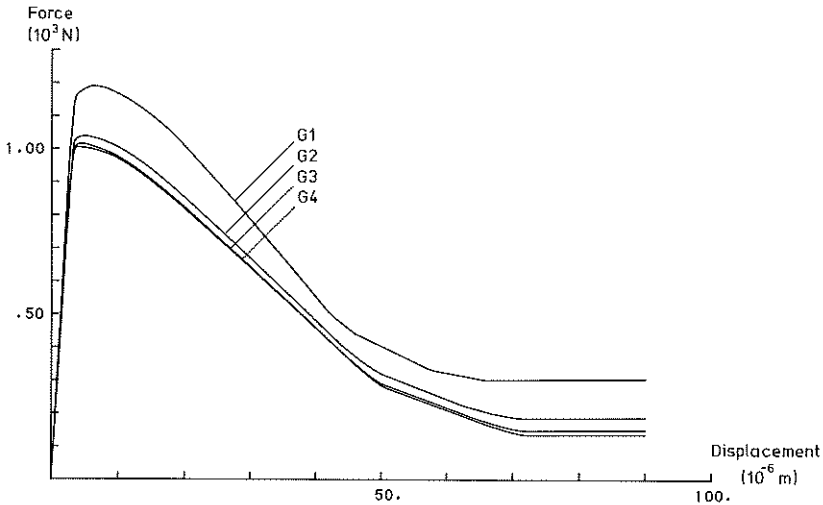
Fig. 5.19. Force-displacement curves for the computations according to Fig. 5.18.

	Estimate of G_F (N/m)	Deviation from input value
G1	143.4	10.3 %
G2	124.8	-4.0 %
G3	120.0	-7.7 %
G4	119.6	-8.0 %

Table 5.7. Estimated values of fracture energy for computations according to Fig. 5.18.

For the eight-node isoparametric element the meshes and the corresponding crack patterns are shown in Fig. 5.20.

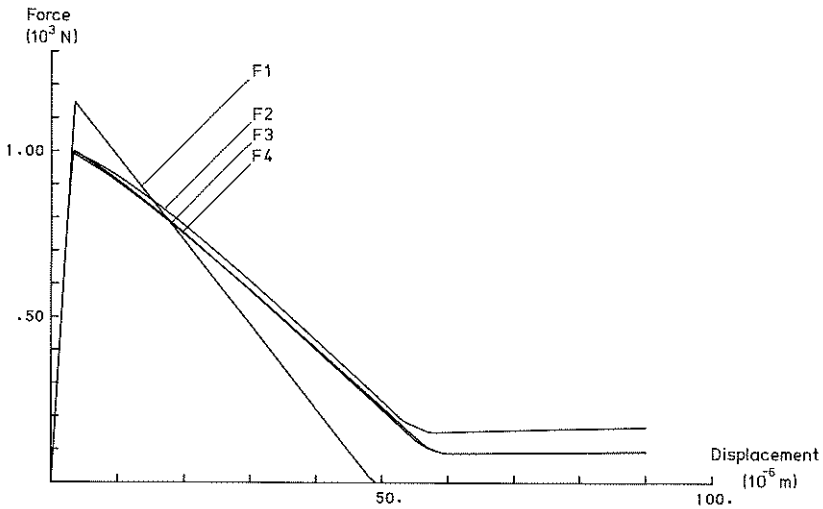The force-displacement curves for the computations corresponding to Fig. 5.20 are shown in Fig. 5.21 and the estimated fracture energies are given in Table 5.8. An important observation is that with the eight-node element the "tails" of the force-displacement curves are negligible.

Simulation of concrete tension specimen
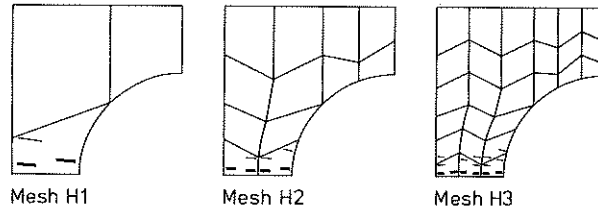
Fig. 5.20. Distorted finite element meshes and corresponding crack patterns for the eight-node isoparametric element.
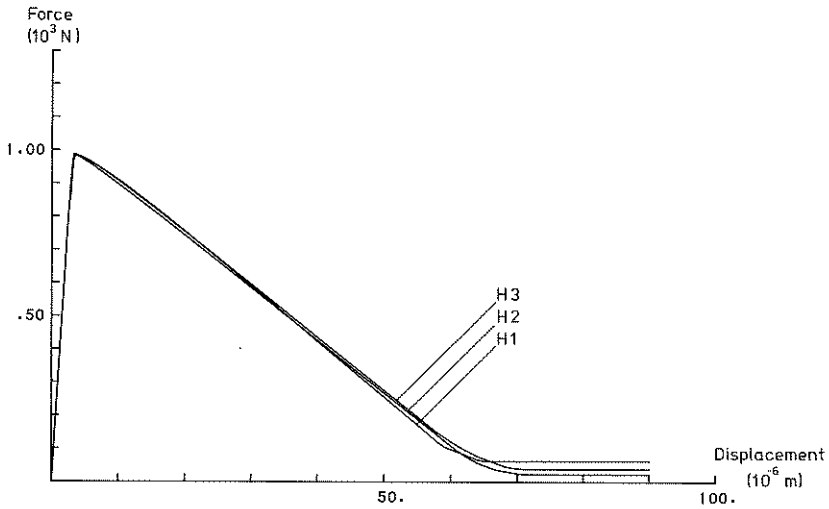
Fig. 5.21. Force-displacement curves for the computations according to Fig. 5.20.

The estimated values of fracture energy given in Tables 5.5-5.8 are plotted in Fig. 5.22 as a function of the inverted value of the number of equations n_{eq}^{-1}.

	Estimate of G_F (N/m)	Deviation from input value
H1	111.8	−14.0 %
H2	112.2	−13.7 %
H3	114.2	−12.2 %

Table 5.8. Estimated values of fracture energy for computations according to Fig. 5.20.
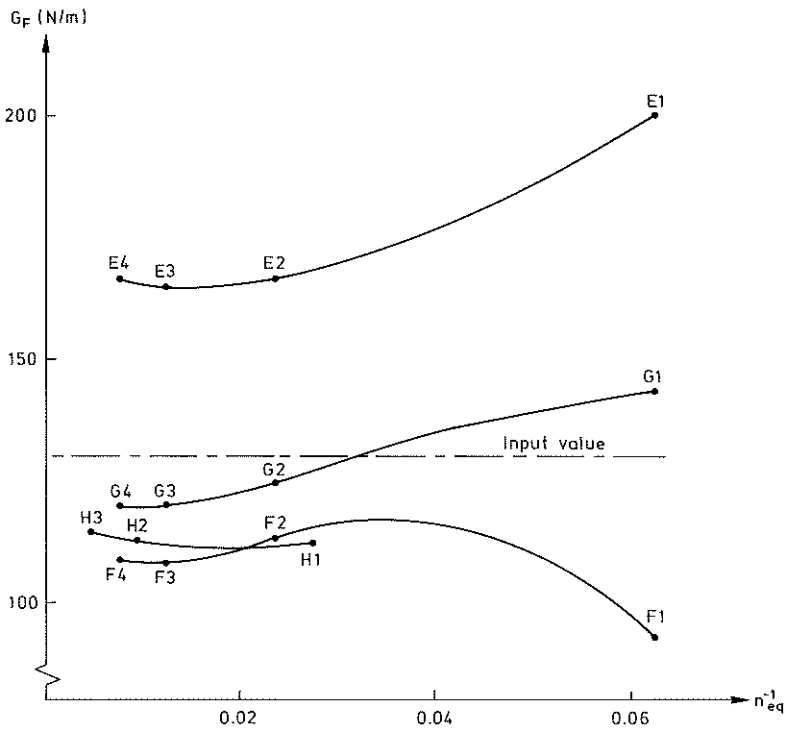
Fig. 5.22. Estimated values of fracture energy as a function of the number of equations.

5.4   Discussion

The proposed smeared approach has been used to simulate a
concrete tensile specimen, in order to show that the assumed
value of the fracture energy per unit area is reflected. For
regular meshes, good results are achieved for all the element
types applied. Compared with the results obtained by Oldenburg
[41] in the analysis of a tensile specimen a considerable
improvement has been achieved. A key to the improvement is the
definition of the equivalent length, which differs from what has
been used in previous smeared crack approaches, e.g. by Nilsson
and Oldenburg [40] or Bazant [4]. Another novelty of the present
approach is the way in which the shear stiffness is reduced
during crack development. The successive reduction of the shear
stiffness and the objectivity with respect to element subdivision
make the concept superior to the commonly used shear retention
factor.

For distorted meshes reasonable results are achieved for the
isoparametric elements, whereas the triangular element yields a
somewhat crude estimate of the fracture energy. However, this
element type has the lowest possible order of the interpolation
functions and because of this the meshes are unfavourable to
modelling the non-homogeneous strain distribution correctly. A
displacement increment applied when the stress perpendicular to
the crack planes of the distorted triangular elements has
decreased to zero, constrains the elements to an increment of
deformation including an increment of shear strain which is
proportional to the increment of normal strain. Due to the
assumed relation between shear displacement, shear stress and
normal displacement (Eq. 3.27) this deformation occurs at a
constant value of shear stress, which is the source of the
"tails" of remaining constant forces at the ends of the
computations. It may be noted that for distorted meshes the

remaining forces are considerably smaller for the eight-node element (Fig. 5.21) than for the other element types (Figs. 5.15, 5.17 and 5.19). This is a result of the influence of the degree of the interpolation functions. It may be concluded that elements of the lowest order are unfavourable in connection with smeared crack analysis, at least in situations where cracks do not develop parallel to element boundaries. In addition to the observed influence of the degree of the interpolation functions the predicted "tails" may be caused by other phenomena. Since the integration points are not positioned at the plane of symmetry the predicted crack direction may deviate from the direction of the symmetry plane. This, and also the fact that cracks are not allowed to develop non-orthogonally to existing crack planes, may contribute to the predicted "tails". However, the performed computations show that the smeared crack approach itself is able to reflect the input value of fracture energy. As an example of the influence of the "tails" it may be mentioned that the contribution to the dissipated energy as obtained with mesh H3 above is only about 8% of the total dissipated energy for a displacement twice as large as when the stress normal to the crack plane has decreased to zero. In a computation where for example compressive failure and reinforcement influence the dissipated energy, the contribution of the predicted "tails" is expected to be still smaller.

6. SIMULATION OF DRYING SPECIMENS

6.1   Introduction

In this chapter the theory described in the previous chapters is
applied to drying concrete specimens. On the basis of assumed
material properties the behaviour of drying specimens is
simulated. The purpose of the simulations is to clarify to what
extent the nonuniform stress distributions in drying specimens
influence the overall specimen behaviour.

Available experimental results from investigations of drying
specimens in general, relate to rectangular prisms or circular
cylinders. A detailed analysis of these types of specimens would
require three–dimensional modelling. However, due to the limited
computer capacity available at present only structures with plane
stress conditions are treated in this investigation. This and
other simplifications given below are acceptable since the
intention here is not to obtain results which quantitatively
reflect experimental data. The purpose is instead to simulate the
behaviour of specimens with constitutive properties which are
representative of concrete and to see how the specimen behaviour
is related to the material properties.

On the assumption that temperature is constant the moisture
transport is assumed to be governed by the diffusion relation

$$\frac{\partial}{\partial x_i} D_w \frac{\partial w}{\partial x_i} - \frac{\partial w}{\partial t} = 0 \qquad\qquad (6.1)$$

where D_w is the diffusivity and w is the moisture content.

Since the results are mainly of qualitative interest, drying may
be described in a simplified but reasonable way. Assuming that
the diffusivity D_w is constant we obtain the expression

$$D_w \frac{\partial^2 w}{\partial x_i \partial x_i} - \frac{\partial w}{\partial t} = 0 \tag{6.2}$$

In Eqs. (6.1) and (6.2) we further assume that the loss of evaporable water due to hydration can be neglected.

Assuming two-dimensional diffusion, i.e.

$$\frac{\partial^2 w}{\partial x_3 \partial x_3} = 0 \tag{6.3}$$

the solution to Eq. (6.2), for a rectangular region $-L_1 \leq x_1 \leq L_1$, $-L_2 \leq x_2 \leq L_2$ (see Fig. 6.2), of initial uniform moisture content w_0, subjected to an environment corresponding to moisture content w_1 at the surface, is according to Carslaw and Jaeger [13] given by

$$w(x_1, x_2, t) = w_1 + (w_0 - w_1)\psi(x_1, L_1, t)\psi(x_2, L_2, t) \tag{6.4}$$

where

$$\psi(x_i, L_i, t) = \sum_{n=0}^{\infty} \frac{2}{\mu_n}(-1)^n e^{-\mu_n^2 F_0} \cos\mu_n\xi \tag{6.5}$$

The parameters μ_n, F_0 and ξ in Eq. (6.5) are given by

$$\mu_n = \frac{(2n+1)\pi}{2} \tag{6.6}$$

$$F_0 = \frac{D_w t}{L_i^2} \tag{6.7}$$

$$\xi = \frac{x_i}{L_i} \tag{6.8}$$

It may be noted that the parameters F_0 and ξ are proportional to time t and coordinate x_i respectively.

Eq. (6.5) is illustrated in Fig. 6.1 for different values of F_0.
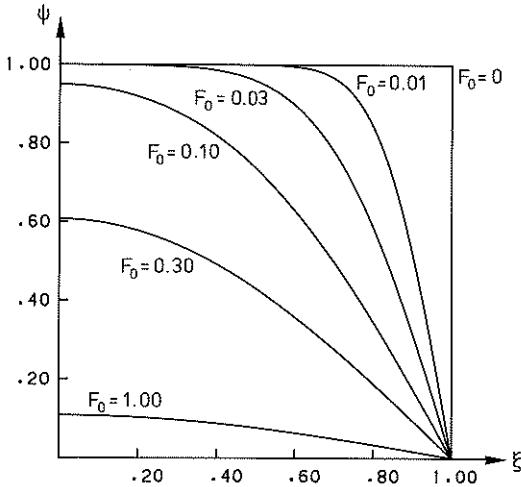
<u>Fig. 6.1</u>. Illustration of Eq. (6.5).

In the following computations, plane stress conditions are assumed. Furthermore it is assumed that the temperature T is constant and that the elastic modulus E and Poisson's ratio v are constant with respect to time. The creep behaviour is described by using two terms of the Dirichlet series. It is also assumed that the creep compliance parameters v_1 and v_2 and the moisture induced strain compliance parameter v_w are equal to Poisson's ratio v. The material is assumed to be characterized by the following parameters: elastic modulus $E = 3.5 \cdot 10^{10}$ Pa, Poisson's ratio $v = 0.2$, tensile strength $f_t = 3.5 \cdot 10^6$ Pa, fracture energy per unit area $G_F = 140.0$ N/m, slip modulus $G_s = 3.8 \cdot 10^6$ Pa, crack irreversibility parameter $\gamma_f = 0.2$, coefficient of drying

shrinkage $\alpha_w = 5.0 \cdot 10^{-6}$ m^3/kg, moisture induced strain compliance parameter $F_w = -4.0 \cdot 10^{-8}$ m^2/N, retardation times $\tau_1 = 5.0 \cdot 10^5$ s, $\tau_2 = 5.0 \cdot 10^6$ s, creep compliance parameters $F_1 = 1.0 \cdot 10^{-11}$ m^2/N, $F_2 = 1.5 \cdot 10^{-11}$ m^2/N and diffusivity $D_w = 3.0 \cdot 10^{-10}$ m^2/s, all representative of concrete. It should, however, be noted that the composition of the concrete has a very strong influence on the material parameters.

6.2   Simulation of nonloaded drying specimen

A concrete specimen as shown in Fig. 6.2, without external loading, is analysed during drying. The aim of the analysis in this section is to find to what extent the observed deformation of the specimen is affected by phenomena caused by the nonuniform stress state. As mentioned in the previous section plane stress conditions and two-dimensional diffusion are assumed. The initial moisture content is assumed to be $w_0 = 170$ kg/m^3. The environmental boundary conditions correspond to a fixed moisture content $w_1 = 70$ kg/m^3 at the surface. Due to symmetry only one quarter of the specimen is considered. The displacement boundary conditions are illustrated in Fig. 6.3.

Pure drying contraction related length change of specimen

When the contraction of a drying specimen is studied experimentally the change in length ΔL_α over some length L_α is measured. The observed change in length is interpreted as mean strain $\bar{\epsilon}_{\alpha\alpha}$, by the relation

$$\bar{\epsilon}_{\alpha\alpha} = \frac{\Delta L_\alpha}{L_\alpha} \tag{6.9}$$
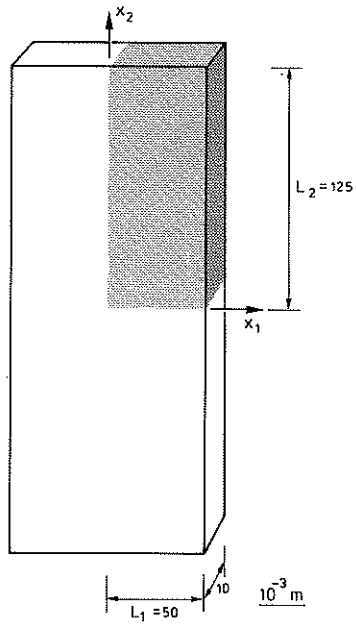
Fig. 6.2.   Analysed concrete specimen.
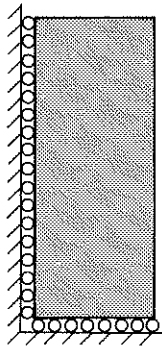
Fig. 6.3.   Boundary conditions.

Since the moisture distribution in a drying specimen is non-uniform it seems reasonable to relate the mean strain $\bar{\epsilon}_{\alpha\alpha}$ to the change in mean moisture content $\Delta\bar{w}$. By assuming that the relation obtained by using the described procedure is representative for a material point, one obtains a relation between moisture induced strain $\epsilon_{\alpha\alpha}^{w}$ and change in moisture content Δw.

In the present work the moisture induced strain is given by the expression (cf. Eq. (3.40))

$$\epsilon_{\alpha\alpha}^{w} = \alpha_w \Delta w \qquad (6.10)$$

where α_w is the coefficient of drying shrinkage and Δw is the difference between the moisture content $w(t)$ at time t and the initial moisture content w_0, i.e.

$$\Delta w = w(t) - w_0 \qquad (6.11)$$

According to the assumption above the relation given in Eq. (6.10) can be applied to the mean strain $\bar{\epsilon}_{\alpha\alpha}$ and the change in mean moisture content $\Delta\bar{w}$, i.e.

$$\bar{\epsilon}_{\alpha\alpha} = \alpha_w \Delta\bar{w} \qquad (6.12)$$

where $\Delta\bar{w}$ is given by

$$\Delta\bar{w} = \bar{w}(t) - w_0 \qquad (6.13)$$

in which, for two-dimensional diffusion, the mean moisture content $\bar{w}(t)$ for a rectangular region is given by

$$\bar{w}(t) = \frac{1}{L_1 L_2} \int_0^{L_2} \int_0^{L_1} w(x_1, x_2, t) dx_1 dx_2 \tag{6.14}$$

where $w(x_1, x_2, t)$ is the moisture content which in the present study is assumed to be given by Eq. (6.4).

Substitution of Eq. (6.12) into Eq. (6.9) yields the expression

$$\Delta L_\alpha = L_\alpha \alpha_w \Delta \bar{w} \tag{6.15}$$

Adopting a value of the coefficient α_w, Eq. (6.15) can be used to obtain the response ΔL_α which could occur if the overall length change were representative for a material point. This response will in the following be referred to as pure drying contraction related length change and will be compared with the response obtained when the nonuniform moisture distribution and nonlinear effects are considered. For the geometry of Fig. 6.2 and the value of α_w given in the previous section the change in the mean value of the moisture content $\Delta \bar{w}$ and the pure drying contraction related length change ΔL_2 at different time values t are given in Table 6.1.

t $(10^6$ s)	$\Delta \bar{w}$ (kg/m^3)	ΔL $(10^{-6}$ m)
0.03	−9.29	−5.81
0.10	−16.69	−10.43
0.30	−28.14	−17.59
1.00	−48.61	−30.38
3.00	−75.68	−47.30
10.00	−97.88	−61.17

Table 6.1. Change in mean value of moisture content and corresponding pure drying contraction related length change.

Simulated response of specimen

The specimen is now analysed using a four-node isoparametric element with four integration points. Four different meshes, all with square elements, are used: mesh A with 4 by 10 elements, mesh B with 6 by 15 elements, mesh C with 8 by 20 elements and mesh D with 12 by 30 elements, cf. Fig. 6.4. Three sets of computations with different assumptions regarding the material modelling are performed.

In the first set of computations the total strain is assumed to consist of elastic strain and conventional moisture induced strain, i.e. fracturing strain, creep strain and stress dependence of moisture induced strain are not considered. The mean values of the vertical displacements of the upper edge at different times are shown in Table 6.2. As can be seen the displacements for large values of time converge for mesh refinement. The mesh dependence for small time values is due to the better ability of fine meshes to reflect the strongly non-uniform state, cf. Fig. 6.1. A comparison with Table 6.1 shows that the results for the assumption of an elastic material in Table 6.2, at least for fine meshes, reproduce the results in Table 6.1, which represent the pure drying contraction related length change. The differences originate from the numerical approximation in the computation of the moisture distribution in the finite element computation.

In the second set of computations the total strain is assumed to consist of elastic strain, fracture strain, conventional moisture induced strain and creep strain, i.e. stress dependence of moisture induced strain is not considered. Compared with the previous computations, fracture and creep strain are now introduced. The mean values of the vertical displacements of the upper edge at different times are shown in Table 6.3. As can be seen, the results again show convergence with respect to a mesh

Time	Displacement $(10^{-6}$ m)			
$(10^6$ s)	Mesh A	Mesh B	Mesh C	Mesh D
0.03	-3.05	-4.73	-5.25	-5.57
0.10	-9.22	-9.93	-10.16	-10.31
0.30	-16.97	-17.32	-17.44	-17.52
1.00	-30.09	-30.25	-30.31	-30.35
3.00	-47.18	-47.25	-47.27	-47.29
10.00	-61.16	-61.17	-61.17	-61.17

Table 6.2. Response of specimen regarding elastic strain and conventional moisture induced strain.

refinement. Owing to tensile fracture, the magnitudes of the displacements are a little less than for the computations shown in Table 6.1. The differences are greatest at early stages of drying. After a long time the differences decrease owing to closing of cracks.

Time	Displacement $(10^{-6}$ m)			
$(10^6$ s)	Mesh A	Mesh B	Mesh C	Mesh D
0.03	-3.05	-4.00	-3.68	-3.72
0.10	-7.45	-7.08	-7.36	-7.33
0.30	-13.46	-13.99	-13.76	-13.82
1.00	-27.10	-27.40	-27.29	-27.33
3.00	-45.60	-45.74	-45.68	-45.68
10.00	-60.45	-60.43	-60.38	-60.36

Table 6.3. Response of specimen regarding elastic strain, fracture strain, conventional moisture induced strain and creep strain.

The crack patterns at the end of the computations are shown in Fig. 6.4. The fracture development is confined to the region close to the surface where tensile stresses occur.
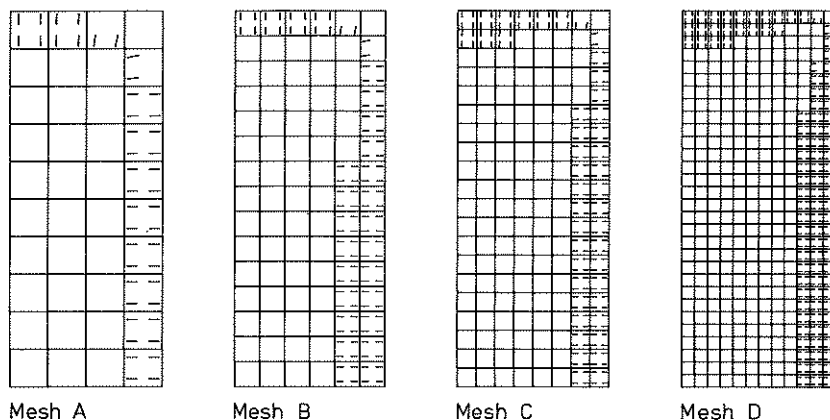
Fig. 6.4. Crack patterns for computations regarding elastic strain, fracture strain, conventional moisture induced strain and creep strain.

In the four computations roughly the same region is affected by cracking. As can be seen, fracture has developed in several elements bounding each other on the edges parallel to the crack direction, i.e. several crack planes are predicted to develop very close to each other. In this situation the width of each crack and the corresponding stress reduction is small. In reality, the predicted width of a developing crack corresponds to the total elongation of a micro-cracked zone. If several crack planes are predicted to develop very close to each other the corresponding zones of micro-cracks will join together and form one region with a uniform distribution of micro-cracks. Therefore, the predicted type of crack pattern will in the following be referred to as distributed fracture. This type of crack pattern is in contrast to the crack patterns obtained in Chapter 5, where fracture development occurred in several elements forming a band parallel to the crack direction. This latter situation will in the following be referred to as localized fracture. Since distributed fracture has been predicted

in the above computations, the question arises whether the results are objective with respect to mesh. As can be seen in Table 6.3 the displacements are practically unaffected by the mesh. In order to further examine about the objectivity of the results the total energy dissipated by fracturing in the structure is computed. This energy, G_T, is defined by the integral

$$G_T = \int_V \int_0^t \sigma_{ij} \dot{\varepsilon}_{ij}^f dt \ dV \qquad (6.16)$$

The dissipated energies after $10.0 \cdot 10^6$ s, corresponding to the four computations, are shown in Fig. 6.5 as a function of the inverted value of the number of equations n_{eq}^{-1}. The computed values of the dissipated energy indicate convergence for mesh refinement, i.e. the results are objective with respect to mesh, not only with respect to displacements, but also with respect to dissipated energy.
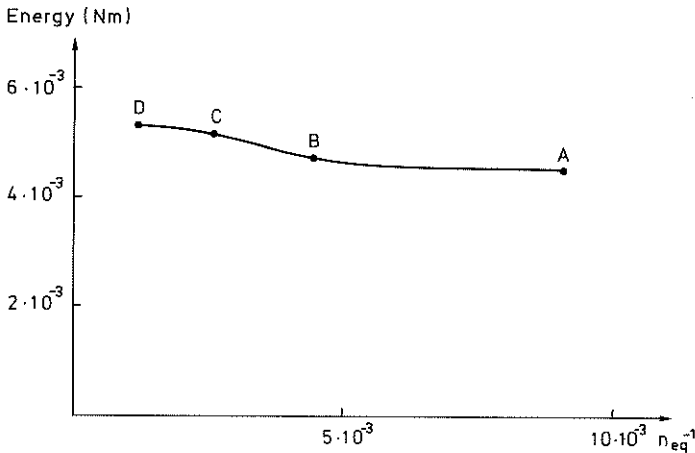

<u>Fig. 6.5</u>. Values of dissipated energy corresponding to Fig. 6.4, as a function of the number of equations n_{eq}.

The third set of computations was performed under the same assumptions as the second one, except that the moisture induced strain was assumed to be stress dependent. The purpose of these computations is to investigate the influence of this stress dependence on a specimen without external loading. The mean values of the vertical displacements of the upper edge at different times are shown in Table 6.4. The results are practically equal to the results in Table 6.3. This important observation demonstrates that the stress dependence of moisture induced strain does not exert a significant influence on the displacements under the present assumptions.

Time	Displacement $(10^{-6}$ m)			
$(10^6$ s)	Mesh A	Mesh B	Mesh C	Mesh D
0.03	−2.98	−4.00	−3.71	−3.73
0.10	−7.50	−7.15	−7.36	−7.38
0.30	−13.61	−13.94	−13.86	−13.91
1.00	−27.19	−27.46	−27.34	−27.36
3.00	−45.71	−45.80	−45.73	−45.73
10.00	−60.02	−59.99	−59.92	−59.90

Table 6.4. Response of specimen regarding elastic strain, fracture strain, stress dependent moisture induced strain and creep strain.

The crack patterns at the end of the computations are shown in Fig. 6.5.

The regions affected by cracking are slightly smaller than those in Fig. 6.4. The difference is due to the stress dependence of the moisture induced strain which affects the stress distribution and leads to a decrease of the fracture strain compared with the previous computations. This is demonstrated by Fig. 6.7, where

Mesh A   Mesh B   Mesh C   Mesh D
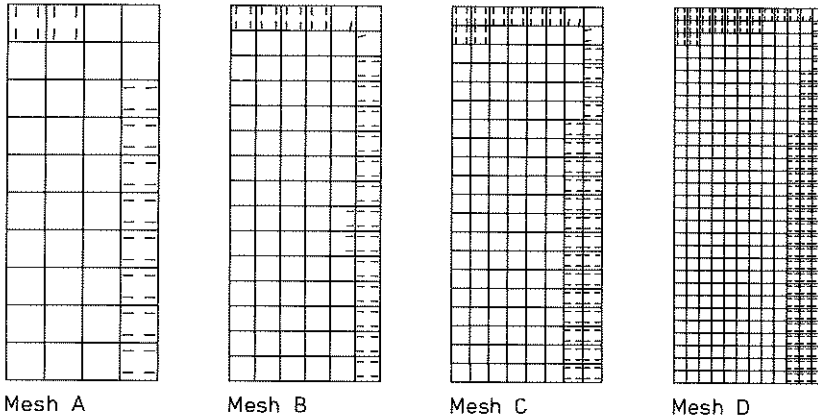
Fig. 6.6. Crack patterns for computations regarding elastic strain, fracture strain, stress dependent moisture induced strain and creep strain.

the dissipated energies after $10.0 \cdot 10^6$ s corresponding to Fig. 6.6 are shown. Again we conclude that objectivity with respect to mesh refinement is achieved both for displacements (cf. Table 6.4) and total dissipated energy (cf. Fig. 6.7).

The responses obtained in three computations are shown in Fig. 6.8. Curve I shows the response corresponding to Table 6.1 obtained by use of Eq. (6.15), representing the pure drying contraction related length change. Curves II and III show the responses obtained with mesh D due to theoretical simulations of the specimen with different assumptions regarding the material properties. With the present assumptions the difference between curve I and curves II and III is as much as 20-30% at early stages of drying. The difference is due to the influence of the nonuniform stress state caused by drying and appears to be quite significant. After a long time the difference is, however, much
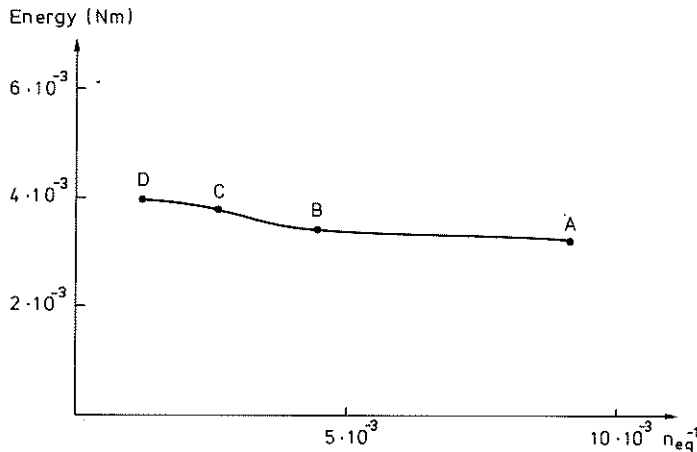
Fig. 6.7.   Values of dissipated energy corresponding to Fig. 6.6, as a function of the number of equations n_{eq}.

smaller, 1–2% with the present assumptions. From the computations it can be concluded that the deformation observed after a long time reflects without much deviation the material contraction due to drying. Curves II and III follow each other for early stages of drying and differ only slightly after a long time, which demonstrates that the assumption of stress dependence of moisture induced strain does not have a significant influence on the overall deformation of the nonloaded specimen. The stress distributions corresponding to Tables 6.3 and 6.4, just above the horizontal symmetry line at different times as computed with mesh D, are shown in Fig. 6.9. As can be seen, the stress distribution at early stages of drying is not affected by the assumption of stress dependence of moisture induced strain (curve III), compared with conventional moisture induced strain description (curve II). At later stages, however, the assumption of stress dependence leads to a redistribution of stress with a decrease of the tensile stresses near the surface and a decrease of the compressive stresses in the core of the specimen. After a long time, when the specimen is in moisture equilibrium, residual

Displacement
$(10^{-5}m)$
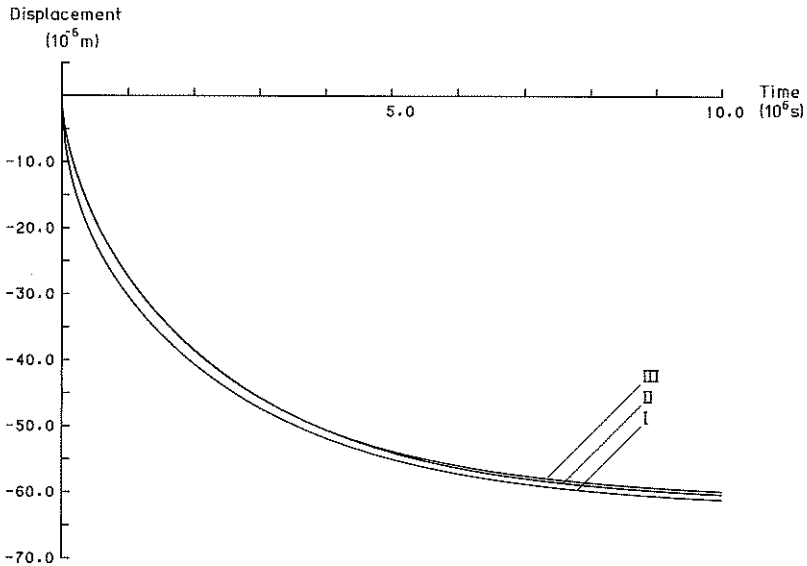
Fig. 6.8. Responses obtained with mesh D in computations corresponding to Table 6.3 (curve II) and Table 6.4 (curve III) compared with the pure drying contraction related length change corresponding to Table 6.1 (curve I).

compressive stresses have developed near the surface. These stresses are higher when the moisture induced strain is assumed to be stress dependent than otherwise. The influence of the assumption of stress dependence of moisture induced strain will in the next section be investigated for a specimen with an external compressive load.
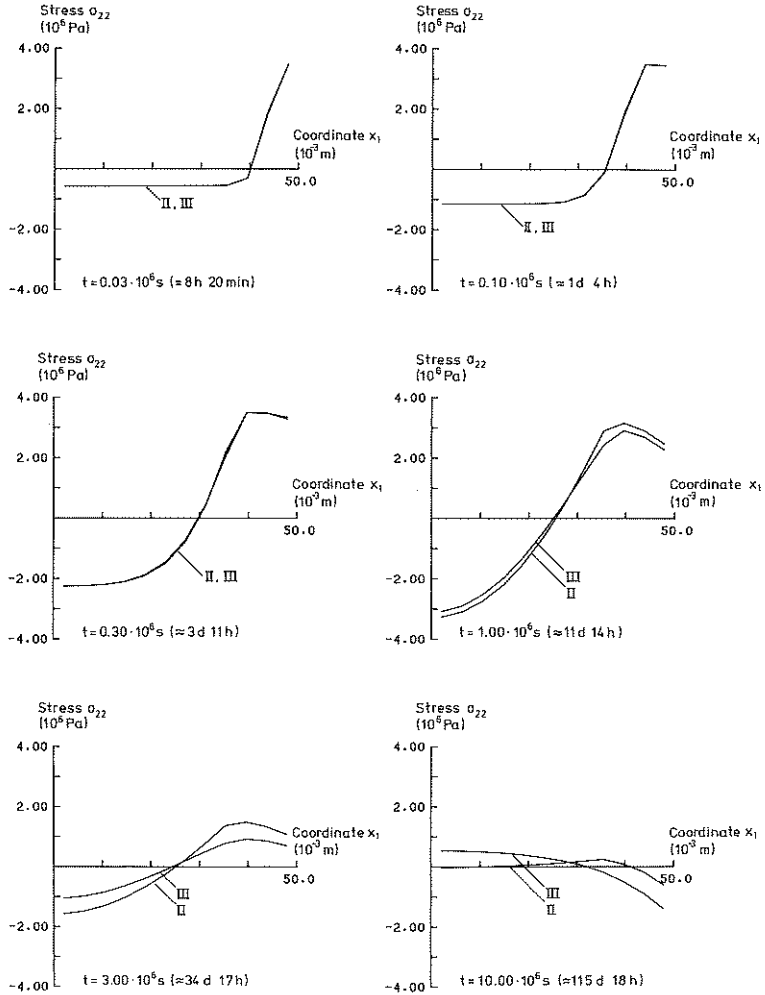
Fig. 6.9. Distributions of normal stress σ_{22} just above the horizontal symmetry line, as obtained with mesh D. Curve II is obtained with the conventional moisture induced strain description and curve III with stress dependent moisture induced strain taken into consideration.

6.3. Simulation of loaded drying specimen

The concrete specimen which was analysed in Sec. 6.2 is in this section analysed with the assumption of an external compressive load according to Fig. 6.10. The load is applied as a uniform stress $\sigma_{22} = -7.9 \cdot 10^6$ Pa at the upper edge of the specimen. Just as in Sec. 6.2, only one quarter of the specimen is analysed owing to symmetry. The same environmental conditions are assumed and the same finite element meshes are used.
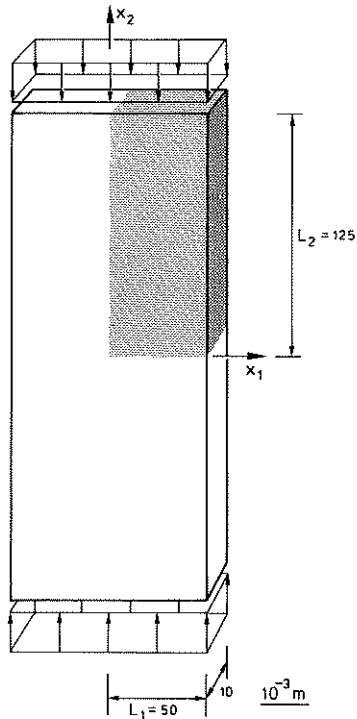
Fig. 6.10. Analysed concrete specimen.

The aim of this analysis is to find out to what extent the Pickett effect is a material property, and to what extent it is caused by the non-uniform stress state.

Two sets of computations with different assumptions regarding the material modelling are performed. The responses obtained in these computations are compared with the sum of the response of a non-loaded drying specimen according to Sec. 6.2 and the response of a loaded specimen in constant environmental conditions, which will be treated before the results for a loaded drying specimen will be given.

Elastic deformation, creep and shrinkage

Since the stress and strain distributions are uniform in a uniformly loaded specimen in moisture equilibrium, numerical simulations give the same response for all the four meshes considered. The change in length at different values of time, as obtained by numerical simulation, is shown in Table 6.5 where the deviation from an analytical solution is also given. As can be seen the numerical simulation gives results which are in good agreement with the analytical solution consisting of elastic and creep contributions and given by

$$\Delta L = [\frac{1}{E} + F_1(1 - e^{-\frac{t}{\tau_1}}) + F_2(1 - e^{-\frac{t}{\tau_2}})]\sigma_{22} L_2 \qquad (6.15)$$

Time (10^6 s)	Displacement (10^{-6} m)	Deviation from analytical solution
0.03	-28.86	-0.1 %
0.10	-30.28	-0.1 %
0.30	-33.55	+0.1 %
1.00	-39.62	+0.4 %
3.00	-45.10	+0.8 %
10.00	-51.48	+1.1 %

Table 6.5. Response of loaded specimen in constant environmental conditions (elastic deformation and creep).

The sum of the response of a nonloaded drying specimen according to Table 6.3 and the response of a loaded specimen in constant environmental conditions according to Table 6.5 is shown in Table 6.6.

Time (10^6 s)	Displacement (10^{-6} m)			
	Mesh A	Mesh B	Mesh C	Mesh D
0.03	-31.90	-32.86	-32.53	-32.58
0.10	-37.74	-37.37	-37.64	-37.62
0.30	-47.01	-47.54	-47.32	-47.37
1.00	-66.71	-67.01	-66.91	-66.95
3.00	-90.70	-90.85	-90.78	-90.79
10.00	-111.93	-111.91	-111.87	-111.85

Table 6.6. Sum of response of nonloaded drying specimen and loaded specimen in constant environmental conditions (elastic deformation, creep and shrinkage).

Simulated response of specimen

Let us now simulate the behaviour of a drying specimen with an
external compressive load. In the first set of computations the
total strain is assumed to consist of elastic strain, fracture
strain, creep strain and conventional moisture induced strain,
i.e. stress dependence of moisture induced strain is not
considered. The mean values of the vertical displacements of the
upper edge at different times are shown in Table 6.7. Again we
observe objectivity with respect to mesh refinement when
displacements are considered. In relation to the Pickett effect
the results shown in Table 6.7 should be compared with the
response given in Table 6.6. The difference between the results
is the effect of the nonuniform stress distribution in a drying
specimen. As can be seen, this difference is very small and can
not explain the Pickett effect.

Time (10^6 s)	Displacement (10^{-6} m)			
	Mesh A	Mesh B	Mesh C	Mesh D
0.03	–31.90	–34.58	–34.11	–34.43
0.10	–39.51	–40.21	–40.44	–40.59
0.30	–50.52	–50.87	–50.99	–51.07
1.00	–69.71	–69.87	–69.92	–69.97
3.00	–92.29	–92.36	–92.38	–92.39
10.00	–112.65	–112.65	–112.65	–112.65

Table 6.7. Response of specimen regarding elastic strain,
fracture strain, conventional moisture induced strain
and creep strain.

The crack patterns at the ends of the computations are shown in
Fig. 6.11. Owing to the compressive external load no horizontal

crack planes have appeared, i.e. the crack pattern is
significantly different from what was obtained for the nonloaded
specimen in the previous section, cf. Fig. 6.4.

Mesh A   Mesh B   Mesh C   Mesh D

Fig. 6.11. Crack patterns for computations regarding elastic
strain, fracture strain, conventional moisture induced
strain and creep strain.

The results so far indicate clearly that the Pickett effect is to
a major extent a material property, which means that it should be
included in the constitutive model. Thus in the second set of
computations the total strain is assumed to consist of elastic
strain, fracture strain, creep strain and stress dependent
moisture induced strain. The mean values of the vertical
displacements of the upper edge at different times are shown in
Table 6.8. The magnitudes of the deformation are considerably
greater than for the computations shown in Table 6.6 which
demonstrates the ability of the applied constitutive model to
describe the Pickett effect.

Time	Displacement (10^{-6} m)			
(10^6 s)	Mesh A	Mesh B	Mesh C	Mesh D
0.03	−32.78	−34.76	−35.29	−35.58
0.10	−41.77	−42.45	−42.67	−42.82
0.30	−54.67	−55.01	−55.14	−55.21
1.00	−77.93	−78.08	−78.13	−78.16
3.00	−106.33	−106.35	−106.36	−106.35
10.00	−131.10	−131.03	−131.00	−130.98

Table 6.8. Response of specimen regarding elastic strain, fracturing strain, stress dependent moisture induced strain and creep.

The crack patterns at the ends of the computations are shown in Fig. 6.12. The region affected by cracking in mesh D is slightly smaller than the one in Fig. 6.11.

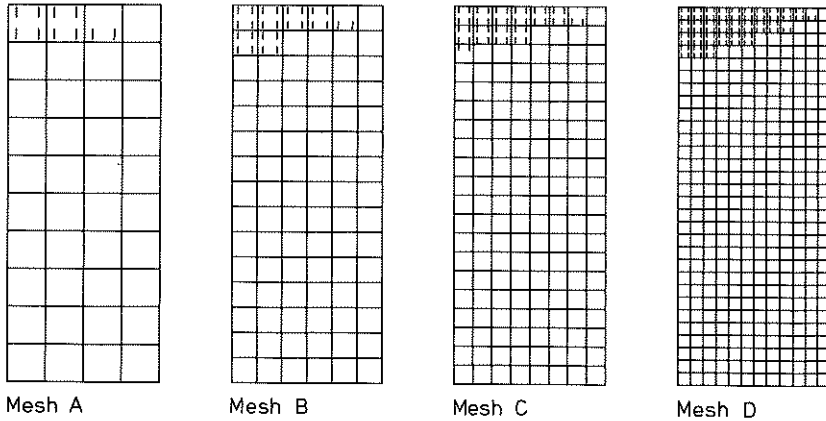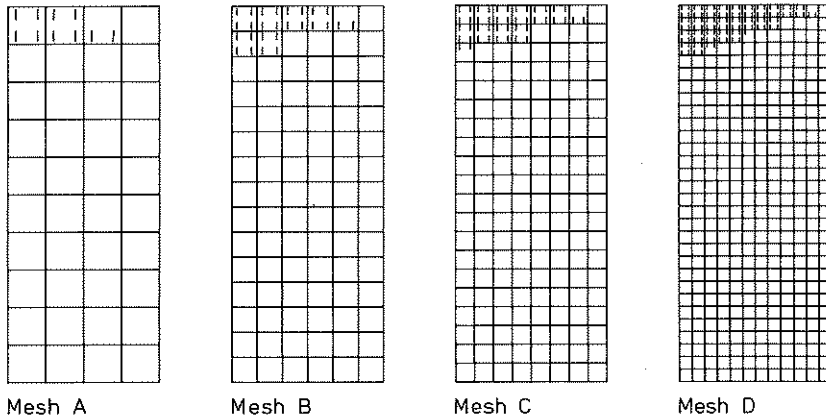Mesh A   Mesh B   Mesh C   Mesh D

Fig. 6.12. Crack patterns for computations regarding elastic strain, fracture strain, stress dependent moisture induced strain and creep strain.

The responses obtained with mesh D in the computations corresponding to Tables 6.6, 6.7 and 6.8 are shown in Fig. 6.13. Curve I shows the sum of the responses of a nonloaded drying specimen and a loaded nondrying specimen. Curve II shows the response of a loaded drying specimen, as obtained with the assumption of the conventional moisture induced strain description. At early stages of drying the response according to curve II is about 6-8% greater than the response according to curve I. After a long time the difference is reduced to 1-2%. According to experimental results by Gamble and Parrott [26] the corresponding difference, for the same load as in the present analysis, is about 15-20% at both early and late stages (cf. Fig. 2.6), i.e. the simulation according to curve II does not satisfactorily reflect the experimental behaviour. Curve III shows the response of a loaded drying specimen, as obtained with the assumption of stress dependence of moisture induced strain. Both at early and late stages the response according to curve III is about 15-20% greater than the response according to curve I which is in accordance with the experimental results of Fig. 2.6. It should, however, be noted that the theoretical simulation cannot be directly compared with the experimental results, since the simulation considers plane stress conditions and the stress state in the experiment is three-dimensional. It should also be noted that the influence of aging and moisture content on material properties, which may affect experimental results, is not considered in the theoretical analysis. The simulation does, however, qualitatively reflect the experimental behaviour.

According to Eq. (3.81) the increase in the rate of drying contraction due to the assumed stress dependence, is proportional to the rate of drying and to the stress. In this particular case the stress dependence of moisture induced strain changes the stress distribution only to a small extent compared with the

Displacement
(10^{-6} m)
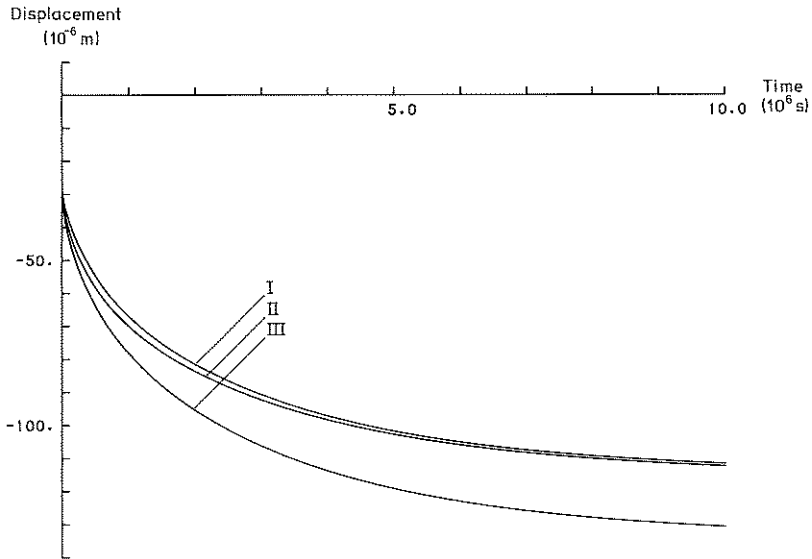
Fig. 6.13. Responses obtained with mesh D in computations corresponding to Table 6.6 (curve I), Table 6.7 (curve II) and Table 6.8 (curve III).

conventional description. This is illustrated in Fig. 6.14 where the stress distribution just above the horizontal symmetry line is shown at different values of time, as obtained with mesh D. Curve II shows the stress distribution for conventional moisture induced strain description and curve III shows the stress distribution when stress dependence of moisture induced strain is taken into consideration.

From the computations it can be concluded that the Pickett effect is to a major extent due to the stress dependence of moisture induced strain and can only to a small extent be explained by prevention of fracture development in a specimen loaded in compression.
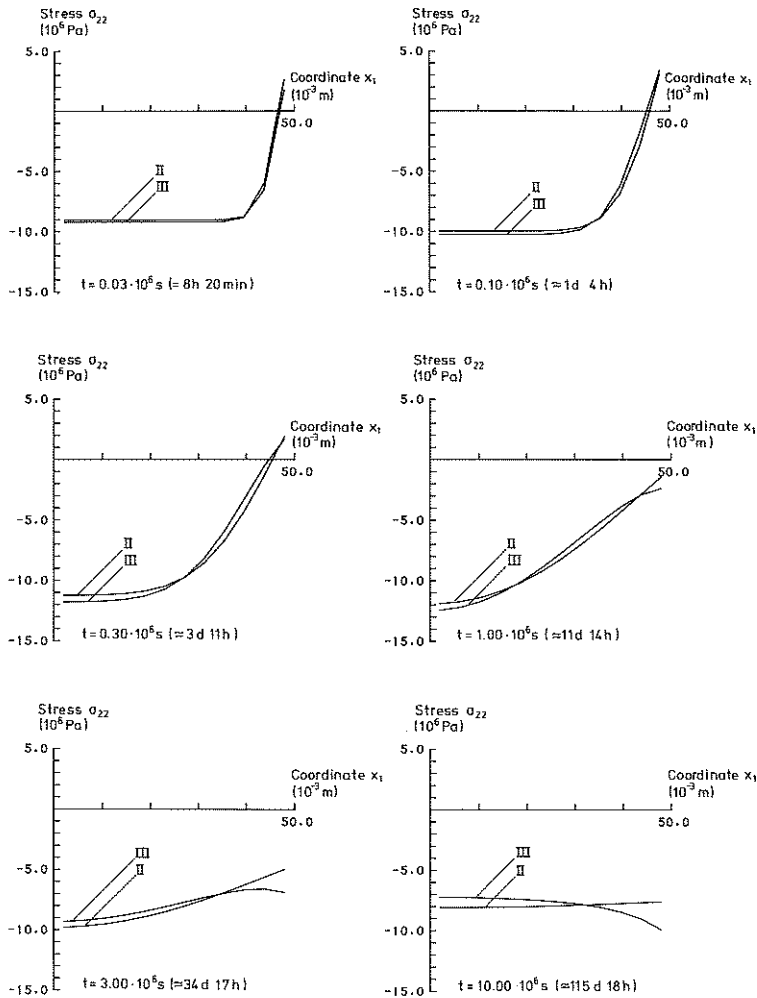
Fig. 6.14. Distributions of normal stress σ_{22} just above the horizontal symmetry line, as obtained with mesh D. Curve II is obtained with the conventional moisture induced strain description and curve III with stress dependent moisture induced strain taken into consideration.

6.4 Investigation of the influence of stress gradient on the crack pattern

The computations in Secs. 6.2 and 6.3 concern specimens which have strong stress gradients due to drying. Since the computations, in contrast to the computations in Chapter 5, give distributed fracture one may question whether the model is able to predict localized fracture under environmental loading. In order to gain an understanding of this important question a structure is analysed under different assumptions regarding the moisture conditions.

A structure as shown in Fig. 6.15 is analysed during drying. Displacement of the upper and lower boundaries in the vertical direction is prevented and the left-hand boundary cannot move in the horizontal direction. The structure is drying unidimen-sionally from the right-hand surface. In order to slow down drying, the right-hand surface is insulated.
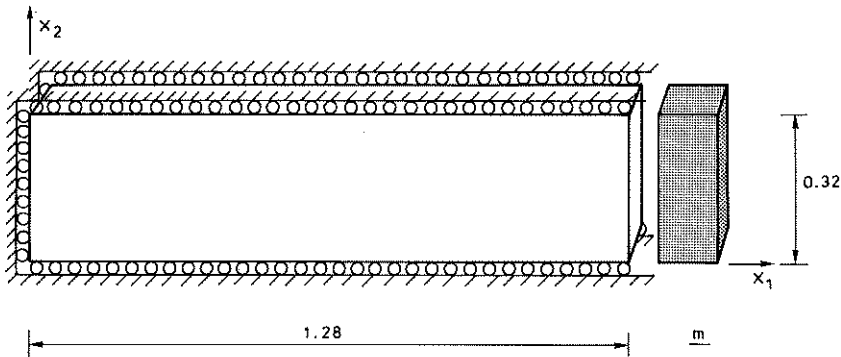

Fig. 6.15. Analysed concrete structure.

For unidimensional diffusion, i.e.

$$\frac{\partial^2 w}{\partial x_2 \partial x_2} = 0, \qquad \frac{\partial^2 w}{\partial x_3 \partial x_3} = 0 \qquad\qquad (6.16)$$

the solution to Eq. (6.2), for a region $-L_1 \leq x_1 \leq L_1$ with initial uniform moisture content w_0, subjected to an environment corresponding to moisture content w_1 at the boundaries, is according to Carslaw and Jaeger [13], given by

$$w(x_1, t) = w_1 + (w_0 - w_1)\psi(x_1, L_1, t) \qquad\qquad (6.17)$$

where $\psi(x_1, L_1, t)$ is given by Eq. (6.5).

In the present analysis four-node isoparametric elements are used. The mesh consists of 32 by 8 square elements. Before cracks start to develop, the distribution of the stresses is the same in all horizontal cross sections. In order to prevent commencement of crack development in several elements simultaneously the geometry is given a very small imperfection giving the element just above the centre line at the right-hand surface a small reduction of area. Since in the present computation we are interested in the qualitative behaviour of the structure for different stress gradients, in particular the question of localized and distributed fracture, the strain is assumed to consist only of elastic strain, fracture strain and conventional moisture induced strain, i.e. creep strain and stress dependence of the moisture induced strain are not considered. The initial moisture content in the structure is assumed to be $w_0 = 170$ kg/m^3. The environment outside the insulation is assumed to correspond to a moisture content $w_1 = 70$ kg/m^3.

In order to understand the behaviour of the specimen under different stress gradients, one computation without insulation and two computations with different insulation thicknesses, are

performed. The insulation is chosen in such a way that the sum of the length of concrete equivalent to the insulation and the length of the structure itself is 10 and 100 times the structure length respectively, i.e. insulation thickness of 11.52 m and 126.72 m, respectively. In this way only the regions $0 < \xi < 0.1$ and $0 < \xi < 0.01$ of Fig. 6.5 are considered, giving small stress gradients. The crack patterns at different values of time are shown in Figs. 6.16, 6.18 and 6.20 for the three computations. The corresponding stress distributions just above the lower boundary and just above the horizontal centre line are shown in Figs. 6.17, 6.19 and 6.21.

In the structure without insulation the stress gradients are large. In this computation the fracture is not localized to a single plane at the early stages of the computation. Distributed fracturing develops in three element rows before a localization is initiated. In the computation with insulation corresponding to 11.52 m concrete the fracture localizes after distributed fracturing in two element rows. The fracture is localized throughout the analysis when insulation corresponding 126.72 m concrete is assumed. In this computation the stress gradients are very small.
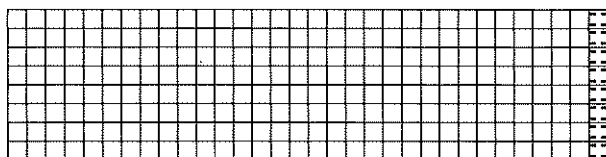
t = 0.408·10⁶s
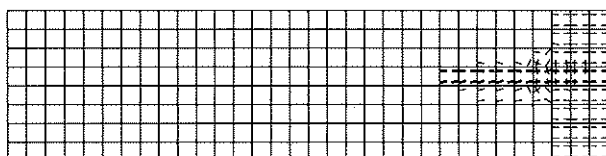
t = 100.0·10⁶s
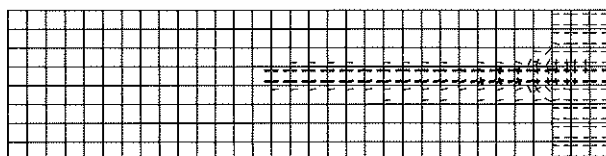
t = 500.0·10⁶s
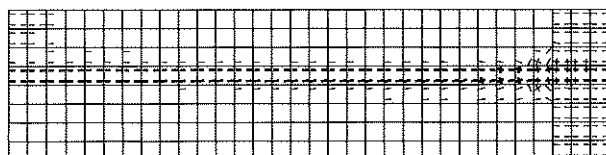
t = 1100.0·10⁶s

Fig. 6.16. Crack pattern for structure without insulation.

Stress σ₂₂
(10⁶ Pa)
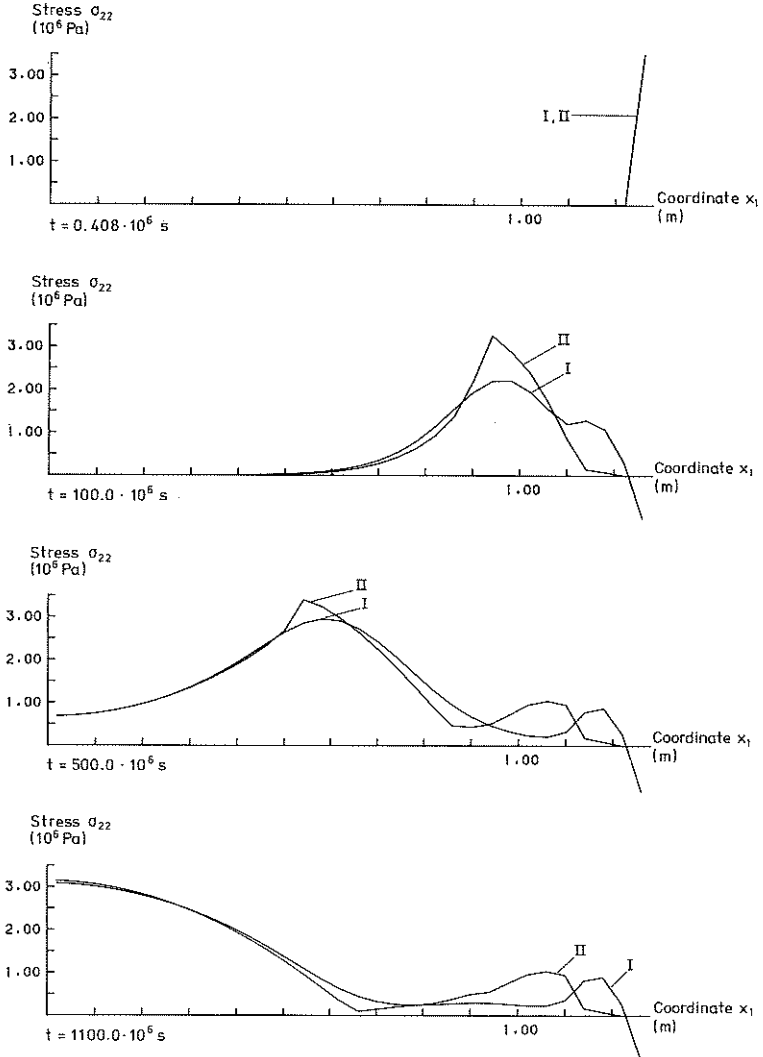
Fig. 6.17. Stress distributions in structure without insulation.
Curve I shows the stress just above the lower boundary
and curve II just above the horizontal centre line.
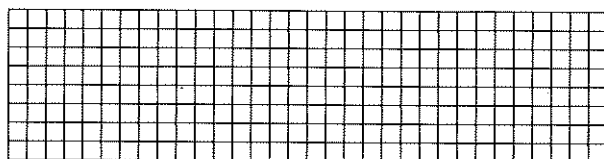
t = 98.26·10⁹s
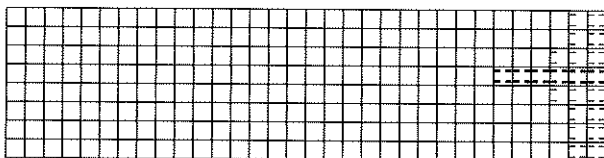
t = 99.0·10⁹s
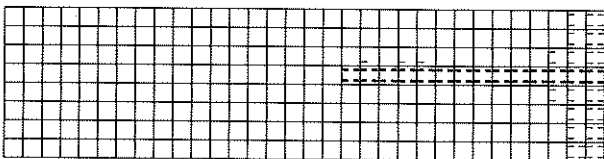
t = 100.0·10⁹s
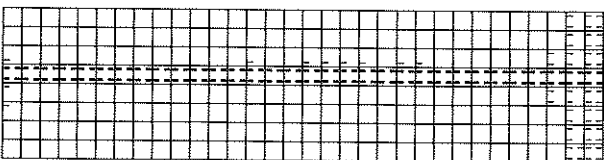
t = 101.0·10⁹s

<u>Fig. 6.18.</u> Crack pattern for structure with insulation corresponding to 11.52 m concrete.
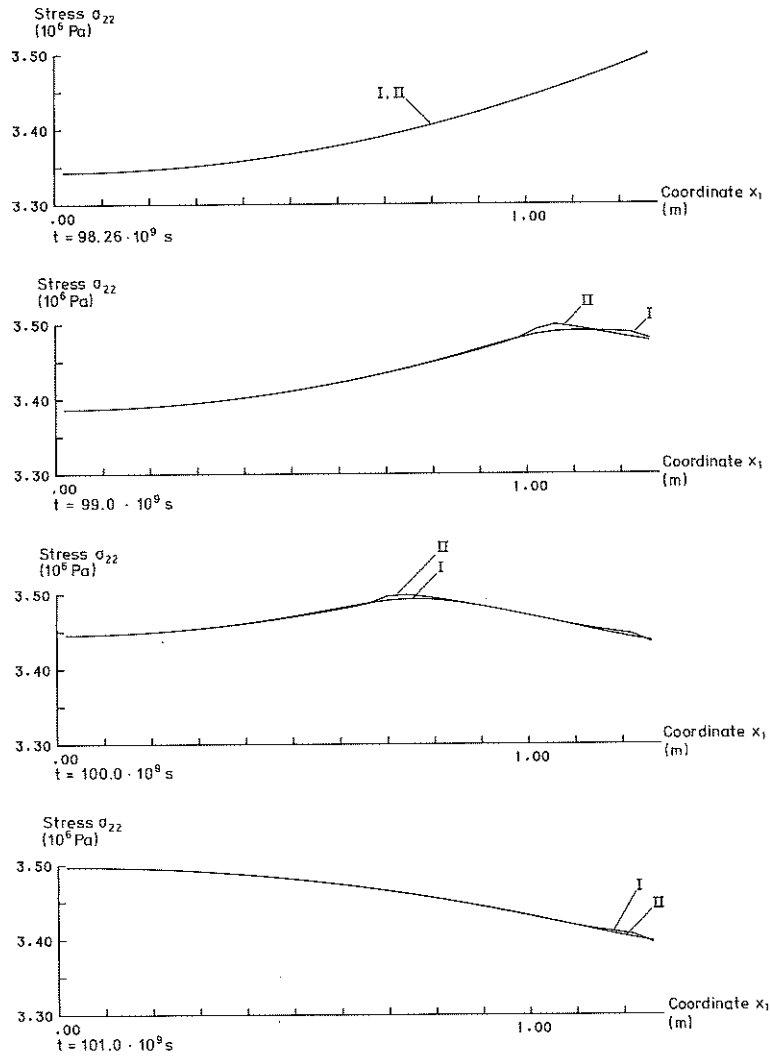
Fig. 6.19. Stress distributions in specimen with insulation corresponding to 11.52 m concrete. Curve I shows the stress just above the lower boundary and curve II just above the horizontal centre line.
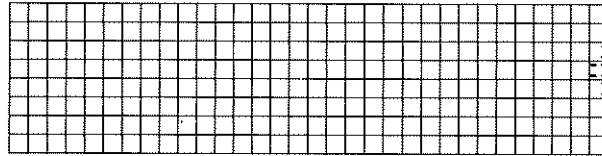
$t = 10.090 \cdot 10^{12}\,s$
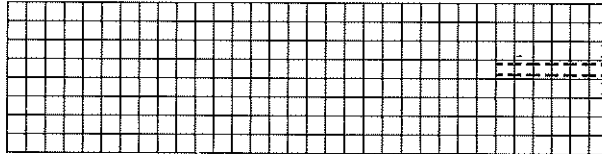
$t = 10.091 \cdot 10^{12}\,s$
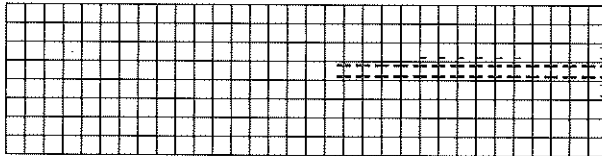
$t = 10.092 \cdot 10^{12}\,s$
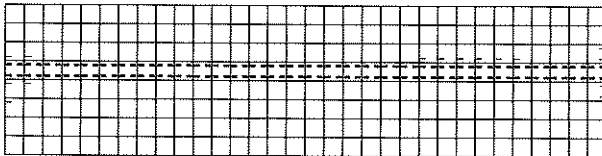
$t = 10.093 \cdot 10^{12}\,s$

Fig. 6.20. Crack pattern for structure with insulation corresponding to 126.72 m concrete.
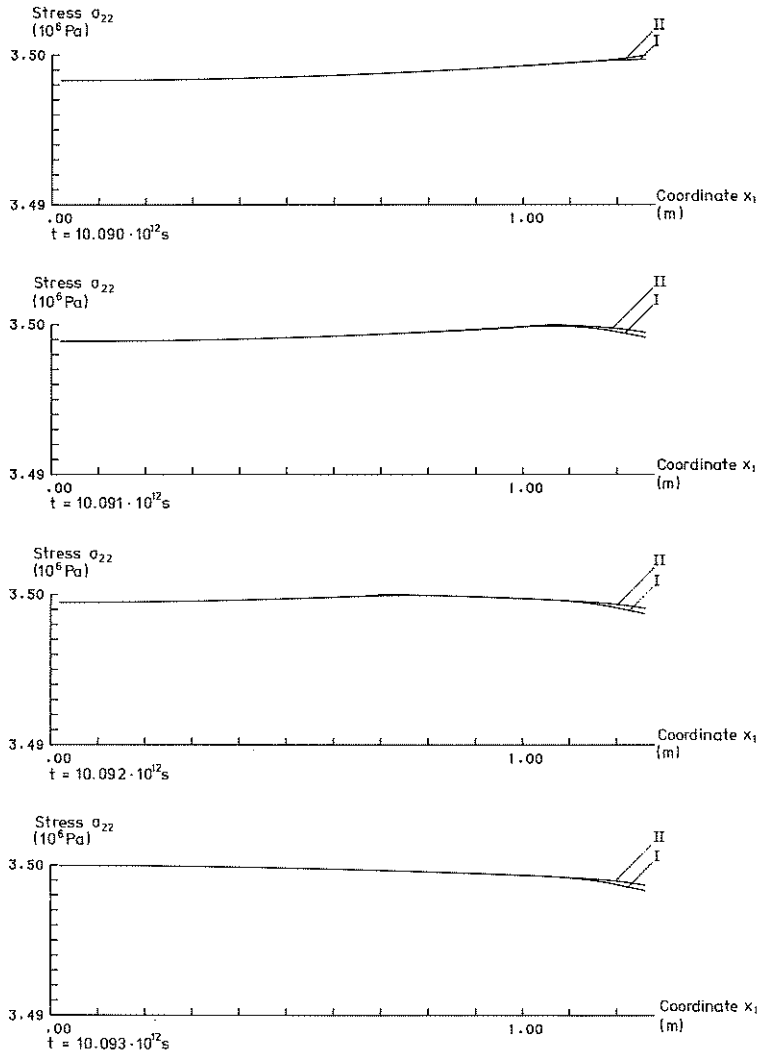
Fig. 6.21. Stress distributions in structure with insulation corresponding to 126.72 m concrete. Curve I shows the stress just above the lower boundary and curve II just above the horizontal centre line.

The present analysis demonstrates that the adopted fracture model for environmental loading is able to predict a sequence of different crack behaviours. From the computations it can be observed that the fracture does not localize initially for large stress gradients whereas it localizes initially for small stress gradients. The computations demonstrate that the adopted fracture model is able to predict distributed or localized fracture depending on the stress conditions. Therefore, the distributed fracture predicted in the analyses of drying specimens in Secs. 6.2 and 6.3 is believed to be realistic. To elaborate on this we observe that in the finite element model the stress is computed at the integration points. The stress states at the integration points determine whether or not fracture develops. When the tensile strength is reached the properties of an element change abruptly. The change of element properties leads to redistribution of stresses. For a small stress gradient in the crack direction the redistribution may yield stresses exceeding the tensile strength in the neighbouring element in the crack direction and a decrease of stress in the neighbouring elements in the direction normal to the crack plane. This situation may lead to development of a localized crack. On the other hand, when the stress gradient is steeper the redistribution is not large enough to cause fracture initiation in the neighbouring element in the crack direction. This situation may lead to fracture initiation in the neighbouring elements in the direction normal to the crack plane, resulting in development of distributed fracturing.

7.   CONCLUDING REMARKS

7.1   Conclusions

The present work concerns the environmental influence on concrete structures. A constitutive model is proposed with regard to tensile fracture and the influence of environment and time. Special attention is given to a realistic description of the crack development, applicable in finite element analysis. A smeared approach is adopted and the fracture energy is taken into account in an objective manner with respect to finite element size. Moreover, the shear stiffness of the fractured region is gradually reduced as fracture develops. Also this effect is modelled in an objective manner. Thermal strain and moisture induced strain are taken into consideration and may optionally be assumed to be dependent on the current stress state. Creep is modelled by a rate type formulation where the total stress history need not be available. For plane stress conditions, the constitutive model is implemented in the finite element program CAMFEM. The program is used in finite element simulations of the behaviour of concrete specimens in different situations. One conclusion of the analyses is that the finite element method is a very powerful tool in investigations of the effects of environmental influence on structures.

The proposed smeared crack approach has been used to simulate a concrete tensile specimen. The purpose of the simulation is to show that it reflects the assumed value of the fracture energy per unit area. The analysis has been performed by three different element types, i.e. a three-node triangular element, a four-node isoparametric element and an eight-node isoparametric element. For regular meshes good results have been obtained for all the element types. For distorted meshes good results have been obtained for the isoparametric elements, whereas for the

triangular element the estimated value of the fracture energy is a little too high, owing to the low order of the interpolation functions. It has, however, been shown that the approach itself is able to reflect the input value of fracture energy in an objective manner.

The proposed material model has been used to simulate the behaviour of a non-loaded drying specimen in order to find out to what extent the overall specimen behaviour is influenced by the non-uniform stress state caused by drying. According to the simulation, the deformation after a long time reflects the material contraction due to drying with a deviation of only 1-2%. In the early stages of drying the deviation is, however, as much as 20-30%. The computations have been performed with one set of assumed values of the material parameters representative for concrete. The results are, of course, influenced by the choice of material parameters. However, the assumption of other material parameters representative for concrete would yield qualitatively the same behaviour. From the computations it can be concluded that the deformation after a long time is close to the material contraction due to drying.

The behaviour of a loaded drying specimen has also been simulated in order to find out to what extent the behaviour is due to stress dependence of moisture induced strain and to what extent it can be explained by nonuniform stress distribution due to drying. On the assumption of the conventional moisture induced strain description the deformation after a long time, with the present assumptions, is about 1-2% greater than the sum of the response of a non-loaded drying specimen and the response of a loaded non-drying specimen. In the early stages of drying the difference is about 6-8%. Since this behaviour does not reflect

experimental evidence it can be concluded that the non-uniform stress state is not the only source of the observed behaviour. When, on the other hand, the moisture induced strain is assumed to be stress dependent the response of the loaded drying specimen, with the present assumptions, is for both early and late stages of drying about 15-20% greater than the sum of the response of the non-loaded drying specimen and the response of the loaded non-drying specimen. In contrast to the result for the conventional moisture induced strain description, this behaviour reflects the experimentally observed behaviour. From the computations it can therefore be concluded that the experimentally observed Pickett effect is to a major extent a material effect, which is most conveniently described as stress dependence of moisture induced strain.

7.2   Future development

The concept used in the foregoing for smeared modelling of tensile fracture represents an improvement compared with previously used concepts. Further development would, however, be of interest, in order that the remaining forces occurring at the ends of the analyses of tension specimens may be eliminated and that non-orthogonal cracks may be handled. Owing to the limited number of experimental results concerning the shear behaviour of cracked concrete the applied assumption regarding shear stiffness is based on the response of concrete with fully developed cracks. To obtain a more sophisticated description of the shear stiffness it would be desirable to have experimental evidence concerning the shear behaviour of concrete with partly developed cracks. Although there have been no implications that the solutions obtained above are not unique, it would be desirable to establish a criterion for determining whether an obtained solution is unique. It would also be of interest to investigate further under what conditions distributed fracture and localized fracture develop.

One of the conclusions of the present work is that the stress dependence of the moisture induced strain is significant when explaining the Pickett effect. At present the stress dependence is assumed to be isotropic. Since available experimental data from uniaxially loaded drying specimens generally relate to the deformation only in the loading direction, theoretical simulations of the specimens provide an opportunity for the determination of only one of the two material parameters describing the stress dependence of the moisture induced strain. To determine the other parameter it would be desirable to have information about the deformation perpendicular to the loading direction. Also, to obtain a quantitatively correct simulation of the behaviour the concept for stress dependence may have to be improved in order to include nonlinear and anisotropic dependence on stress. At present, stress dependence of moisture induced strain has been applied only to the first drying of the material. In order that the behaviour of multiple drying and wetting cycles may be considered, more experimental data is needed.

In the present work the influence of moisture on concrete has been mainly studied, although the influence of temperature is included in the constitutive model. The knowledge about crack development in drying specimens which has been provided by the present work facilitates future studies of environmental influence from e.g. chemical substances, which may be influenced by the presence of cracks in the concrete.

To investigate the behaviour of more complicated concrete structures than those considered in the present work, a sequence of topics arise like: the description of compressive failure, the influence of reinforcement and the interaction between concrete and reinforcement, etc.

The applications in the present work all relate to concrete. The description of tensile fracture can, however, be directly applied to other materials, e.g. rock, metal powder and wood based materials. The description of stress dependent moisture induced strain can also be applied to wood based materials, where however, the influence of multiple drying and wetting cycles is more significant than in the case of concrete.

APPENDIX A: NOTATIONS

Notations are explained in the text where they first occur. Most of them are also given in this appendix.

$A_{\alpha\beta}$ fracture strain compliance parameter

a_{ik} direction cosine

B strain-displacement matrix

$B_{\alpha\beta}$ fracture strain compliance parameter

C material compliance matrix

C material compliance tensor

C_c^n creep compliance matrix

$C^{c,n}$ creep compliance tensor

C_e elastic compliance matrix

C^e isotropic elastic compliance tensor

C^f fracture strain compliance tensor

C_T thermal strain compliance matrix

C^T thermal strain compliance tensor

C_w moisture induced strain compliance matrix

C^w moisture induced strain compliance tensor

D material stiffness matrix

D material stiffness tensor

D_w diffusivity

E elastic modulus

F_n creep compliance parameter

F_T thermal strain compliance parameter

F_w moisture induced strain compliance parameter

$\mathbf{f}$	body force vector
$\mathbf{f}_t$	tensile strength
G	transformation matrix
G_F	fracture energy per unit area
G_s	slip modulus
$\mathbf{i}_i$	unit vector
J_α	fracture strain compliance parameter
K	tangential structural stiffness matrix
L_α	characteristic length
N	slope of stress-crack width curve
N_{im}	interpolation function
$\dot{\mathbf{P}}$	load rate matrix
$\dot{\mathbf{P}}^0$	pseudo load rate matrix
$\mathbf{P}^*$	out-of-balance force matrix
T	temperature
t	time
$\mathbf{t}$	traction vector
$\mathbf{u}$	displacement vector
$\dot{\overline{\mathbf{u}}}$	nodal displacement rate matrix
v_{im}	weighting function
w	moisture content
w_c	crack width at zero stress
w_α	crack width
$w^s_{\alpha\beta}$	shear displacement in crack
x_i	coordinate axis
α_T	coefficient of thermal expansion.

Appendix A

Symbol	Description
α_w	coefficient of drying shrinkage
β_T	stress dependence indicator
β_w	stress dependence indicator
γ^n	material history integral tensor
γ_c^n	material history integral matrix
γ_f	crack irreversibility parameter
δ_{ij}	Kronecker's delta
$\dot{\epsilon}$	strain rate matrix
$\dot{\epsilon}$	total strain rate tensor
$\dot{\epsilon}_0$	stress rate independent strain rate matrix
$\dot{\epsilon}^0$	stress rate independent strain rate tensor
$\dot{\epsilon}_c$	creep strain rate
$\dot{\epsilon}^c$	creep strain rate tensor
$\dot{\epsilon}^e$	elastic strain rate tensor
$\dot{\epsilon}^f$	fracture strain rate tensor
$\dot{\epsilon}_T$	thermal strain rate matrix
$\dot{\epsilon}^T$	thermal strain rate tensor
$\dot{\epsilon}_t$	strain rate matrix representing the effect of change of elastic properties
$\dot{\epsilon}^t$	strain rate tensor representing the effect of change of elastic properties
$\dot{\epsilon}_w$	moisture induced strain rate matrix
$\dot{\epsilon}^w$	moisture induced strain rate tensor
κ_c^n	creep compliance parameter
κ_e	elastic compliance parameter
κ_T	thermal strain compliance parameter

κ_w moisture induced strain compliance parameter

υ Poisson's ratio

υ_n creep compliance parameter

υ_T thermal strain compliance parameter

υ_w moisture induced strain compliance parameter

ρ_c^n creep compliance parameter

ρ_e elastic compliance parameter

ρ_T thermal strain compliance parameter

ρ_w moisture induced strain compliance parameter

$\dot{\sigma}$ stress rate matrix

σ stress tensor

$\dot{\sigma}_0$ pseudo stress rate matrix

$\dot{\sigma}^0$ pseudo stress rate tensor

τ_n retardation time

$\tilde{\nabla}$ differential operator

Appendix A

APPENDIX B: DESCRIPTION OF THE COMPUTER PROGRAM CAMFEM

Problem independent program structure

In CAMFEM the computational procedure is defined by the commands
given by the user. A command consists of a command name followed
by arguments. The different parts of a command are separated by
empty spaces (blanks). In general the arguments are matrix names
or numbers. All data are stored in matrices named by the user.
The matrices are stored in a one-dimensional array called the
"matrix bank" in the primary memory of the computer, and are
identified by their names. At any stage of a computation the user
can inspect the content of the matrix bank and change it if
desired. The matrices may be either numerical matrices or text
matrices. Data used in computations are stored in numerical
matrices. Text matrices may be used to store commands. A text
matrix containing commands can be used as a macro command which
is executed by giving a special command. In e.g. a time stepping
procedure the same sequence of commands is to be executed several
times. The computational procedure can be defined by a set of
macro commands. By rearranging the macro commands, the
computational procedure can easily be changed. In a conventional
finite element program a modification in the computational
procedure often results in a lot of changes in the program code.
The structure of the matrix bank is illustrated in Fig. B.1.

Matrices stored in the matrix bank may be copied to the "external
matrix bank" which is stored in a file in a backing store. When
so desired matrices stored in the external matrix bank may be
copied to the matrix bank.
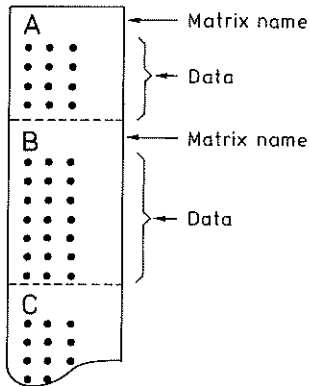
<u>Fig. B.1</u>.   Matrix bank.

During execution of the program, commands given by the user via the keyboard are stored in the "command bank" which is held in a backing store. The commands stored in the command bank can be used in the computation. The structure of the command bank is illustrated in Fig. B.2.
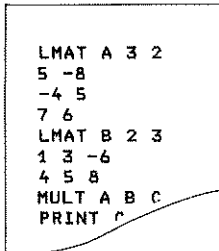
<u>Fig. B.2</u>.   Command bank.

Outputs from the program are displayed on the screen, but are also stored in the "listing bank". The output stored in the listing bank may be directed to a line printer. The listing bank is stored in a backing store. The structure of the listing bank is illustrated in Fig. B.3.

```
***           CAMFEM          ***
***      VERSION 87:01-100     ***
----------------------------------
**LMAT A 3 2
    3 ROWS     2 COLUMNS IN MATRIX A
INPUT OF ROW NO   1 !
**5 -8
INPUT OF ROW NO   2 !
**-4 5
INPUT OF ROW NO   3 !
**7 6
----------------------------------
**LMAT B 2 3
    2 ROWS     3 COLUMNS IN M'''
INPUT OF ROW NO   1 !
**1 3 -6
INPUT OF ROW NO
**4 5 8
------
```

Fig. B.3. Listing bank.

Graphic information generated by the program is stored in the "graphic bank" which is held in a backing store. Several plots may be stored in the graphic bank. Each plot is identified by a name. The last plot of the graphic bank is open for input of additional graphic information. The structure of the graphic bank is shown in Fig. B.4.

Fig. B.5 illustrates the way in which the user can communicate with CAMFEM. The program is stored in the main memory of the computer. Input data are given via the keyboard. The output is displayed on the screen, but may also be directed to the line printer. Graphic information may be directed to a plotter.
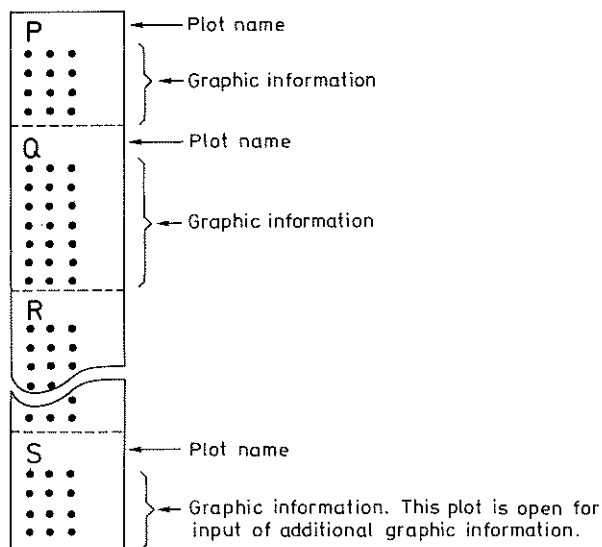
Fig. B.4. Graphic bank.

The problem independent program structure consists of five different groups of commands:

1. Basic commands. Central commands for data handling and termination of a run.

2. Control commands. Commands to control, inter alia, output and the command bank.

3. Graphic commands. Commands for generating graphic information in device independent form and for producing visible output based on this information.

4. Matrix commands. Commands for matrix handling.

5. System commands. Commands for setting up, solution and elimination of systems of equations.
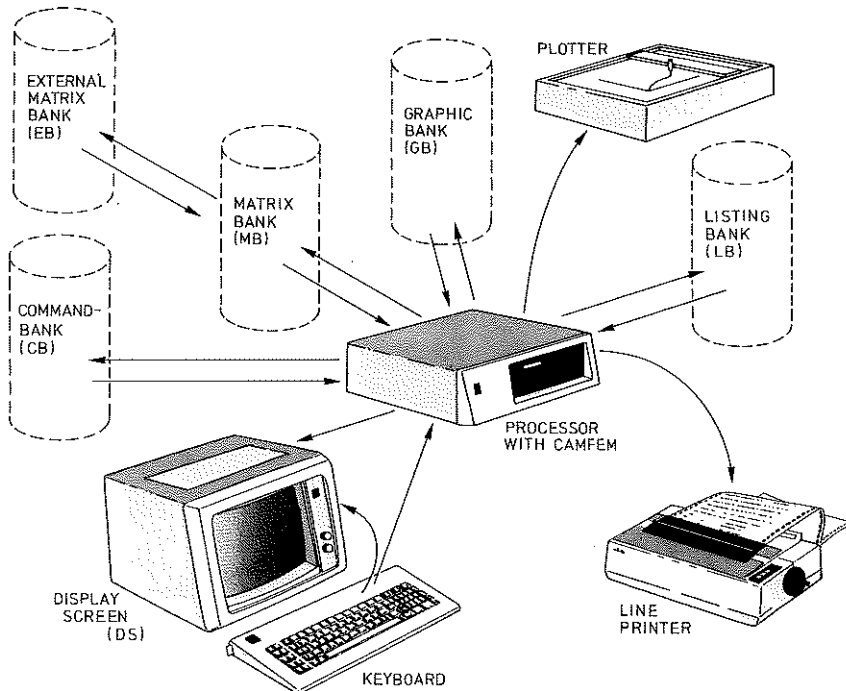
Fig. B.5. Communication with CAMFEM.

In the following is a list of the problem independent commands in CAMFEM. For a detailed description the reader is referred to Ref. [19].

1. Basic commands

LMAT	Load numerical matrix
LTEXT	Load text matrix
DELETE	Delete matrix
COPY	Copy matrix
PRINT	Output matrix
C	Write out a comment line
STOP	Stop execution
START	Get ready for new run

2.   Control commands

DSOFF	Stop output on display screen
DSON	Resume output on display screen
LBSEND	Direct output to line printer
LBDEL	Delete stored output
LBOFF	Stop storage or output
LBON	Resume storage of output
QMOFF	Turn off question mode
QMON	Turn on question mode
LANENG	Give output in English
LANSWE	Give output in Swedish
CBOFF	Stop storage of commands
CBON	Resume storage of commands
EDIT	Edit command bank
RUN	Execute the commands in the command bank
EMACRO	Execute macro command
PMACRO	Set parameters to macro command
BMACRO	Break execution of macro command
EBON	Open external matrix bank
EBOFF	Close external matrix bank
EBSTO	Store matrix in the external matrix bank
EBGET	Get matrix from the external matrix bank
EBDEL	Delete matrix in the external matrix bank
EBCOMP	Compress the external matrix bank
STATUS	List the current status of the control parameters

3.   Graphic commands

GBON	Open graphic bank
GBOFF	Close graphic bank
GBDEF	Define a plot
GBOPEN	Open a previously defined plot for input of graphic information
GBDEL	Delete a plot

GBCOPY   Copy a plot

GBPEN   Change type of pen

GBPOL   Draw a polygon

GBAXIS   Draw coordinate axes

GBTEXT   Write a text

GBVALU   Write a value

GBSEND   Send a plot to an output device

4.   Matrix commands

ADD   Add two matrices

SUB   Subtract one matrix from another

MULT   Multiply one matrix by another

INV   Invert a matrix

DET   Compute the determinant of a matrix

TRANS   Transpose a matrix

REDUCE   Reduce the size of a matrix

ABS   Compute the absolute values of the elements of a matrix

SQRT   Compute the square roots of the elements of a matrix

MAX   Determine the largest value in a matrix

MIN   Determine the smallest value in a matrix

SUM   Compute the sum of the elements of a matrix

PROD   Compute the product of the elements of a matrix

5.   System commands

ELIN   Assemble element matrices

SOLVE   Solve a system of equations

SOLVET   Perform Gaussian reduction

SOLVEB   Perform back substitution

COND   Carry out static elimination

STEP   Carry out step-by-step computation

EIGEN   Solve an eigenvalue problem

To obtain a special purpose program version, the problem independent program structure is supplemented with problem dependent program modules. The problem dependent program modules used in the present study are described below.

Problem dependent program modules

In the present work, the constitutive equations described in Chapter 3 are applied to plane stress problems. The equations have been coded and implemented as commands in CAMFEM.

Two sets of commands are used for the constitutive equations. In the first set of commands elastic, fracturing and moisture induced strains are taken into consideration. The command used to compute tangential material stiffness and pseudo stresses is

MMEF2D MP EV ST SS D PS J $\left[\text{I}\right]$

where

MP contains material properties
EV contains moisture increments
ST contains fracturing data
SS contains stresses
D contains the computed material stiffness
PS contains the computed pseudo stresses
J is a scalar parameter indicating which row of EV, ST and SS is to be used
I is a scalar parameter indicating which group of columns is to be used in EV, ST and SS.

The material parameters stored in MP are elastic modulus E, Poisson's ratio v, tensile strength f_t, fracture energy G_F, slip modulus G_s, irreversibility parameter γ_f, coefficient of drying

shrinkage α_w and stress dependent moisture induced strain
parameter F_w. The matrices EV, ST and SS have one row for each
element and one group of columns for each integration point. The
matrix D has 3 rows and 3 columns and PS is a vector with 3 rows.

Since the equivalent lengths depend on the geometries of the
elements, special element dependent commands are used to compute
the equivalent lengths. The computation is based on the direction
of the maximum principal stress at crack initiation, which is
computed by the command

MMEF2C MP EV ST SS DSN ANGL J [I]

where

DSN   contains the obtained strain increments
ANGL contains the principal stress direction and a parameter
          indicating whether cracking is initiated.

The equivalent length in the maximum principal stress direction
and perpendicular to that direction are also stored in ANGL when
they are computed by element dependent commands.

The stresses obtained are computed by the command

MMEF2S MP EV ST SS SN DSN ANGL J [I]

where

SN   contains strains

The matrix SN has one row for each element and one group of
columns for each integration point.

In the second set of commands elastic, fracturing, moisture induced and creep strains are taken into consideration. The command used to compute material stiffness and pseudo stresses is

MMFC2D MP EV ST SS D PS J [I]

where now

EV also contains time increments
ST also contains creep data

In addition to the material parameters used for the first set of commands, MP now also contains the retardation times τ_1 and τ_2 and creep compliance parameters F_1 and F_2. To describe the creep properties two terms of the Dirichlet series are used.

The direction of the maximum principal stress at crack initiation and the stresses obtained are, respectively, computed by the commands

MMFC2C MP EV ST SS DSN ANGL J [I]

and

MMFC2S MP EV ST SS SN DSN ANGL J [I]

In the present work three element types are used. For the three-node triangular element the element stiffness and load matrices are computed by the command

PLANTK EP EC D PS EK EPR ER J

where

      EP contains element properties

      EC contains element coordinates

      D   contains material stiffness

      PS contains pseudo stresses

      EK contains the computed element stiffness

      EPR contains the computed element pseudo loads

      ER contains the computed element loads

      J   is a scalar parameter indicating which row of EC
           is to be used

The element properties stored in EP are element thickness t and body forces per unit volume f_1 and f_2. To assemble the element matrices and solve the system of equations problem independent commands are used. The strain increments obtained are computed by the command

      PLANTT EP EC EN DU DSN J

where

      EN contains element topology

      DU contains displacement increments

      DSN contains strain increments

The matrix EN has one row for each element.

When cracking is initiated the equivalent lengths are computed by the command

      PLANTC EC ANGL J

where

> ANGL contains principal stress direction and the computed
> equivalent lengths.

The element nodal forces obtained are computed by the command

> PLANTI EP EC SS EF J

where

> SS   contains the stresses
> EF   contains the obtained element nodal forces

For the four-node isoparametric element the element stiffness and
load matrices are computed by the command

> PLANFK EP EC D PS EK EPR ER J [I]

where

> I   is a scalar parameter specifying integration point of
> the element.

If the argument I is omitted one-point integration is used,
otherwise four-point integration is used. When I = 1 the matrix
EK and the vectors EPR and ER are created and the stiffness and
load emanating from integration point No 1 are stored. When I>1
the stiffness and load emanating from the corresponding
integration point are added to EK, EPR and ER.

The strain increments obtained are computed by the command

> PLANFT EP EC EN DU DSN J [I]

When cracking is initiated the equivalent lengths are computed by the command

    PLANFC EC ANGL J

The element nodal forces obtained are computed by the command

    PLANFI EP EC SS EF J

For the eight-node isoparametric element the element stiffness and load matrices are computed by the command

    PLANEK EP EC D PS EK EPR ER J I

For this element four-point integration is used.

The strain increments obtained are computed by the command

    PLANET EP EC EN DU DSN J I

When cracking is initiated the equivalent lengths are computed by the command

    PLANEC EC ANGL J I

The element nodal forces obtained are computed by the command

    PLANEI EP EC SS EF J

Example of use

To demonstrate the use of CAMFEM, supplemented with the commands described above, the structure shown in Fig. B.6 is analysed using two triangular elements. For a more detailed description of the use of commands, see Refs. [19] and [21].

$$E = 21 \cdot 10^9 \, Pa$$
$$v = 0.2$$
$$f_t = 3.3 \cdot 10^6 \, Pa$$
$$t = 3 \cdot 10^{-3} \, m$$
$$\delta = 4 \cdot 10^{-6} \, m$$
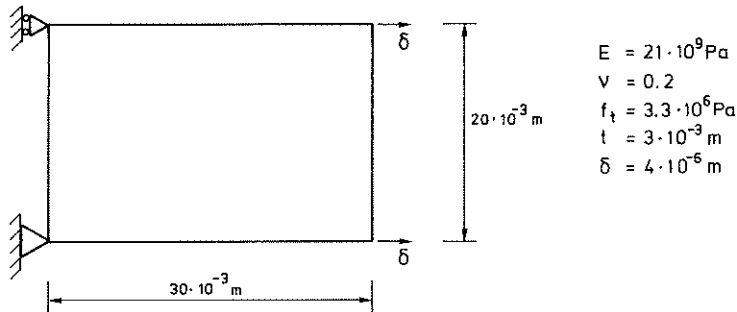
Fig. B.6. Analysed structure.

The element subdivision and the degrees of freedom are shown in Fig. B.7.

The computational procedure is defined by the macro commands shown in Fig. B.8.

The macro command INCR defines one time step in the computational procedure and calls the macro commands STIFF and STRESS. The macro command STIFF is used to compute the stiffness and load emanating from one element. The macro command STRESS is used to compute the stresses and the obtained nodal forces in one element. The contents of the matrices used in Fig. B.8. which have not been previously explained are given below.

    NEQ scalar defining number of equations
    NEL scalar defining number of elements
    K   structural stiffness matrix
    DPR incremental pseudo load matrix
    DDR incremental distributed load matrix
    R   incremental load matrix
    DNR incremental nodal load matrix
    RR out-of-balance force matrix
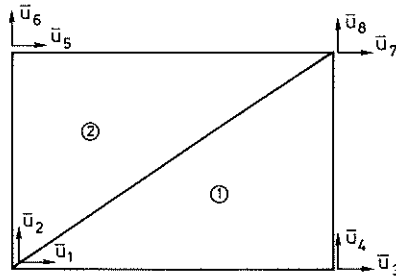
Fig. B.7. Element subdivision and degrees of freedom.

```
MATRIX INCR            18 ROWS     MATRIX STIFF              4 ROWS
==============================     ==============================

 1 LMAT K NEQ NEQ                   1 ADD J ONE J
 2 LMAT DPR NEQ 1                   2 MMEF2D MP EV ST SS D PS J
 3 LMAT DDR NEQ 1                   3 PLANTK EP EC D PS EK EPR ER J
 4 LMAT J 1 1                       4 ELIN EN EK K EPR DPR ER DDR J
 5 EMACRO STIFF NEL
 6 ADD DPR DDR R                   MATRIX STRESS              7 ROWS
 7 ADD R DNR R                     ==============================
 8 ADD RR R R
 9 SOLVE K DU R B Q L 3             1 ADD J ONE J
10 BMACRO L                         2 PLANTT EP EC EN DU DSN J
11 ADD DU U U                       3 MMEF2C MP EV ST SS DSN ANGL J
12 ADD DDR P P                      4 PLANTC EC ANGL J
13 ADD DNR P P                      5 MMEF2S MP EV ST SS DSN ANGL J
14 ADD Q P P                        6 PLANTI EP EC SS EF J
15 LMAT RI NEQ 1                    7 ELIN EN EF RI J
16 LMAT J 1 1
17 EMACRO STRESS NEL
18 SUB P RI RR
```

Fig. B.8. Macro commands.

B   prescribed variables

Q   reaction forces

L   scalar indicating whether the system of equations has been successfully solved

U   displacement matrix

P   total load matrix

RI   obtained nodal force matrix

ONE scalar with the value 1

In Fig. B.9 the computation is set out. The macro commands and the matrices containing data describing the structure have previously been stored in a external matrix bank, from which they are read by the command EBGET. It should be noted that the macro commands of Fig. B.8 can be used to analyse different structures. The properties of a structure are defined by element coordinates, topology, material properties, load and prescribed variables. As mentioned above the macro command INCR defines one time step in the computational procedure. By executing the macro command several times the behaviour of a structure can be studied for varying load and prescribed displacements.

Analytically the displacement $\delta = 4 \cdot 10^{-6}$ m corresponds to a stress $\sigma = E \dfrac{\delta}{L_x} = 2.8 \cdot 10^6$ Pa and reaction forces $R_3 = R_7 = \dfrac{1}{2} \sigma L_y t$ $= 84$ N, which coincides with the results in Fig. B.9.

Fig B.9. Output from CAMFEM computation.

APPENDIX C: REFERENCES

[1]   ANDERSON, C.A.: Numerical creep analysis of structures,
       Chapter 8 of Creep and Shrinkage in Concrete Structures,
       edited by Z.P. Bazant and F.H. Wittmann, John Wiley & Sons,
       1982.

[2]   BATHE, K.J.: Finite Element Procedures in Engineering
       Analysis, Prentice-Hall, Englewood Cliffs, New Jersey 1982.

[3]   BAZANT, Z.P.: Mathematical models for creep and shrinkage
       of concrete, Chapter 7 of Creep and Shrinkage in Concrete
       Structures, edited by Z.P. Bazant and F.H. Wittmann, John
       Wiley & Sons, 1982.

[4]   BAZANT, Z.P.: Mechanics of distributed cracking, Applied
       Mechanics reviews, Vol. 39, No. 5, pp. 675-705, May 1986.

[5]   BAZANT, Z.P., ASGHARI, A. and SCHMIDT, J.: Experimental
       study of creep of hardened Portland cement paste at
       variable water content, Materials and Structures, RILEM,
       Vol. 9, No. 52, pp. 279-290, 1976.

[6]   BAZANT, Z.P. and CEDOLIN, L.: Blunt crack band propagation
       in finite element analysis, Journal of the Engineering
       Mechanics Division, ASCE, Vol. 105, No. EM2, April 1979,
       pp. 279-315.

[7]   BAZANT, Z.P. and CHERN, J.C.: Concrete creep at variable
       humidity: Constitutive law and mechanism, Materials and
       Structures, Vol. 18, No. 103, pp. 1-20, 1985.

[8]   BAZANT, Z.P. and OH, B.H.: Crack band theory for fracture
       of concrete, Materials and Structures, RILEM, Vol. 16, No.
       93, pp. 155-177, 1983.

[9] BAZANT, Z.P. and RAFTSHOL, W.J.: Effect of cracking in drying and shrinkage specimens, Cement and Concrete Research, Vol. 12, pp. 209-226, 1982.

[10] BERGAN, P.G. and SØREIDE, T.: A comparative study of different numerical solution techniques as applied to a nonlinear structural problem, computer Methods in Applied Mechanics and Engineering, 2, pp. 185-201, 1973.

[11] Betonghandbok-Material (Swedish Handbook for Concrete Construction-Material), Svensk Byggtjänst, Stockholm 1980.

[12] BYFORS, J.: Plain concrete at early ages, Swedish Cement and Concrete Research Institute, Fo 3:80, Stockholm 1980.

[13] CARSLAW, H.S. and JAEGER, J.C.: Conduction of heat in solids, Second edition, Oxford University Press, Oxford 1959.

[14] CHEN, W.F.: Plasticity in reinforced concrete, McGraw-Hill, 1982.

[15] CHEN, W.F. and SALEEB, A.F.: Constitutive equations for engineering materials, Volume 1: Elasticity and modeling, John Wiley & Sons, 1982.

[16] DAHLBLOM, O.: CAMFEM applied to nonlinear structural analysis, Report TVSM-7016, Lund Institute of Technology, Division of Structural Mechanics, Lund 1983.

[17] DAHLBLOM, O.: Multiaxial elastic and elastic-plastic material models, Report TVSM-7014, Lund Institute of Technology, Division of Structural Mechanics, Lund 1983.

[18]   DAHLBLOM, O. and PETERSON, A.: CAMFEM – Computer aided
        modelling based on the finite element method, Report
        TVSM-3001, Lund Institute of Technology, Division of
        Structural Mechanics, Lund 1982.

[19]   DAHLBLOM, O. and PETERSON, A.: Manual for CAMFEM – a
        program for computer aided modelling based on the finite
        element method, Version 87. To be published.

[20]   DAHLBLOM, O., PETERSON, A. and PETERSSON, H.: CALFEM – a
        program for computer-aided learning of the finite element
        method, Engineering Computations, Vol. 3, No. 2, June 1986,
        pp. 155-160.

[21]   DAHLBLOM, O., PETERSON, A. and PETERSSON, H.: Manual for
        CALFEM – a program for computer aided learning of the
        finite element method, Version 85, Report TVSM-3007, Lund
        Institute of Technology, Division of Structural Mechanics,
        Lund 1986.

[22]   DAY, R.L., CUFFARO, P. and ILLSTON, J.M.: The effect of
        rate of drying on the drying creep of hardened cement
        paste, Cement and Concrete Research, Vol. 14, No. 3, pp.
        329-338, 1984.

[23]   DOMONE, P.L.: Uniaxial tensile creep and failure of
        concrete, Magazine of Concrete Research, Vol. 26, No. 88,
        pp. 144-152, 1974.

[24]   ENGLAND, G.L. and ROSS, A.D.: Reinforced concrete under
        thermal gradients, Magazine of Concrete Research, Vol. 14,
        No. 40, pp. 45-12, 1962.

[25]   Finite element analysis of reinforced concrete, American
        Society of Civil Engineers, New York 1982.

[26] GAMBLE, B.R. and PARROTT, L.J.: Creep of concrete in compression during drying and wetting, Magazine of Concrete research, Vol. 30, No. 104, pp. 129-138, 1978.

[27] GLEMBERG, R.: Dynamic analysis of concrete structures, Constitutive modelling, Dynamic substructuring, Computer implementation, Publication 84:1, Chalmers University of Technology, Department of Structural Mechanics, Göteborg 1984.

[28] HANSEN, T.C. and ERIKSSON, L.: Temperature change effect on behaviour of cement paste, mortar and concrete under load. Journal of ACI 63, pp. 489-504, 1966.

[29] HILLERBORG, A.: A model for fracture analysis, Report TVBM-3005, Lund Institute of Technology, Division of Building Materials, Lund 1978.

[30] HILLERBORG, A., MODÉER, M. and PETERSSON, P-E.: Analysis of crack formation and crack growth in concrete by means of fracture mechanics and finite elements, Cement and Concrete Research, Vol. 6, pp. 773-782, 1976.

[31] ILLSTON, J.M. and SANDERS, P.D.: The effect of temperature change upon the creep of mortar under torsional loading, Magazine of Concrete Research, Vol. 25, No. 84, pp. 136-144, 1973.

[32] INGREFFEA, A.R. and SAOUMA, V.: Numerical Modelling of discrete crack propagation in reinforced and plain concrete, Fracture Mechanics of Concrete: Structural Application and Numerical Calculation, Edited by G.C. Sih and A. DiTommaso, Martinus Nijhoff Publ., pp. 171-225, Dordrecht 1985.

[33] ISHAI, O. and GLUCKLICH, J.: The effect of extreme hygrometric changes on the isotropy and deformability of mortar and concrete specimens, RILEM Symposium on Moisture Problems in Buildings, Otaniemi, Finland, paper 1-4, pp. 1-26, 1965.

[34] LEIBENGOOD, L.D., DARWIN, D. and DODDS, R.H.: Parameters affecting FE analysis of concrete structures, Journal of Structural Engineering, Vol. 112, No. 2, February 1986.

[35] MALVERN, L.E.: Introduction to the Mechanics of a Continuous Medium, Prentice-Hall, Englewood Cliffs, New Jersey 1969.

[36] MAMILLAN, M.M.: Etude sur le fluage du béton, Annales de l'Institut Technique du Batiment et des Travaux Publics, No. 134, pp. 221-233, Paris 1959.

[37] MODÉER, M.: A fracture mechanics approach to failure analyses of concrete materials, University of Lund, Division of Building Materials, Lund 1979.

[38] NEVILLE, A.M.: Role of cement in the creep of mortar, Journal of the American Concrete Institute, Proceedings Vol. 55, No. 9, pp. 963-984, 1959.

[39] NILSSON, L.: Impact loading of concrete structures, A constitutive modelling, finite element analysis, and experimental study of nonlinear wave propagation, Publication 79:1, Chalmers University of Technology, Department of Structural Mechanics, Göteborg 1979.

[40] NILSSON, L. and OLDENBURG, M.: Nonlinear wave propagation in plastic fracturing materials − a constitutive modelling and finite element analysis, IUTAM Symposium: Nonlinear Deformation Waves, Tallin 1982, Springer, Berlin 1982, pp. 209−217.

[41] OLDENBURG, M.: Finite element analysis of tensile fracturing structures, Licentiate thesis 1985:010L, Luleå University, Division of Computer Aided Analysis and Design, Luleå 1985.

[42] OLSSON, M.: Analysis of structures subjected to moving loads, Report TVSM−1003, Lund Institute of Technology, Division of Structural Mechanics, Lund 1986.

[43] OTTOSEN, N.S.: Thermodynamic consequences of strain softening in tension, Journal of Engineering Mechanics, ASCE, Vol. 112, No. 11, pp. 1152−1164, 1986.

[44] OTTOSEN, N.S. and DAHLBLOM, O.: Smeared crack analysis using a nonlinear fracture model for concrete, Numerical Methods for Non−Linear Problems, Vol. 3, Edited by C. Taylor, D.R.J. Owen, E. Hinton and F.B. Damjanic, Pineridge Press, pp. 363−376, 1986.

[45] PARROTT, L.J.: A study of transitional thermal creep in hardened cement paste, Magazine of Concrete Research, Vol. 31, No. 107, pp. 99−103, 1979.

[46] PAULAY, T. and LOEBER, P.S.: Shear transfer by aggregate interlock, Shear in reinforced concrete, Volume 1, Special Publication SP−42, pp. 1−15, American Concrete Institute, Detroit, Michigan 1974.

[47] PETERSON, A.: Finite element analysis of structures at high temperatures, Report TVSM-1001, Lund Institute of Technology, Division of Structural Mechanics, Lund 1984.

[48] PETERSSON, P-E.: Crack growth and development of fracture zones in plain concrete and similar materials, Report TVBM-1006, Lund Institute of Technology, Division of Building Materials, Lund 1981.

[49] PICKETT, G.: The effect of change in moisture content on the creep of concrete under a sustained load, Journal of the American Concrete Institute, Proceedings Vol. 38, No. 4, pp. 333-355, 1942.

[50] RASHID, Y.R.: Ultimate strength analysis of reinforced concrete pressure vessels, Nuclear Engineering and Design, Vol. 7, No. 4, April 1968, pp. 334-344.

[51] REINHARDT, H.W.: Fracture mechanics of an elastic softening material like concrete, HERON, Vol. 29, No. 2, Delft 1984.

[52] ROTS, J.G., NAUTA, P., KUSTERS, G.M.A. and PLAAUWENDRAAD, J.: Smeared crack approach and fracture localization in concrete, HERON, Vol. 30, No. 1, 1985.

[53] SAEMANN, J.C. and WASHA, G.W.: Variation of mortar and concrete properties with temperature, Journal of the American Concrete Institute, Vol. 54, pp. 385-395, 1957.

[54] SANDBERG, G.: Finite element modelling of fluid-structure interaction, Report TVSM-1002, Lund Institute of Technology, Division of Structural Mechanics, Lund 1986.

[55] STRICKLIN, J.A., HAISLER, W.E. and VON RIESEMANN, W.A.: Evaluation of solution procedures for material and/or geometrically nonlinear structural analysis, AIAA Journal, Vol. 11, pp. 292-299, 1973.

[56] SUN, J.: Finite element analysis of thin shells, Report TVSM-3008, Lund Institute of Technology, Division of Structural Mechanics, Lund 1986.

[57] THELANDERSSON, S.: Modelling of combined thermal and mechanical action of concrete, to be published in Journal of Engineering Mechanics, ASCE.

[58] THELANDERSSON, S.: On the multiaxial behaviour of concrete exposed to high temperature, Nuclear Engineering and Design, Vol. 75, No. 2, pp. 271-282, 1983.

[59] WITTMANN, F.H. and ROELFSTRA, P.E.: Total deformation of loaded drying concrete, Cement and Concrete Research, Vol. 10, pp. 601-610, 1980.

[60] ZIENKIEWICZ, O.C.: The Finite Element Method, McGraw-Hill, London 1977.